Vertical-cavity laser with a novel grating mirror

Park, Gyeong Cheol; Chung, Il-Sug; Semenova, Elizaveta

Publication date:
2016

Document Version
Publisher's PDF, also known as Version of record

Vertical-cavity laser with a novel grating mirror

Gyeong Cheol Park

Department of Photonics Engineering

Technical University of Denmark

A thesis submitted in partial fulfillment for the degree of

Doctor of Philosophy

February 2016

Acknowledgements

The experimental project has been carried out at DTU Fotonik, the Department of Photonics Engineering, in the Nanophotonics Theory & Signal Processing group from February 2013 to February 2016 and has been supervised by Associate Professor Il-Sug Chung and Dr. Elizaveta Semenova.

First and foremost, I would like to thank my main supervisor Il-Sug Chung for giving me the chance to conduct this experimental project with his supporting in many ways. I would also like to show my gratitude to my co-supervisor Elizaveta Semenova for her kind support and encouragement. I thank Supannee Learkthanakhachon for introducing me how to start Danchip cleanroom work and for sharing general knowledge. I also thank Alireza Taghizadeh for sharing his numerical simulation knowledge, providing numerical simulation results, which are inserted in this thesis, and proofreading. I would like to thank Dr. Weiqi Xue for helping me to characterize the hybrid laser devices and for sharing his characterization skill and knowledge with kindness. I also thank Dr. Radu Malureanu for giving me a detail explanation about his reflectance measurement setup and allowing me to use the setup for the HG reflector characterization. I am grateful to Dr. Molly Piels for helping me to characterize and analyze the dynamic property of the high-speed hybrid laser device. I would also like to thank Dagmawi Alemayehu Bekele for supporting me during the tough PhD life and for proofreading.

I would like to thank all colleagues of the Theory & Signal Processing group for sharing their enormous physical insight and fruitful discussion during the group meeting. I enjoyed the time whenever there were in-depth and profound discussions. I also thank Charlotte Melgaard Larsen for helping me to handle administrative work and always greeting me with a warm hello. Personally, I would like to thank Professor Jesper Mørk for listening and respecting my opinions. My special thanks go to Christine Pepke Pedersen for translating Abstract into Danish. In addition, I gratefully acknowledge the PhD Scholarship funded by DTU.

I thank all former colleagues of the Optoelectronics Laboratory, Gwangju Institute of Science and Technology (GIST), Korea. Especially, I learned a lot of experimental knowledge and characterization skills from Dr. Young Min Song and Eun Sil Choi. Personally, Dr. Young Min Song imbued me with passion toward research. I also thank Dr. Kwangwook Park and Gunwu Ju for sharing the same

difficulties and their proofreading. I would like to thank Professor Jae Su Yu for leading me this exciting research area and for his sincere advice. I would like to extend my thanks to Professor Yong Tak Lee, my former supervisor, and leader of the Optoelectronics Laboratory. In the Optoelectronics laboratory, Professor Youg Tak Lee conducts diverse experimental works from MBE growth, device fabrication, and characterization; and hence, I had a lot of chances to expand my knowledge during my Master study. Without the experimental experience in the Optoelectronics Laboratory, I could not have conducted my PhD project properly.

Last but not least, I would like to thank my parents who always believe in my decision and always support me. I would also like to thank my sister and brother who always try to share my difficulty and give me advice. Also, I thank my first nephew for giving me a lot of delight.

Gyeong Cheol Park
Kongens Lyngby, 14. February, 2016.

Abstract

Hybrid III-V on silicon (Si) 'vertical cavity lasers' (hybrid VCLs), which can emit light *laterally* into a Si waveguide, are fabricated and investigated. The Si-integrated hybrid VCL consists of a top dielectric Bragg reflector (DBR), a III-V active layer, and a bottom high contrast grating (HCG) mirror formed in the Si layer of a Si-on-insulator (SOI) wafer. The hybrid VCLs have a promising potential for very high-speed operation and low energy consumption, which is ideal for optical interconnects as well as large data center applications.

For the experimental demonstration of hybrid VCLs, CMOS-compatible fabrication processes are designed and developed. These include a low-temperature direct wafer bonding process for integrating III-V layers onto a SOI wafer, as well as two types of DBR formation processes: a lift-off process and an etch-back process. Based on these, two versions of optically-pumped hybrid VCLs have been fabricated.

The first version of hybrid VCL is designed for demonstrating in-plane emission into a Si waveguide. The in-plane emission is enabled by the bottom HCG abutting the Si waveguide, which not only functions as a highly reflective mirror but also routes the light from the vertical cavity laterally into the Si waveguide. The measured in-plane emission proves the lasing action with a side-mode suppression ratio (SMSR) of 27.5 dB at a peak wavelength of 1486 nm. The threshold pumping power corresponds to a current injection of 1.1 mA. A signature of highly anisotropic cavity dispersion has been observed and discussed, which is unique for HCG-based vertical cavities.

The second version proves the potential for high-speed operation of hybrid VCL structure. In the hybrid VCL structure, the effective cavity length is substantially reduced by using a dielectric DBR and a TM-HCG with a very short evanescent tail. This reduces the photon lifetime of the laser cavity significantly without reducing the mirror reflectivity, leading to a very high intrinsic speed. A 3 dB frequency of 27.2 GHz was measured at a pumping power corresponding to a current injection of 0.7 mA. Since the pumping power was limited by the setup, the 3 dB frequency could be even higher. At this pumping level, the SMSR was about 49 dB and the lasing wavelength was 1541 nm. It was noteworthy that a modulation current efficiency factor (MCEF) of 42.1 GHz/mA$^{1/2}$, which is 3 times greater than the cutting edge 850 nm VCSEL. Besides, this large MCEF is desirable for significantly lowering the injection current at a given target speed, which implies the amount of heat generation can potentially be reduced by 2 orders of magnitude than the 850 nm VCSELs.

Last, a new type of grating reflector, referred to as hybrid grating (HG) is analyzed and demonstrated, which may improve the heat dissipation efficiency of HCG-based hybrid VCL structures. The HG mirror consisting of a bottom grating and a high-refractive-index cap layer integrated on the grating can provide a stop band even broader than HCG. The interaction between the cap and the bottom grating results in strong Fabry-Perot (FP) resonance as well as weak guided mode (GM) resonance. Most of the reflected power come from the FP resonance while the GM resonance performs a crucial role in achieving a reflectance of almost 100% as well as broadening the stopband as wide as 300 nm.

Resumé

Projektet fabrikerer og undersøger hybride III-V på silicium (Si) 'vertikale kavitets lasere' (hybride VCLs), som kan udsende lys *sidelæns* ind i en Si-bølgeleder. Den Si-integrerede hybride VCL består i toppen af en dielektrisk Bragg reflektor (DBR), så et III-V aktivt lag, og derefter en bund af et høj kontrast gitter (HCG) spejl formet i Si laget af en Si-på-insulator (SOI) wafer. De hybride VCLs har potentielle anvendelsesmuligheder for høj-hastighed og energi-effektive optiske forbindelser samt for data center anvendelser.

CMOS-kompatible fabrikations processer er designet og udviklet til den eksperimentelle demonstration af optisk-pumpede hybride VCLs. Disse inkluderer en lav-temperatur direkte wafer bindende process til at integrere III-V lag på en SOI wafer, samt to typer af DBR formations processeer: en lift-off process og en etch-back process.

Den hybride VCL er egnet til emission i planet ind i en Si-bølgeleder. Bund HCG spejlet, tilstødende til Si-bølgelederen, fungerer ikke kun som et høj reflektivt spejl, men leder også det vertikal-forstærkede lys sidelæns ind i Si-bølgelederen. Den målte emission i planet beviser at strukturen laser med et undertrykkelsesforhold af side-mode på 27.5 dB i peak bølgelægnden på 1486 nm. Den brede linjebredde på 0.66 nm med mange under peaks kommer fra den anisotropiske kavitets dispersion af den HCG-baserede vertikale kavitet.

Potentialet for høj-hastigheds operation ved brugen af hybride VCL strukturer er bevist ved at squeeze den effektive kavitets længde, hvilket er en kritisk faktor i at bestemme den indre hastighed af laseren. I den hybride VCL, er den effektive kavitets længde væsentligt reduceret ved at bruge en dielektrisk DBR og en transvers magnetisk HCG med en meget kort evanescent hale. Den hybride VCL viser en 3 dB båndbredde af 27.2 GHz ved en lang bølgelængde på 1541 nm. En modulation strøm effektivitets faktor (MCEF) på 42.1 GHz/mA$^{1/2}$ er estimeret, hvilket er 3 gange større end 850 nm VCSEL cutting edge.

Til sidst bliver en ny type hybrid gitter (HG) spejl for hybride VCLs analyseret og demonstreret. HG spejlet består af et bund gitter og et højt brydnings-index cap-layer integreret på gitteret. Vekselvirkningen mellem cap-layer og det nederste gitter resulterer i stærke Fabry-Perot (FP) resonanser og også svagt guided mode (GM) resonanser. Det meste af den reflekterede effekt kommer fra FP resonansen mens GM resonansen spiller en afgørende rolle i at opnå en reflektans på næsten 100% lige så vel som at forbredde stopbåndet så bredt som 300 nm.

List of Publications

The work carried out during this PhD project has resulted in the following publications.

□ Journal paper

1. A. Taghizadeh, G. C. Park, J. Mørk and I.-S Chung. Hybrid grating reflector with high reflectivity and broad bandwidth. *Opt. Express* **22**, 21175 (2014).

2. G. C. Park, W. Xue, A. Taghizadeh, E. Semenova, K. Yvind, J. Mørk and I.-S. Chung. Hybrid vertical-cavity laser with lateral emission into a silicon waveguide. *Laser Photon. Rev.* **9**, L11 (2015).

3. D. A. Bekele, G. C. Park, R. Malureanu and I.-S. Chung. Polarization-independent wideband high-index-contrast grating mirror. *IEEE Photon. Technol. Lett.* **27**, 1733 (2015).

4. G. C. Park, A. Taghizadeh and I.-S. Chung. Hybrid grating reflectors: origin of ultrabroad stopband. *Appl. Phys. Lett.* **108**, 141108 (2016).

□ Conference

1. G. C. Park, W. Xue, E. Semenova, K. Yvind, J. Mørk and I.-S Chung. III-V/SOI vertical cavity laser with in-plane output into a Si waveguide. in *Optical Fiber Communication Conference* , paper W2A.17 (2015).

2. G. C. Park, W. Xue, E. Semenova, J. Mørk and I.-S Chung. Hybrid III-V/SOI single-mode vertical-cavity laser with in-plane emission into a silicon waveguide. in *Lasers and Electro-Optics (CLEO)*, paper SW3F.2 (2015).

3. G. C. Park, W. Xue, J. Mørk, E. Semenova and I.-S Chung. III-V/SOI vertical cavity laser structure for 120 Gbit/s speed. in *Advanced Photonics 2015*, paper JT5A.2 (2015).

Contents

Appendices

List of Abbreviations

1D . . . . . One-dimensional.

a-Si . . . . . Amorphous silicon.

BOT . . . . . Bandwidth over thickness

BOX . . . . . Buried oxide.

CMOS . . . . . Complementary metal-oxide-semiconductor.

c-Si . . . . . Crystalline silicon.

CW . . . . . continuous-wave

DBR . . . . . Distributed Bragg reflector.

DWB . . . . . Direct wafer bonding.

FB . . . . . Fractional bandwidth

FWHM . . . . Full-width at half-maximum

GMR . . . . . Guided-mode resonance.

HCG . . . . . High contrast grating.

HG . . . . . Hybrid grating.

QW . . . . . Quantum well.

RCWA . . . . Rigorous coupled-wave analysis.

RT . . . . . Room temperature.

SOI . . . . . Silicon-on-insulator.

TE . . . . . Transverse electric.

TM . . . . . Transverse magnetic.

VCL . . . . . Vertical cavity laser.

VCSEL . . . . Vertical-cavity surface-emitting laser.

VOC . . . . . Vertical outgassing channel.

- EQUIPMENT -

ASE . . . . . Advanced silicon etcher

IBD . . . . . Ion beam deposition

ICP . . . . . Inductively coupled plasma RIE

PECVD . . . . Plasma-enhanced chemical vapor deposition

RIE . . . . . Reactive-ion etcher

SEM . . . . . Scanning electron microscope

- CHARACTERIZATION -

DM . . . . . Dichroic mirror

EDFA . . . . . Erbium-doped fiber amplifier

MM . . . . . Multi-mode

MZM . . . . . Mach-Zehnder modulator

NA . . . . . Network analyzer

OSA . . . . . Optical spectrum analyzer

PC . . . . . Polarization controller

PCF . . . . . Photonic crystal fiber

PD . . . . . Photo detector

PL . . . . . Photoluminescence or polarization

SM . . . . . Single mode

We know very little, and yet it is astonishing that we know so much, and still more astonishing that so little knowledge can give us so much power.

— Bertrand Russell

1 Introduction

1.1 Introduction

1.1.1 Motivation

The dramatic increase in computing and signal processing in modern society requires high computing performance. The computing performance is determined by the processing speed of computing unit and the efficiency of interconnects, which connect the computing units [1]. Electrical signal processing via electrical interconnects (EIs) have been used to solve these increasing burdens by decreasing the size of logic gates and increasing the chip size to enhance the integration density [1]. The scaling down of logic gates with a high integration density improves the signal processing speed by reducing the gate delay [1]. However, these efforts have led to a fundamental challenge regarding performance and energy efficiency. This is mainly due to the electrical interconnects through metal wires because the scaling down of the interconnect part does not reduce the RC time constant, leading to a signal delay in the interconnects [1]. Therefore, the current electrical interconnects cause a bottleneck to support the higher signal processing speed of the electrical logic gates.

As an alternative to electrical interconnects, optical interconnects have received intense attention, due to their high technological potential. In principle, the optical interconnects can outperform the electrical interconnects regarding the

speed as well as energy efficiency [2, 3]. If the optical interconnect components are realized in silicon platform, the fully fledged complementary metal-oxide-semiconductor (CMOS) technology can be used to significantly lower the component price, which is a practical consideration for the employment of optical interconnects. Furthermore, the integration of silicon microelectronics and silicon photonics on a single chip is possible, which allows to combine electrical computing part with optical interconnect part [4, 5].

1.1.2 Overview

For the use of truly on-chip optical interconnects, a fast and energy-efficient light source should be integrated on an optical interconnects (OIs) by using CMOS technology [6]. Of the passive and active optical devices, one of the challenging devices to implement on a silicon-on-insulator (SOI) platform, where the silicon photonics circuits are presented, is light source because silicon (Si) itself is an indirect band gap material [7]. When comparing it to a direct band gap material such as a III-V compound, it has much lower efficiency [8, 9].

Over the past decade, there have been scientifically remarkable results such as a continuous-wave (CW) Raman laser and a periodic nanopatterned Si laser that use Si as a gain material [10, 11]. However, these optically-pumped lasers showed low efficiency and low output power, which are not applicable for the present OI applications. As an alternative to the Si as a gain, germanium (Ge) has been grown on SOI platform. Because of a $\sim$4% lattice mismatch between Ge and Si, a thick buffer layer of $\sim$1 μm is needed to overcome the rough surface and threading dislocations. To engineer the indirect band gap of Ge to a direct band gap material, highly n doped and strained Ge layer were used [12]. Recently, a direct band gap GeSn alloy has been grown [13]. Nevertheless, the efficiency and output power are not enough for today's OI applications.

The second way is to grow the direct band gap material on a Si platform: a hetero-epitaxy growth. For a 1.55 μm light source, the InP material system is preferable because the InP material support telecommunication wavelength (1.3 -

1.6 μm) with a superior performance of InGaAlAs active when compared to GaAs material system which use GaInNAs active [14]. However, when the direct band bap material are grown on the heterogeneous material of Si, the lattice mismatch between InP and Si, which is ∼8%, degrades the optical property of active layer compared to that of the III-V active layer grown on their own material system [9].

The third way is to integrate the light source on the SOI platform using a flip-chip bonding [9]. To do the flip-chip bonding, a bulky laser diode die is needed. The bulky solder bumps on the laser die and a bottom SOI platform are prepared. After aligning the solder bumps to the top and bottom of the samples, then the two samples are pressed down. This flip-chip bonding process is not a monolithic integration using CMOS-compatible process. Therefore, it is tricky to densely integrate the light sources on SOI platform.

Last, it is a wafer bonding process. The III-V active material, which was grown on the InP substrate, is directly integrated on the SOI platform. Since the III-V epitaxy is grown on its own material substrate, it possesses high-quality optical properties. After removing the thick InP substrate, the heterogeneously-integrated laser can be fabricated using CMOS-compatible processes [15–17]. With the aid of oxygen plasma-assisted direct wafer bonding (DWB), the electrically-pumped in-plane laser on a SOI platform was demonstrated, for the first time [15]. It showed a maximum output power of 1.8 mW and operated up to 40 °C. Recently, a DFB laser integrated on a SOI platform has been demonstrated with a 3 dB bandwidth of 9.5 GHz and 12.5 Gb/s direction modulation [18]. Besides, a Si-integrated photonic-crystal (PhC) laser with a threshold current of 31 μA has been demonstrated, which reduced the energy consumption further [19]. The Si-integrated DFB and PhC laser cavity structurally emit light along the in-plane direction. It is beneficial because it couples the laser output into the planar silicon photonics circuits. For all these reasons, the in-plane emission laser structure with a III-V gain material, which is integrated on the SOI platform using the DWB process, is the feasible way to introduce an energy-efficient and compact light source for the on-chip OI applications.

Vertical-cavity surface-emitting lasers (VCSELs) have been widely used for short-reach optical communications and data centers because they operate at high-speeds and are energy efficient light sources [20]. Besides, the VCSELs have easy and efficient coupling with a vertically-aligned optical fiber, the possibility of fully monolithic processes, and high integration capability [21]. Nevertheless, it will not be a preferable light source for the on-chip OI application because it needs additional coupling scheme to couple the vertically-amplified lasing output laterally into the in-plane OI system [22].

There has been effort to solve this problem of the vertical cavity laser by introducing a monolithically-integrated grating waveguide structure [23]. For the monolithic integration of a VCSEL with an in-plane waveguide, a GaAs layer for the grating waveguide is epitaxially grown on top of a full VCSEL structure. Then, a grating structure is introduced onto the waveguide layer. The GaAs material of the waveguide layer is chosen because it is the lattice-matched material with the bottom VCSEL's material system. This monolithic integration method cannot be directly adopted for the OI system because the laser output from the GaAs waveguide needs to be coupled into a Si waveguide.

The in-plane emission possibility of a vertical cavity laser using a high contrast grating (HCG) was numerically investigated [24]. Also, a vertical cavity laser with an in-plane emission into a Si waveguide by using a bottom HCG was suggested [25]. The performance of HCGs as a mirror for the vertical cavity laser applications, which require a high reflectance more than 99.5%, was experimentally proven by employing it as the top mirror of a VCSEL [27]. In addition, by using CMOS-compatible fabrication processes, a bottom HCG reflector, which was introduced on a SOI, and a top Si HCG were employed for the vertical cavity laser [28].

1.2 Recent Progress of High-speed VCSELs

After the initial concept of VCSELs had been suggested by K. Iga in 1977 [20], VCSELs have been used in short-reach optical communications and data center applications [26].

Short-wavelength VCSELs ($\lambda \sim$ 800-1,000 nm) with GaAs material system have been intensively and extensively studied, and then become commercialized for various applications [20, 29]. The GaAs material system provides excellent optical, electrical, and thermal properties for the GaAs-based VCSELs. The oxide-confined aperture, which is for the optical and current confinement, and the lattice-matched AlGaAs/GaAs-based epitaxial DBRs with high thermal conductivity support those excellent performances of the VCSELs. The speed performances of current state-of-the-art VCSELs are summarized in Table 1.1 and all of them use the GaAs material system and an oxide-confined aperture.

For long-wavelength (λ 1310 or 1550 nm) VCSELs, which can be used as an energy-efficient and high-speed light source for on-chip optical interconnects [30], an InP material system is used. For the InP-based VCSELs, lattice-matched InGaAsP/InP epitaxial DBRs were employed. The epitaxial DBRs have a low index contrast (Δn $\approx$ 0.2-0.3); and hence, the quarter-wavelength DBR results in a thick mirror with a thickness of more than 5 μm and with more than 28 pairs [31,32]. More importantly, the quaternary lattice-matched DBR has poor thermal conductivity which blocks continuous-wave (CW) operation at high temperature, e.g., up to 85 °C [31]. To overcome the low index contrast, dielectric DBRs are employed to enhance the Δn; and therefore, the total thickness of the DBRs are reduced. However, the low thermal conductivity of the amorphous dielectric materials needs to be addressed as well. In addition, the long-wavelength VCSELs are more likely to suffer from Auger process than the short-wavelength VCSELs because the energy band gap is smaller, which brings the more change for Auger recombination [38].

Table 1.1: High speed short-wavelength VCSELs.

λ (nm)	Bandwidth (GHz)/ @ RT	Bit rate (Gbps)	Temperature (°C)
850	23	40	25 [33]
850	21	39	25 [34]
980	20	35	25 [35]
980	14	25	85 [36]
1060	24	40	25 [37]

Therefore, for the long-wavelength VCSELs with dielectric DBRs, the thermal issue should be addressed. The weakness in terms of the thermal property is solved by depositing a bottom metal layer that acts as a heat sink and partial reflector to support the bottom dielectric DBR [39]. By using the top dielectric and the bottom metal-assisted dielectric DBRs, a long-wavelength VCSEL has been successfully demonstrated at temperature of up to 90°C with a maximum output power of 1 mW [39]. In addition, the VCSEL has operated with 35 Gb/s data transmission at 20°C and 25 Gb/s data transmission at 55°C [39]. This high-speed property results from the short cavity design by employing the top and bottom dielectric mirrors and adopting a proper heat sink structure. The speed performances of long-wavelength VCSELs using the dielectric DBR are listed in Table 1.2.

1.3 Contribution and Outline

The main goal of this thesis work is to experimentally investigate and demonstrate Si-integrated long-wavelength hybrid VCLs with an in-plane emission for on-chip OI applications which is numerically suggested in [25]. The hybrid VCL is comprised of a bottom Si HCG reflector on a SOI wafer, a wafer-bonded III-V active layer on top of the Si HCG, and a top dielectric DBR. In addition, the possibility of high-speed operation of the hybrid structure is investigated and experimentally demonstrated. To experimentally demonstrate the initial proof-of-concept of the Si-integrated long-wavelength hybrid VCLs, CMOS-compatible fabrication procedures are developed, which includes a low temperature direct wafer bonding (DWB) process and two types of DBR formation processes.

Table 1.2: High speed long-wavelength VCSELs.

λ (nm)	Bandwidth (GHz)/ @ RT	Bit rate (Gbps)	Temperature (°C)
1310	11	12	70 [41]
1550	17	35	20 [39]
		25	55 [39]

With these goals, a low-temperature direct wafer bonding (DWB) process and lift-off and etch-back processes for forming a top DBR are mainly developed. The developed process steps are CMOS-compatible and the DWB process is conducted at temperature as low as 300°C. First, using the developed fabrication procedure, an in-plane hybrid VCL is fabricated. On a SOI wafer, a bottom HCG is transferred to the top Si layer. For the heterogeneous integration of the SOI and a III-V active layer, the DWB process is implemented. For the top dielectric DBR, the lift-off process is used to form a 7-pair SiO_2/TiO_2 DBR. Second, for the demonstration of a high-speed hybrid VCL, a bottom HCG and a top dielectric DBR are investigated to squeeze the mode volume of the VCL. For the top DBR mirror, a 6-pair SiO_2/a-Si DBR is formed by using the etch-back process, which has a higher index contrast than SiO_2/TiO_2 and can further reduce the energy penetration depth into the mirror. For the bottom HCG, there are two types of HCG design: the TE HCG and the TM HCG design. The TM HCG design is adopted because the TM HCG possesses a shorter evanescent tail, which can significantly reduce the effective cavity length and hence reduce the mode volume. In addition, during the thesis work, a new type of reflector is numerically investigated. The reflector consists of a bottom grating and a high-refractive-index membrane directly integrated onto the bottom grating. The hybrid grating (HG) reflector is more rigorously investigated and experimentally demonstrated as well by focusing on the function of the high index membrane.

The experimental demonstration shows the possibility of the in-plane emission using the vertical cavity structure. In other words, the in-plane hybrid VCL emits the light into a Si waveguide and has all of the advantages of the conventional VCSELs. Second, the high-speed long-wavelength hybrid VCL proved that there is potential to perform at high speeds like the short-wavelength VCSELs. The 3 dB bandwidth of 27 GHz was obtained. Among the Si-integrated light source such as DFB and PhC laser, it has the highest 3 dB bandwidth. In addition, the HG reflector shows that even though the bottom grating is integrated with a finite-thick high-index layer, it shows a high reflectance with a broader wavelength range than HCGs.

This thesis consists of six chapters. In the first chapter, a general introduction into optical interconnects and the requirement of light sources for the optical interconnects are given. Among the three types of lasers, the vertical cavity structure is investigated because it is energy-efficient and operates at high-speed. To use the vertical cavity for the optical interconnects, the new functionality of the bottom HCG is introduced. For the high-speed operation of the long-wavelength vertical cavity laser, the top dielectric DBR, which can support higher speeds than the epitaxial DBR was used.

In Chapter 2, a general laser theory mainly involved with mirrors and a numerical technique necessary for analyzing HCG or HG structure are discussed. For a high-speeds laser, an energy penetration depth into the mirrors are critical factor to enhance the intrinsic frequency response of lasers. The relation between the energy penetration depth and the intrinsic frequency response are explained to obtain a high-speed laser. Also, the numerical technique, which is explained here, is rigorous coupled-wave analysis (RCWA) and it is used in this thesis work to analyze the HCG and HG reflector. Besides, diverse types of mirrors for long-wavelength VCSELs are introduced by explaining the pros and cons.

Chapter 3 covers the entire fabrication process. This includes the procedures needed to create the Si-integrated hybrid VCLs. There are two main processes. The first one is the direct wafer bonding process which allows for the heterogeneous integration. The second one is the dielectric DBR formation processes: lift-off and etch-back processes. All fabrication processes are enumerated in order and explained in detail.

In Chapter 4, the results of Si-integrated hybrid VCLs are presented. First, the fabricated in-plane hybrid VCL is shown and its static characterization results from the in-plane Si waveguide are described. Second, the mirror properties for the bottom HCG and top dielectric DBR are explained with the goal of high-speed operations. By employing the two mirrors, the high-speed hybrid VCL is fabricated and characterized. The static and dynamic characterization results are presented.

Chapter 5 introduces a new type of mirror which is comprised of a bottom grating and a top high-refractive-index membrane. The membrane is directly integrated to the bottom grating by using the DWB process. The new type of mirror, which is named hybrid grating (HG) reflector, is fabricated and characterized. It demonstrates high broadband characteristics and outperforms the HCG in terms of the reflectance bandwidth.

Lastly, Chapter 6 concludes and summarizes the thesis work. Chapter 6 also examines the current optically-pumped hybrid VCL. The possible structure and technology for implementing an electrically-pumped hybrid VCL are discussed as well.

If we knew what it was we were doing, it would not be called research, would it?

— Albert Einstein

2 Novel Grating Mirrors

Contents

2.1 Introduction

In this chapter, different types of mirrors for long-wavelength (λ = 1310 or 1550 nm) vertical-cavity surface-emitting lasers (VCSELs), which use an InP-material system, are explained. First, it is introduced how distributed Bragg reflectors (DBRs) for long-wavelength VCSELs have been progressed and demonstrated.

For the long-wavelength VCSELs, three types of mirrors have been employed: 1) epitaxial DBRs, 2) dielectric DBRs, and 3) metal-assisted dielectric DBRs [31, 39, 42–45, 49]. The progress was focused on how to solve 1) the limited selection of lattice-matched DBR materials with a small index contrast which causes thick DBRs at the long wavelength and 2) the poor thermal property of the lattice-matched quaternary epitaxial DBR which blocks a continuous wave (CW) operation or high-temperature operation [31, 42].

The recent breakthrough for VCSELs is to employ thin high-contrast grating (HCG) mirror [50]; and hence, it reduces the overall volume of the 850 nm VCSELs [27, 53]. Besides, the HCG mirrors have replaced the bulky long-wavelength DBRs without concerning about the lattice matching condition [28]. The HCG is structurally different from the DBR because it is one-dimensional (1D) structure with alternating high- and low-index grating bars, which is extended along the transverse direction, while the DBR is a periodically alternating high- and low-index layers in the longitudinal direction. Not only the geometric features but also the optical properties are unique compared with the conventional DBRs. Also, a new type of grating mirror denoted as hybrid grating (HG) reflector is briefly introduced, which can be used as a reflector for a vertical cavity laser as well. The new mirror consists of a 1D grating structure and a uniform high-index layer integrated on top of the 1D grating, which shows a broader stopband than that of HCGs [55].

To analyze the DBR mirrors, transfer matrix method (TMM) is usually used [56]. In the case of the 1D grating analysis, rigorous coupled-wave analysis (RCWA) is employed due to the non-uniform layer of the HCG or HGR mirrors [57–60]. Therefore, RCWA method is explained starting from a single grating layer to a multi-block structure which includes a grating layer. The mirrors are characterized by phase penetration depth or energy penetration depth and by physical thickness [52, 62, 63]. The phase penetration depth and energy penetration depth influence the lasing wavelength and the intrinsic relaxation oscillation frequency of a laser, respectively [52, 69].

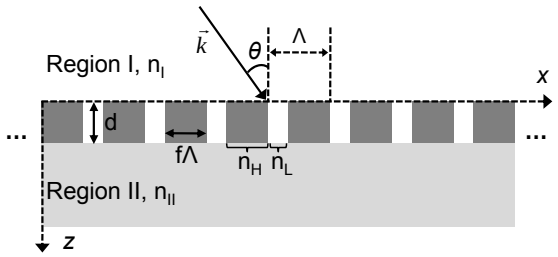

Figure 2.1: Schematic illustration of a 1D infinite grating structure.

In addition, the two distinct features of the HCG and HG mirrors are explained such as polarization-selective reflectance [27] and in-plane guided modes excited inside the grating structure which is perpendicular to the direction of normal incident light [24, 25, 40, 64]. The in-plane guided modes play a vital role to utilize a vertical cavity laser (VCL) as an in-plane light source for silicon photonics or optical interconnect applications.

2.2 Analysis of Grating Structure

There have been numerous applications of periodic grating structures such as surface-relief gratings [57, 59], dielectric-metal surface relief gratings [58], deep gratings [65, 66], aperiodic gratings [67] and HCG reflectors [50], and HG reflectors [55]. Especially, for the VCSEL applications, the epitaxial distributed Bragg reflectors (DBRs) have been successfully replaced with the HCGs. For long-wavelength VCSELs, a DBR with more than 30 pairs is needed, which can be more than $\sim$5 μm in thickness [31, 42]. As an alternative to the thick DBR mirrors, HCG or HG reflector can be used for VCSEL application. To investigate the patterned structure such as HCG, HG, or VCSELs including HCG mirrors, rigorous coupled-wave analysis (RCWA) method is employed.

2.2.1 Diffraction from grating

To investigate a periodic grating reflector interacting with an incident electromagnetic field in terms of reflectance and phase, RCWA method has been proved itself that it is accurate and efficient numerical method by successfully conducting the

numerical investigation of the above mentioned grating structures. Basically, RCWA is a numerical method to solve Maxwell's equation in the spatial frequency domain, and the permittivity of grating structure and the interacting fields are expanded using Fourier series with spatial harmonics of the fundamental spatial frequency [57–60].

The 1D cross-section of grating is shown in Fig. 2.1 and the region I and region II are separated by the grating structure. The grating has a period of Λ, filling factor of 'f' which is defined as the grating bar width (s) over the Λ, and thickness of 'd'. It is assumed that the grating is extended infinitely along the y-direction, and it is infinitely periodic along the x-direction. The grating bars consist of a high index material (n_H) and a low index material (n_L), which form a unit of the grating. For the simplicity, the refractive indices used here are assumed to be non-dispersive materials.

The incident plane wave can be expressed with the $\vec{k} = k_0 n_I(\sin\theta\hat{x} + \cos\theta\hat{z})$ and the incident angle of θ from the surface normal direction of the z-axis as shown in Fig. 2.2. The grating is surrounded by the incident medium, n_I and the exit medium, n_{II}. Then, the incident electric field with a normalized intensity can be expressed as

$$E_{inc,y} = 1 \cdot \exp[-jk_0 n_I(\sin\theta x + \cos\theta z)], \tag{2.1}$$

where $E_{inc,y}$ is the normalized TE polarized light, k_0 is the $2\pi/\lambda_0$ in air and the time dependency of exp(-jωt) is assumed. For a TM polarized light, it can be expressed similar to the TE case using $H_{inc,y}$ field. For the in-depth explanation

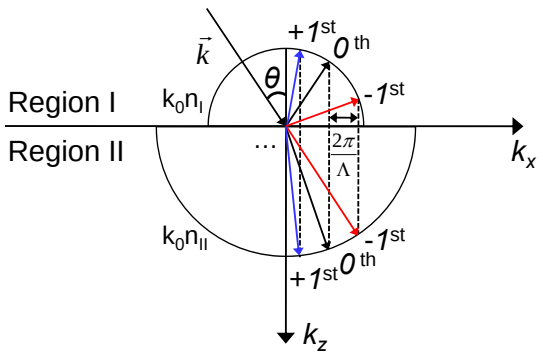

Figure 2.2: Phase-matching diagram for a diffraction grating with reflected and transmitted orders.

for the TM case and also for the general case, it is recommended to refer to [60]. The refractive index profile of the grating structure can be expanded with the harmonics of the fundamental spatial frequency as

$$\epsilon(\mathrm{x}) = \epsilon(\mathrm{x} + n\Lambda) = \sum_m \epsilon_m \exp\left[j\left(\frac{2\pi}{\Lambda}\right)m\right], \qquad 0 \leqq \mathrm{x} \leqq \Lambda, \tag{2.2}$$

where n is the integer number to express the periodic structure with Λ, ϵ_m is the m-th Fourier harmonic, m is the integer number of -$\infty \leqq m \leqq \infty$. For the numerical simulation, only a truncated number of harmonics is considered such as -M $\leqq m \leqq$ M. The Fourier harmonic components of a simple square gratings are given by

$$\epsilon_0 = \mathrm{n_H^2 f} + \mathrm{n_L^2}(1 - \mathrm{f}), \qquad \epsilon_m = (\mathrm{n_H^2} - \mathrm{n_L^2})\frac{\sin(m\pi \mathrm{f})}{m\pi}, \tag{2.3}$$

where ϵ_0 is the average relative permittivity of the single unit of grating, which consists of a high index (n_H) and a low index (n_L) grating bar, and the permeability for all materials is assumed to be 1. In region I and II, the reflected and transmitted field can be described using Rayleigh field expansion as [61]

$$E_{\mathrm{I,y}} = E_{inc,y} + \sum_m R_m \exp[-\mathrm{j}(\mathrm{k_{xm}} - \mathrm{k_{I,zm}z})], \qquad \mathrm{z} < 0, \tag{2.4}$$

$$E_{\mathrm{II,y}} = \sum_m T_m \exp\{-\mathrm{j}[\mathrm{k_{xm}x} - \mathrm{k_{II,zm}}(\mathrm{z} - \mathrm{d})]\}, \qquad \mathrm{z} > \mathrm{d}, \tag{2.5}$$

with

$$\mathrm{k_{xm}} = \mathrm{k_0}[\mathrm{n_I} \sin\theta - m(\lambda_0/\Lambda)], \tag{2.6}$$

where

$$\mathrm{k_{l,zm}} = \begin{cases} +\mathrm{k_0}[\mathrm{n_l^2} - (\mathrm{k_{xi}}/\mathrm{k_0})^2]^{(1/2)} & \mathrm{k_0 n_l} > \mathrm{k_{xm}}, \\ -\mathrm{jk_0}[(\mathrm{k_{xm}}/\mathrm{k_0})^2 - \mathrm{n_l^2}]^{(1/2)} & \mathrm{k_{xm}} > \mathrm{k_0 n_l}, \quad \mathrm{l} = \mathrm{I, II}. \end{cases}$$

The R_m and T_m are the amplitude of the m-th reflected and transmitted diffraction orders in region I and II, respectively. The corresponding magnetic fields can be calculated

$$\vec{H} = \left(\frac{\mathrm{j}}{\omega\mu}\right)\nabla \times \vec{E} \tag{2.7}$$

Depending on the angle and wavelength of the incident light as well as refractive indices of the incident (region I) and exit region (region II), higher orders (> 0-th

order) can be excited in region I and II as shown in Fig. 2.2, which satisfy Eq. (2.6). As shown in Fig. 2.2, if the spacial frequency of the grating, $2\pi/\Lambda$ is less than $k_0 n_I$ and $k_0 n_{II}$, then there can be propagating higher reflected and transmitted diffraction orders ($\pm$1-st, $\pm$2-nd, $\cdots$. orders).

If the grating period become shorter than the incident wavelength, then the number of higher diffraction orders (or propagating orders along the z-direction) become smaller accordingly. In the extreme condition, according to Eq. (2.6), if the grating period is smaller than the incident wavelength of λ_0 and the refractive indices of the incident and the exit medium are small enough, then the corresponding $k_{l,zm}$ become imaginary number as increasing the m-th order. It indicates that there is no propagating mode along the z-direction above m-th order from which it start having an imaginary propagation constant, but there can be energy flow along the x-direction inside the grating when guided-mode resonance condition is met. The most extreme case is shown in Fig. 2.3(a). In region I and II, only the 0-th order is excited. This condition is achieved when the grating surrounded by low-index materials. With the $|\vec{k}|$ of the incident wavelength, the upper and lower half circles should be smaller than the reciprocal vector of the 1D periodic grating as

$$k_0 n_I, \quad k_0 n_{II} \quad < \quad 2\pi/\Lambda. \tag{2.8}$$

In this case, the 0-th reflected and transmitted diffraction order are only propagating one. At this condition, only two grating modes may be propagating modes inside

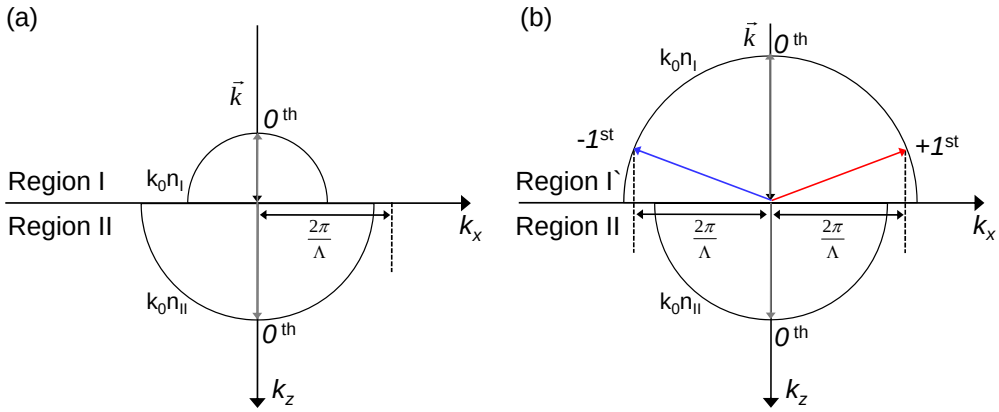

Figure 2.3: Phase-matching diagrams for a) a HCG and b) a HG reflector, respectively.

the grating region along the z-direction. Then, by exploiting the two modes via the grating parameters, the grating can work as high reflection, high transmission, or high-Q resonator [53]. For a high reflective purpose, HCG reflectors are representative example.

If there is a high-refractive-index layer (region I′) with a finite thickness on top of the grating, which is shown in Fig. 2.3(a), then the upper half-circle can be larger than the grating vector. Then, in region I′, higher reflected orders are excited as shown in Fig. 2.3(b). For instance, if a HCG reflector is integrated with a high-index-refractive index layer on top of it, then the surface normal reflectance will be deteriorated due to the ±1-st and more higher off-normal diffraction orders. Even though the excited higher orders in region I′ deteriorate the surface normal reflectance, if it is possible to secure these orders and re-guide them through the surface-normal direction with an in-phase condition, the cap layer and bottom grating together can work as a mirror. If the index of the cap and the grating condition is designed to excite only the ±1-st order in a specific wavelength range, then it become a new type of highly broadband mirror referred to as hybrid grating (HG) reflector [55]. The HG reflector will be discussed in more detail in Chapter 5.

2.2.2 Periodic single-block structure

Inside and near the grating, the incident electromagnetic fields propagating along the z-direction are distorted due to the different phase velocities ($\mathrm{v}_p = \mathrm{c}/\mathrm{n_H}$ or $\mathrm{c}/\mathrm{n_L}$) of the high index and low index grating bars. Since the grating structure is periodic, the distorted field can be expanded using Fourier series in terms of the space harmonics and it follows Bloch's condition [60]. All notations, which are used in this section, follow the notations in [60]. The distorted field inside the grating can be expressed as

$$E_{\mathrm{g,y}} = \sum_m S_{\mathrm{y,m}}(\mathrm{z})\exp(-\mathrm{j}\mathrm{k_{x,m}}\mathrm{x}), \tag{2.9}$$

$$H_{\mathrm{g,x}} = -\mathrm{j}\left(\frac{\epsilon_0}{\mu_0}\right)^{(1/2)} \sum_m U_{\mathrm{x,m}}(\mathrm{z})\exp(-\mathrm{j}\mathrm{k_{x,m}}\mathrm{x}). \tag{2.10}$$

where ϵ_0 and μ_0 are the permittivity and permeability of free space, and $S_{\mathrm{y,m}}$ and $U_{\mathrm{x,m}}$ are the m-th space harmonic fields. They meet the Maxwell's equation in the grating region as

$$\frac{\partial E_{\mathrm{g,y}}}{\partial z} = \mathrm{j}\,\omega\mu_0 H_{\mathrm{g,x}}, \tag{2.11}$$

$$\frac{\partial H_{\mathrm{g,x}}}{\partial z} = \mathrm{j}\,\omega\epsilon_0\epsilon_{\mathrm{x}} E_{\mathrm{g,y}} + \frac{H_{\mathrm{g,z}}}{\partial x}. \tag{2.12}$$

Then, after substituting Eqs. (2.9) and (2.10) into Eqs. (2.11) and (2.12), respectively, and removing the z-field component in Eq. (2.12), the coupled-wave equations become,

$$\frac{\partial S_{\mathrm{y,m}}}{\partial z} = \mathrm{k}_0\, U_{\mathrm{x,m}}, \tag{2.13}$$

$$\frac{\partial U_{\mathrm{x,m}}}{\partial z} = \left(\frac{\mathrm{k}_{\mathrm{x,m}}^2}{\mathrm{k}_0}\right) S_{\mathrm{y,m}} - \mathrm{k}_0 \sum_p \epsilon_{\mathrm{m-p}} \mathrm{S}_{\mathrm{y,p}}. \tag{2.14}$$

In matrix form for numerical calculation,

$$\begin{bmatrix} \partial \mathbf{S}_y/\partial(z') \\ \partial \mathbf{U}_x/\partial(z') \end{bmatrix} = \begin{bmatrix} \mathbf{0} & \mathbf{I} \\ \mathbf{A} & \mathbf{0} \end{bmatrix} \begin{bmatrix} \mathbf{S}_y \\ \mathbf{U}_x \end{bmatrix}, \tag{2.15}$$

where $z' = k_0 z$ and

$$\mathbf{A} = \mathbf{K}_x^2 - \mathbf{E}, \tag{2.16}$$

where $\mathbf{E}$ is the matrix consisted by the permittivity harmonics of ϵ(m-p) component, $\mathbf{K}_x$ is the diagonal matrix with diagonal components of $k_{x,m}/k_0$, and $\mathbf{I}$ is the identity matrix. All the matrix component are (2M+1 $\times$ 2M+1) matrices. After calculating the eigenvalues and eigenvectors of the matrix $\mathbf{A}$, the space harmonic component fields in the grating layer are expresses as,

$$S_{\mathrm{y,m}}(\mathrm{z}) = \sum_i w_{\mathrm{m,i}} \{c_{\mathrm{m}}^{+} \exp(-\mathrm{jk}_0 \mathrm{q_i z}) + c_{\mathrm{m}}^{-} \exp[\mathrm{jk}_0 \mathrm{q_i}(\mathrm{z-d})]\}, \tag{2.17}$$

$$U_{\mathrm{x,m}}(\mathrm{z}) = \sum_i v_{\mathrm{m,i}} \{c_{\mathrm{m}}^{+} \exp(-\mathrm{jk}_0 \mathrm{q_i z}) - c_{\mathrm{m}}^{-} \exp[\mathrm{jk}_0 \mathrm{q_i}(\mathrm{z-d})]\}, \tag{2.18}$$

where $w_{\mathrm{m,i}}$ is the element of the eigenvector matrix $\mathbf{W}$ and $\mathrm{q_i}$ is the positive square root of the eigenvalues of the matrix $\mathbf{A}$. The quantity $v_{\mathrm{m,i}}$ is the (m,i)

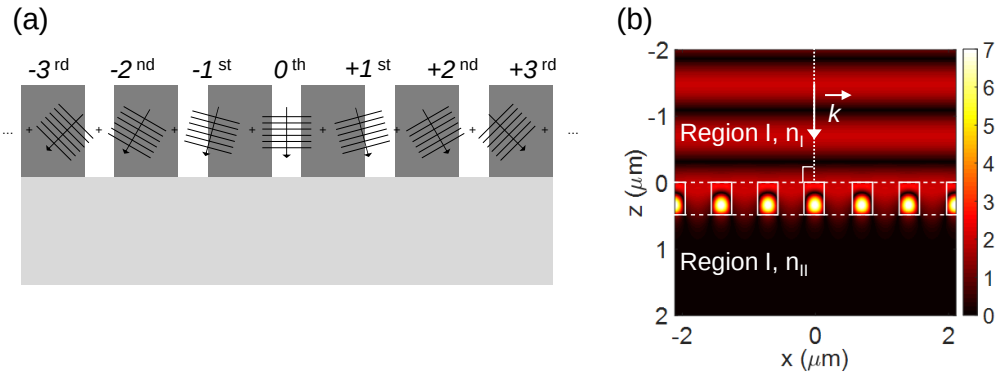

Figure 2.4: a) Schematic illustration of spatial harmonic components in the grating region excited by normal incident plane wave. b) Example of field amplitude profile of the periodic square grating (HCG case) for the normal incident plane wave.

matrix element of the matrix of

$$\mathbf{V} = \mathbf{WQ}, \tag{2.19}$$

where $\mathbf{Q}$ is the diagonal matrix with the element $\mathrm{q_i}$. The harmonic components describing the field inside the single period of the grating structure are illustrated on top of the infinite periodic grating in Fig. 2.4(a) and the simulated field profile of a HCG structure is shown in Fig. 2.4(b).

The two quantities of c_{m}^{+} and c_{m}^{-} in Eqs. (2.17) and (2.18) are the constants for going forward and going backward fields inside the grating and they are determined from the two boundary conditions of continuous transverse electric and magnetic fields. At the input boundary of $z = 0$,

$$\delta_{\mathrm{n0}} + R_n = \sum_m w_{\mathrm{n,m}}[c_{\mathrm{m}}^{+} + c_{\mathrm{m}}^{-}\exp(-\mathrm{j}k_0 q_{\mathrm{m}} d)], \tag{2.20}$$

$$\mathrm{j}[n_{\mathrm{I}}\cos\theta\delta_{\mathrm{n,0}} - (k_{\mathrm{I,zn}}/k_0)R_{\mathrm{n}}] = \sum_m v_{\mathrm{n,m}}[c_{\mathrm{m}}^{+} - c_m^{-}\exp(-\mathrm{j}k_0 q_{\mathrm{m}} d)], \tag{2.21}$$

or, in matrix form,

$$\begin{bmatrix} \delta_{\mathrm{n0}} \\ \mathrm{j}n_{\mathrm{I}}\cos\theta\delta_{\mathrm{n0}} \end{bmatrix} + \begin{bmatrix} \mathbf{I} \\ -\mathrm{j}\mathbf{Y}_{\mathrm{I}} \end{bmatrix} \begin{bmatrix} \mathbf{R} \end{bmatrix} = \begin{bmatrix} \mathbf{W} & \mathbf{WX} \\ \mathbf{V} & -\mathbf{VX} \end{bmatrix} \begin{bmatrix} \mathbf{c}^{+} \\ \mathbf{c}^{-} \end{bmatrix} \tag{2.22}$$

At the input boundary of $z = \mathrm{d}$,

$$\sum_m w_{\mathrm{n,m}}[c_{\mathrm{m}}^{+}\exp(-\mathrm{j}k_0 q_{\mathrm{m}} d) + c_{\mathrm{m}}^{-}] = T_{\mathrm{n}}, \tag{2.23}$$

$$\sum_m v_{\mathrm{n,m}}[c_{\mathrm{m}}^{+}\exp(-\mathrm{j}k_0 q_{\mathrm{m}} d) - c_{\mathrm{m}}^{-}] = \mathrm{j}(k_{\mathrm{II,zn}}/k_0)\, T_{\mathrm{n}}, \tag{2.24}$$

and the corresponding matrix equation are given by

$$\begin{bmatrix} \mathbf{WX} & \mathbf{W} \\ \mathbf{VX} & -\mathbf{V} \end{bmatrix} \begin{bmatrix} \mathbf{c}^{+} \\ \mathbf{c}^{-} \end{bmatrix} = \begin{bmatrix} \mathbf{I} \\ \mathrm{j}\mathbf{Y}_{\mathrm{II}} \end{bmatrix} \begin{bmatrix} \mathbf{T} \end{bmatrix} \tag{2.25}$$

where

$$\delta_{n0} = \begin{cases} 1 & n = 0 \\ 0 & n \neq 0. \end{cases}$$

The diagonal matrices of $\mathbf{X}$,$\mathbf{Y}_{\mathrm{I}}$, and $\mathbf{Y}_{\mathrm{II}}$ have the diagonal elements of $\exp(-\mathrm{k}_0 \mathrm{q}_m \mathrm{d})$, $(\mathrm{k}_{\mathrm{I},zn}/\mathrm{k}_0)$, and $(\mathrm{k}_{\mathrm{II},zn}/\mathrm{k}_0)$, respectively. Then, Eqs. (2.22) and (2.25) are solved simultaneously for the forward- and backward-diffracted amplitudes of T_n and R_n and the coupling coefficients ${c_m}^{+}$ and ${c_m}^{-}$. This is illustrated in Fig. 2.5(a). Figure 2.5(b) show the case when the incident light comes from the right-to-left direction.

The diffraction efficiencies for m-th reflected and transmitted orders are defined as [60],

$$\mathrm{DE}_{rm} = |R_m|^2 \mathbf{Re}\left(\frac{k_{\mathrm{I},zm}}{k_0 n_{\mathrm{I}} \cos\theta} \right), \tag{2.26}$$

$$\mathrm{DE}_{tm} = |T_m|^2 \mathbf{Re}\left(\frac{k_{\mathrm{II},zm}}{k_0 n_{\mathrm{I}} \cos\theta} \right). \tag{2.27}$$

For a lossless structure, the sum of total diffraction efficiencies should be conserved and it leads to this condition [60],

$$\sum_m \mathrm{DE}_{rm} + \mathrm{DE}_{tm} = 1. \tag{2.28}$$

After knowing all these four kinds of coefficients, the response of the incident electromagnetic fields to the periodic grating can be fully described. From the R_m and T_m, the forward- and backward-diffracted fields outside the grating structure are obtained, and the ${c_m}^{+}$ and ${c_m}^{-}$ describe the excited Bloch eigenmodes propagating forward and backward, respectively, inside the grating. For the same grating, if the incident field propagates from the opposite side, using the same manner, all the four kinds of coefficients can be obtained as shown in Fig. 2.5(b). Then, as shown in Fig. 2.5(c), the grating system can be fully addressed using $\mathbf{S}$ and $\mathbf{c}$ matrices obtained from the left-to-right and right-to-left propagating incident fields. When the refractive index of the single-block is assumed as a constant and surrounded by

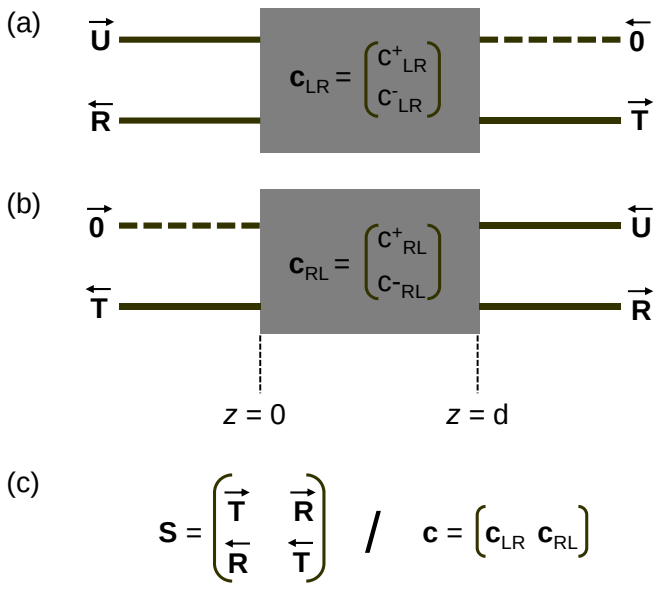

Figure 2.5: Schematic illustration of the single-block response using **S**-matrix components and coupling coefficients describing the interaction with the normalized incident fields and the structure. a) Left-to-right propagating case. b) Right-to-left propagating case. The arrows above the R and T coefficient matrices indicate the direction of the forward- and backward-diffracted fields. c) **S** matrix and **c** matrix fully describing the system response inside (**c** matrix) and outside (**S** matrix) of the single block interacting with the incident light.

the same material in the left and right sides then, the **S** matrix and the **c** matrix are fully obtained from the left-to-right or right-to-lest response due to the symmetry.

2.2.3 Two-block structure

For two-block structure including unpatterned (i.e. DBRs and III-V layer) and patterned (i.e. HCGs) single block along transverse directions (x- and y-direction), the **S** and **c** matrix for the two-block system, which represent the entire system as as a single block, is required. The system response of the two-block structure can be obtained from the responses of each layer, which is surrounded by vacuum [69, 70]. For the two-block structure, the coupling coefficients of $\mathbf{c}_{\mathrm{LR}}$ and $\mathbf{c}_{\mathrm{RL}}$ connect the adjacent two layers at the boundary, and the **R** and **T** for the left-to-right or right-to-left are obtained after considering the infinite reflection and transmission processes at the multiple boundaries. To handle the infinite processes between the boundaries, a zero-distance concept is employed [69, 70] and the **R** and **T** can be

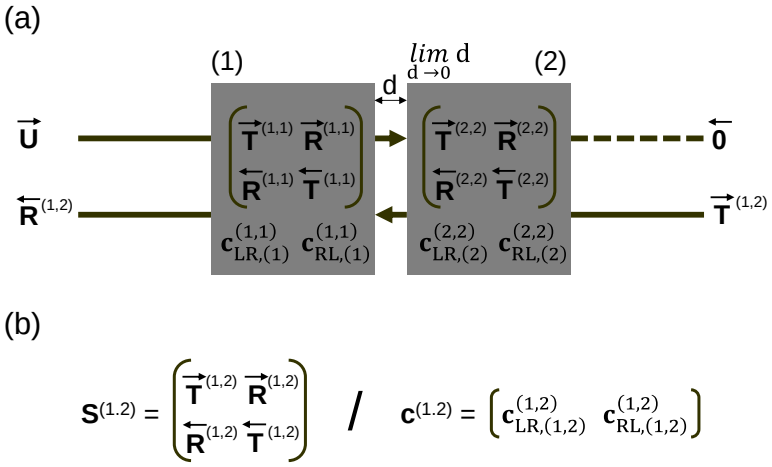

Figure 2.6: (a) Illustration of two-block system with the zero-distance concept. (left-to-right direction illustrated only.) (b) The two-block **S** matrix and **c** matrix indicated with the superscript and subscript (1,2).

thought as the result after reaching the steady state.

As shown in Fig. 2.6, each block is indicated as number of '(1)' and '(2)' [69, 70]. Inside the block, the **S** matrices and **c** matrices are indicated with the numbering system. The superscripts indicate the total number of blocks and the subscripts show the local block. The **S** matrix inside each block consists of the same number pair which indicates the single-block **S** matrix and **c** matrix explained the previous subsection. In the input and output ports, the superscript,(1,2) indicates that $\overleftarrow{\mathrm{R}}$ and $\overrightarrow{\mathrm{T}}$ are the responses of the two-block system. The *imaginary distance* 'd' is introduced through the limiting process to explain the zero-distance concept [69,70].

First, S-matrix components of the single layer '(1)' and '(2)' are calculated. Using the two S-matrix components, the infinite multiple reflection processes can be obtained taking infinite sum. In here, the infinite processes are conducted by approaching the 'd' as '0'. Therefore, there is 'no' *physical distance* and no phase delay is introduced [69, 70]. The infinite processes are expressed using the sum of bi-directional reflection processes between the boundary using $\overleftarrow{\mathbf{R}}$ and $\overrightarrow{\mathbf{R}}$. Then,

the S-matrix component of the two-block structure can be written as

$$\overleftarrow{\mathbf{R}}^{(1,2)} = \overleftarrow{\mathbf{R}}^{(1,1)} + \overleftarrow{\mathbf{T}}^{(1,1)}\left[\sum_{k=0}^{\infty}\left(\overleftarrow{\mathbf{R}}^{(2,2)}\overrightarrow{\mathbf{R}}^{(1,1)}\right)^{k}\right]\overleftarrow{\mathbf{R}}^{(2,2)}\overrightarrow{\mathbf{T}}^{(1,1)} \tag{2.29a}$$

$$\overrightarrow{\mathbf{T}}^{(1,2)} = \overrightarrow{\mathbf{T}}^{(2,2)}\left[\sum_{k=0}^{\infty}\left(\overrightarrow{\mathbf{R}}^{(1,1)}\overleftarrow{\mathbf{R}}^{(2,2)}\right)^{k}\right]\overrightarrow{\mathbf{T}}^{(1,1)} \tag{2.29b}$$

$$\overrightarrow{\mathbf{R}}^{(1,2)} = \overrightarrow{\mathbf{R}}^{(2,2)} + \overrightarrow{\mathbf{T}}^{(2,2)}\left[\sum_{k=0}^{\infty}\left(\overrightarrow{\mathbf{R}}^{(1,1)}\overleftarrow{\mathbf{R}}^{(2,2)}\right)^{k}\right]\overrightarrow{\mathbf{R}}^{(1,1)}\overleftarrow{\mathbf{T}}^{(2,2)} \tag{2.29c}$$

$$\overleftarrow{\mathbf{T}}^{(1,2)} = \overleftarrow{\mathbf{T}}^{(1,1)}\left[\sum_{k=0}^{\infty}\left(\overleftarrow{\mathbf{R}}^{(2,2)}\overrightarrow{\mathbf{R}}^{(1,1)}\right)^{k}\right]\overleftarrow{\mathbf{T}}^{(2,2)}, \tag{2.29d}$$

where the superscript (1,2) of the S-matrix components indicates the interconnected two-block **S** matrix of the layer (1) and layer (2) [70]. The infinite sums in Eqs. (2.29a-2.29d) can be considered as a geometric series with a common ratio of $\overrightarrow{\mathbf{R}}^{(1,1)}\overleftarrow{\mathbf{R}}^{(2,2)}$. The geometric series can be converged to a finite number because the common ratio is less than 1 and the summations become simplified using the sum rule of the geometric series as [70],

$$\sum_{k=0}^{\infty}\left(\overrightarrow{\mathbf{R}}^{(1,1)}\overleftarrow{\mathbf{R}}^{(2,2)}\right)^{k} = \lim_{k\to\infty}\frac{\mathbf{I}-(\overrightarrow{\mathbf{R}}^{(1,1)}\overleftarrow{\mathbf{R}}^{(2,2)})^{k}}{\mathbf{I}-\overrightarrow{\mathbf{R}}^{(1,1)}\overleftarrow{\mathbf{R}}^{(2,2)}} = \frac{\mathbf{I}}{\mathbf{I}-\overrightarrow{\mathbf{R}}^{(1,1)}\overleftarrow{\mathbf{R}}^{(2,2)}}. \tag{2.30}$$

The convergence is direct result from the law of the energy conservation as well. Then, substituting Eq. (2.30) into (2.29a-2.29d) [69, 70],

$$\overleftarrow{\mathbf{R}}^{(1,2)} = \overleftarrow{\mathbf{R}}^{(1,1)} + \overleftarrow{\mathbf{T}}^{(1,1)}\left[\mathbf{I}-\overleftarrow{\mathbf{R}}^{(2,2)}\overrightarrow{\mathbf{R}}^{(1,1)}\right]^{-1}\overleftarrow{\mathbf{R}}^{(2,2)}\overrightarrow{\mathbf{T}}^{(1,1)} \tag{2.31a}$$

$$\overrightarrow{\mathbf{T}}^{(1,2)} = \overrightarrow{\mathbf{T}}^{(2,2)}\left[\mathbf{I}-\overrightarrow{\mathbf{R}}^{(1,1)}\overleftarrow{\mathbf{R}}^{(2,2)}\right]^{-1}\overrightarrow{\mathbf{T}}^{(1,1)} \tag{2.31b}$$

$$\overrightarrow{\mathbf{R}}^{(1,2)} = \overrightarrow{\mathbf{R}}^{(2,2)} + \overrightarrow{\mathbf{T}}^{(2,2)}\left[\mathbf{I}-\overrightarrow{\mathbf{R}}^{(1,1)}\overleftarrow{\mathbf{R}}^{(2,2)}\right]^{-1}\overrightarrow{\mathbf{R}}^{(1,1)}\overleftarrow{\mathbf{T}}^{(2,2)} \tag{2.31c}$$

$$\overleftarrow{\mathbf{T}}^{(1,2)} = \overleftarrow{\mathbf{T}}^{(1,1)}\left[\mathbf{I}-\overleftarrow{\mathbf{R}}^{(2,2)}\overrightarrow{\mathbf{R}}^{(1,1)}\right]^{-1}\overleftarrow{\mathbf{T}}^{(2,2)}. \tag{2.31d}$$

The two-block **S** matrix is composed of the S-matrix components of each single block of layer '(1)' and '(2)' and this relation is mathematically calculated using Redheffer star product. The **S** matrix of the two-block system is then written as

$$\mathbf{S}^{(1,2)} = \begin{pmatrix}\overrightarrow{\mathbf{T}}^{(1,2)} & \overrightarrow{\mathbf{R}}^{(1,2)} \\ \overleftarrow{\mathbf{R}}^{(1,2)} & \overleftarrow{\mathbf{T}}^{(1,2)}.\end{pmatrix} \tag{2.32}$$

Using the Redheffer star product notation, it can be expressed as

$$\mathbf{S}^{(1,2)} = \mathbf{S}^{(1,1)} * \mathbf{S}^{(2,2)}, \tag{2.33}$$

where '*' indicates the Redheffer star product [69, 70].

To describe the internal Bloch's eigenmodes of the two-block structure, the coupling coefficient can be calculated using the concept of the infinite summation in Eq. (2.30) and can be shortly expressed using the Redheffer star product. The set of the two-block coupling coefficients are written as

$$\mathbf{c}^{(1,2)}_{\mathrm{LR},(1,2)} = \left\{\mathbf{c}^{(1,2)}_{\mathrm{LR},(1)}, \mathbf{c}^{(1,2)}_{\mathrm{LR},(2)}\right\} \tag{2.34a}$$

$$\mathbf{c}^{(1,2)}_{\mathrm{RL},(1,2)} = \left\{\mathbf{c}^{(1,2)}_{\mathrm{RL},(1)}, \mathbf{c}^{(1,2)}_{\mathrm{RL},(2)}\right\}, \tag{2.34b}$$

where the superscript (1,2) indicates the interconnected two-block and the subscripts of (1) and (2) indicate the interconnected coupling coefficient of the two-block system in the layer of (1) and (2), respectively [69, 70]. Each coefficient can be properly calculated using the concept of the infinite reflection process as

$$\mathbf{c}^{(1,2)}_{\mathrm{LR},(1)} = \mathbf{c}^{(1,1)}_{\mathrm{LR},(1)} + \mathbf{c}^{(1,1)}_{\mathrm{RL},(1)}\left(\mathbf{I} - \overleftarrow{\mathbf{R}}^{(2,2)}\overrightarrow{\mathbf{R}}^{(1,1)}\right)^{-1}\overleftarrow{\mathbf{R}}^{(2,2)}\overrightarrow{\mathbf{T}}^{(1,1)} \tag{2.35a}$$

$$\mathbf{c}^{(1,2)}_{\mathrm{RL},(1)} = \mathbf{c}^{(1,1)}_{\mathrm{RL},(1)}\left(\mathbf{I} - \overleftarrow{\mathbf{R}}^{(2,2)}\overrightarrow{\mathbf{R}}^{(1,1)}\right)^{-1}\overleftarrow{\mathbf{T}}^{(2,2)} \tag{2.35b}$$

$$\mathbf{c}^{(1,2)}_{\mathrm{LR},(2)} = \mathbf{c}^{(2,2)}_{\mathrm{LR},(2)}\left(\mathbf{I} - \overrightarrow{\mathbf{R}}^{(1,1)}\overleftarrow{\mathbf{R}}^{(2,2)}\right)^{-1}\overrightarrow{\mathbf{T}}^{(1,1)} \tag{2.35c}$$

$$\mathbf{c}^{(1,2)}_{\mathrm{RL},(2)} = \mathbf{c}^{(2,2)}_{\mathrm{RL},(2)} + \mathbf{c}^{(2,2)}_{\mathrm{LR},(2)}\left(\mathbf{I} - \overrightarrow{\mathbf{R}}^{(1,1)}\overleftarrow{\mathbf{R}}^{(2,2)}\right)^{-1}\overrightarrow{\mathbf{R}}^{(1,1)}\overleftarrow{\mathbf{T}}^{(2,2)}. \tag{2.35d}$$

This relation is now expressed by using the Redheffer star product [69, 70], and it is given as

$$\left(\mathbf{c}^{(1,2)}_{\mathrm{LR},(1,2)}, \mathbf{c}^{(1,2)}_{\mathrm{RL},(1,2)}\right) = \left(\mathbf{c}^{(1,1)}_{\mathrm{LR},(1)}, \mathbf{c}^{(1,1)}_{\mathrm{RL},(1)}\right) * \left(\mathbf{c}^{(2,2)}_{\mathrm{LR},(2)}, \mathbf{c}^{(2,2)}_{\mathrm{RL},(2)}\right). \tag{2.36}$$

To interconnect the two-block structure with the left and right half-infinite layers (region I and II), the same algorithm, which is used to connect two blocks, can be used [69,70], and then reflectance, transmittance, and field profiles of a multi-layered structure can be calculated. Based on the RCWA method, MATLAB RCWA code is used to plot total filed profile and decomposed field profile, and a freely available RCWA tool, RODIS[1]is used to calculate reflectance and transmittance as well. For the general case of a multi-block structure, it is briefly explained in Appendix A.

[1]RODIS is available at http://photonics.intec.ugent.be/research/facilities/design/rodis/default.htm.

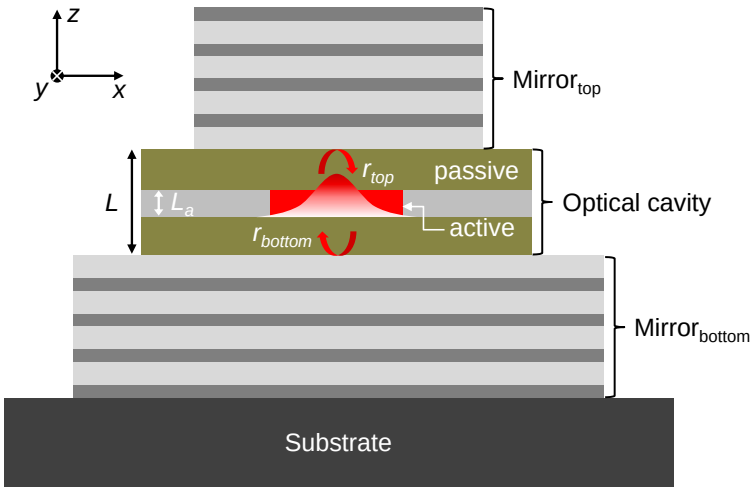

Figure 2.7: Schematic illustration of a VCSEL.

2.3 DBR, HCG, and HG Mirror

The lasing condition of a laser is determined by two factors: 1) amplitude and 2) phase conditions. The amplitude condition indicates that during one round trip of light inside the optical cavity, it should be equal to unity. It means that all possible losses should be retrieved at a gain region. In addition, during the round trip, the phase condition should satisfy the integer multiple of 2π. These two conditions are intimately related to the mirrors, which surround the optical cavity, in terms of reflectivity and phase.

For a VCSEL as shown in Fig. 2.7, the light will be bounced up and down inside the vertical cavity, and it will be lased if the lasing condition meet. As an illustration, the excited fundamental mode is described as well. For VCSEL applications, the top and bottom mirror should have high reflectivity because of the extremely short thickness of the active region along the vertical direction [20, 51]. It is required to have more than 99.5% reflectance [27]. The phase change resulted from the propagation into the mirrors needs to be considered as well because it will determine the lasing wavelength.

The lasing mode in a laser can be described by the space-time electric field with y-direction polarization as

$$\mathcal{E} = \hat{e}_y E_0 U(x,y) e^{j(\omega t - \tilde{\beta} z)}, \tag{2.37}$$

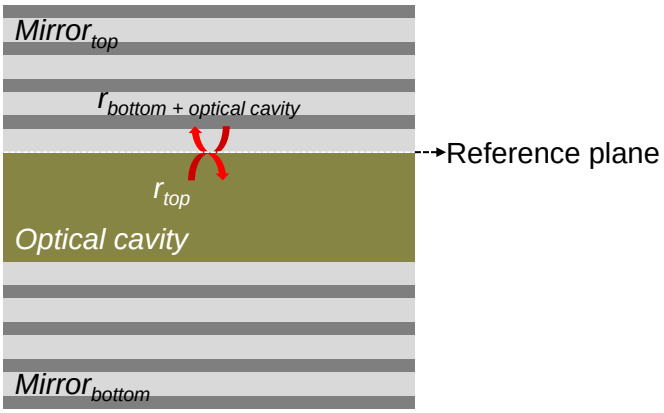

Figure 2.8: Schematic illustration of reference plane to find a vertical resonance condition by using two section structure.

where $\hat{e}_y$ is the unit vector along the y-direction, E_0 is the magnitude of the field, and $U(x,y)$ is the normalized transverse electric profile [38]. In the exponential term, ω is the angular frequency and $\tilde{\beta}$ is the complex propagation constant depending on a lossy or a gain material or a lossy structure. The complex propagation constant can be rewritten in terms of the real and imaginary part as

$$\tilde{\beta} = \beta + j(\Gamma_{xy} g - \alpha_i)/2, \tag{2.38}$$

where β is the real number of the propagation constant defined as $2\pi\bar{n}/\lambda$ using an effective index of $\bar{n}$, Γ_{xy} is the transverse confinement factor, g is the material gain, and α_i is the internal modal loss including scattering and absorption losses. Then, the lasing condition, which include the amplitude and phase condition to reach a threshold level at a reference plane inside the optical cavity as shown in Fig. 2.8, is given by [38]

$$r_t r_{b+cav} = 1, \tag{2.39}$$

where r_t and r_{b+cav} are the complex reflectance seen from the reference plane, which are boundary between the top mirror and the optical cavity. The r_{b+cav} includes gain and loss terms of the cavity. By separating the bottom and the cavity, the lasing condition can be rewritten as

$$r_t r_b e^{-j2\tilde{\beta}_{a,th} L_a} e^{-j2\tilde{\beta}_{p,th} L_p} = 1, \tag{2.40}$$

where r_t and r_b are the complex mirror reflection coefficients for the top and bottom mirrors seen from the optical cavity, $\tilde{\beta}_{a,th}$ and $\tilde{\beta}_{p,th}$ are the complex propagation constants for the active and passive region of the cavity at the threshold, L_a is the thickness of the active region, and L_p is the thickness of the passive region which is the length of the passive part of the optical cavity given by L - L_a and the L is the thickness of the total optical cavity as shown in Fig. 2.7. The complex terms can be rewritten as

$$r_t = |r_{t,\alpha}|\, e^{-j\varphi_t}, \tag{2.41}$$

$$r_b = |r_{b,\alpha}|\, e^{-j\varphi_b}, \tag{2.42}$$

$$\tilde{\beta}_{a,th} = \beta_{a,th} + j(\Gamma_{xy} g - \alpha_{i,a})/2, \tag{2.43}$$

$$\tilde{\beta}_{p,th} = \beta_{p,th} + j(-\alpha_{i,p})/2. \tag{2.44}$$

The top and bottom complex reflection coefficients in Eqs. (2.41) and (2.42) consist of the amplitude terms of $|r_{t,\alpha}|$ and $|r_{b,\alpha}|$, which include internal mirror losses, respectively, and the corresponding phase terms of φ_t and φ_b.

2.3.1 Phase penetration depth

The mirrors are not reflecting light instantaneously, but there is some time delay to reach a specific reflectance level. The time delay is related to [52]

$$\tau = -\frac{\partial \varphi(\omega)}{\partial \omega}\bigg|_{\omega=\omega_0}, \tag{2.45}$$

where τ is the delay time, φ is the phase and ω is the angular frequency. If the mirrors have high and uniform reflectance as well as linear variation of phase near the design wavelength, the mirrors can be approximated as linear phase mirrors by transferring the delay time, τ into the penetration depth, l_p as shown in Fig. 2.9 [52].

In case of a DBR, it consists of high- and low-index material with a quarter-wave thickness of a design wavelength which is the same as the Bragg wavelength. Since the phase variation is linear around the Bragg frequency [52], the phase deviation from the Bragg frequency, ω_0 can be linearly approximated as

$$\Delta\varphi \approx \Delta\omega\left(- \frac{\partial \varphi(\omega)}{\partial \omega}\bigg|_{\omega=\omega_0}\right) = \Delta\omega\tau, \tag{2.46}$$

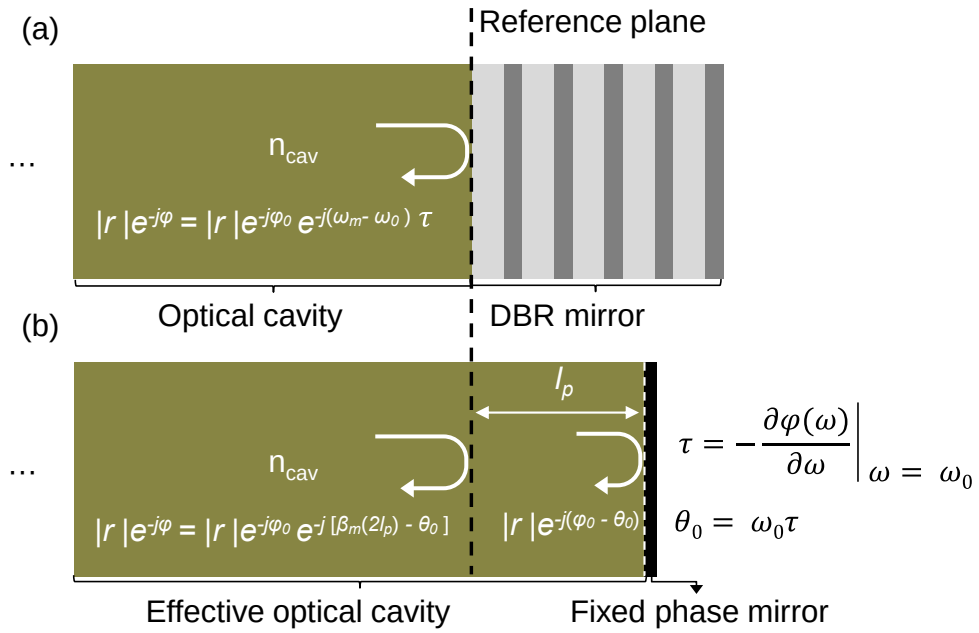

Figure 2.9: Schematic illustration of (a) a real mirror and (b) an equivalent mirror model with an one-sided optical cavity. (a) The DBR mirror expressed with a delay time, τ. (b) The equivalent mirror model with the fixed phase, θ_0 and the penetration depth, l_p.

where the $\Delta\omega$ is the angular frequency difference between a ω and ω_0 and τ is the delay time due to the reflection delay at ω_0. Then, the penetration depth can be expressed with the delay time, τ and the effective index, n_{cav} as

$$l_p = \frac{1}{2}\frac{c}{n_{cav}}\left(-\left.\frac{\partial\varphi(\omega)}{\partial\omega}\right|_{\omega=\omega_0}\right) = \frac{1}{2}v_{cav}\tau, \tag{2.47}$$

where n_{cav} is the refractive index of the optical cavity. Since the phase delay is due to the round trip inside the mirror, the 1/2 is multiplied. Then, near the Bragg wavelength of the DBR, the total phase term of the mirror with l_p and θ_0 can be approximated as

$$\begin{aligned}
\varphi &\approx \varphi_0 + \Delta\varphi \\
&= \varphi_0 + \Delta\omega\left(-\left.\frac{\partial\varphi(\omega)}{\partial\omega}\right|_{\omega=\omega_0}\right) \\
&= \varphi_0 + (\omega_m - \omega_0)\tau \\
&= \varphi_0 + (\beta_m - \beta_0)(2l_p) \\
&= \varphi_0 + \beta_m(2l_p) - \theta_0,
\end{aligned} \tag{2.48}$$

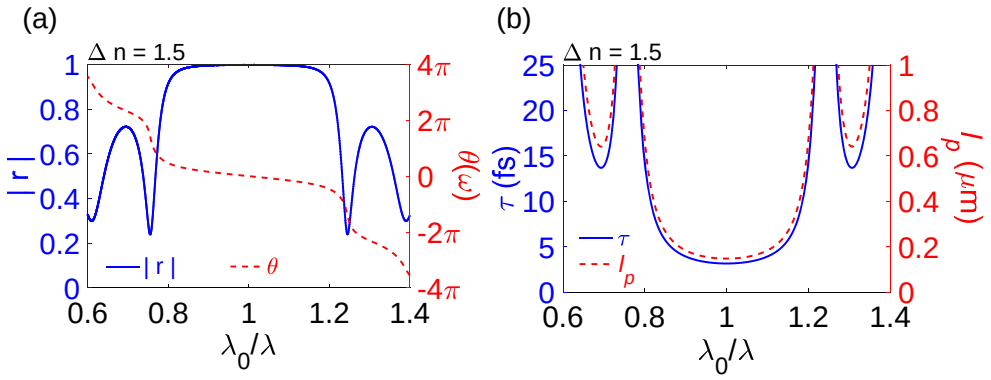

Figure 2.10: (a) Calculated amplitude and phase of reflection spectra of a dielectric DBR structure with Δn = 1.5 and (b) corresponding reflection delay time [52].

where φ_0 is the phase change from the DBR at the Bragg wavelength which is 0 or π depending on a refractive index of the cavity, and ω_m is the angular frequency of the m-th lasing modes, ω_0 is the angular frequency of the fundamental lasing mode which is the same as the Bragg frequency of the DBR, β_m (= $n_{cav}\omega_m/c$) and β_0 (= $n_{cav}\omega_0/c$) are the corresponding propagation constants, l_p is the effective penetration depth of the mirror because of the delayed reflection and θ_0 is the additional phase term to conserve the original mirror condition at the Bragg frequency [42].

Figure 2.10 shows the calculated amplitude and phase of reflection spectra of a DBR centered at 1.3 μm and the corresponding delay time and penetration depth using the same parameters in [42]. The DBR consists of 5 pair Si_3N_4/Si($n_{Si_3N_4}$ = 2.0/n_{Si} = 3.5) layers on a InP (n_{InP} = 3.2) and the DBR is surrounded by air (n_{air} = 1). The index contrast (Δn), which is defined as the index difference between the high and low index layer, of the dielectric DBR is 1.5. Near the normalized center frequency, the reflectivity is close to unity and almost constant, and the phase varies linearly as shown in Fig. 2.10(a). The calculated delay time and the phase penetration depth are shown in Fig. 2.10(b) and the minimum is at the center frequency or the Bragg frequency. In case of a DBR with Δn = 0.6, even though the DBR is designed for the same center frequency, the region of high reflectivity and linear phase variation become narrower, and the delay time and the corresponding penetration depth are increased as shown in Fig. 2.11.

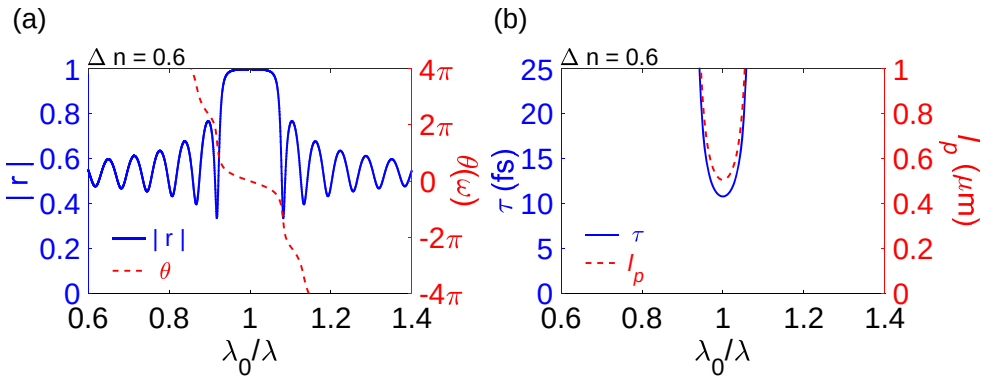

Figure 2.11: (a) Calculated amplitude and phase of reflection spectra of a DBR structure with Δn = 0.6 and (b) corresponding reflection delay time.

The m-th lasing mode can be excited within the high and uniform reflectance region of the linear phase mirror when it meets the lasing condition of Eq. (2.39). As an illustration, by simplifying the optical cavity with a single material surrounded by the same top and bottom DBR mirrors, the phase condition can be written as

$$2\varphi_0 + 2\beta_m(L + 2l_p) - 2\omega_0\tau = 2\pi m, \qquad m = 1, 2, 3, \cdots . \tag{2.49}$$

Especially, at the Bragg frequency of ω_0, if the resonance frequency of the optical cavity is designed as to have the same frequency as ω_0, then the lasing frequency is kept even though the l_p is changed. Therefore, the phase condition of the lasing frequency is determined solely by the optical cavity such as

$$2\beta_m L = 2\pi m, \qquad m = 1, 2, 3, \cdots . \tag{2.50}$$

If the phase condition is deviated from the Bragg frequency, the lasing wavelength will be varied according to the slope of the phase variation or the penetration depth. The phase penetration concept can be used to the other types of mirrors such as HCG and HG reflectors to estimate the phase condition of the optical cavity and to estimate the tunability of a laser [71]. The steeper the slope, the faster change the lasing wavelength.

2.3.2 Energy penetration depth

The other property which characterizes a mirror is its energy penetration depth, l_e. It shows how much energy is distributed in the mirror [52, 63, 72]. The energy

penetration depth can be related to the vertical confinement factor (Γ_z) of a vertical cavity laser [52]. In case of DBR mirrors, the distributed reflection process in a DBR along the vertical direction can be related to the the energy distribution inside the mirror because the field propagating back and forth inside DBR will transfer energy. Since the delay time due to the distributed reflection process is a function of Δn, the energy penetration depth depends on the Δn as well [52, 72]. For the DBR, the energy penetration depth is defined as the length where the incident field intensity decreases to |1/e| [72]. If a DBR has a large Δn, then the phase and energy penetration depths converge fast as increasing the number of pair of DBR [52]. For a DBR with a high Δn such as a dielectric DBR for VCSEL applications, the phase and the energy penetration depths are almost same. The analytical expression for energy penetration depth of DBR structure is given as [52]

$$l_e = \frac{\lambda_0}{4n_{cav}}\Lambda, \tag{2.51}$$

with

$$\Lambda = \frac{q}{1-p}\frac{(1+a^2p^{m-1})(1-p^m)}{1+q^2a^2p^{2m-2}}, \tag{2.52}$$

where λ_0 is the center wavelength (or Bragg wavelength) and q, p, and a are given by,

$$q = \frac{\mathrm{n_{L,inc}}}{\mathrm{n_{H,inc}}}, \qquad p = \frac{\mathrm{n_L}}{\mathrm{n_H}}, \qquad a = \frac{\mathrm{n_{L,exit}}}{\mathrm{n_{H,exit}}}, \tag{2.53}$$

where q is the ratio of refractive index between the incident medium and the first layer of the DBR, p is the ratio between the low and high index material of the DBR, and a is the ratio between the last layer of the DBR and the exit medium, and all the ratios are defined as low over high index which are always less than 1 [52].

For the other type of mirrors such as HCG and HG mirrors, the correlation between the phase penetration depth calculated from the delay time and the energy penetration depth is not necessary correlated [63, 72] because the reflection process involved in the mirrors is different. For the HCG or HG mirrors, the highly broadband reflection is involved with guided-mode resonances (GMRs) [63, 72] which occurs along the in-plane direction. The energy penetration depth, then, cannot be defined as the length of |1/e| inside the mirror because the GMRs are excited inside

the HCG or HG mirror, which can be larger than the incident field [72]. Then, as a simple estimation, the energy penetration depth is given as

$$T = 1 - R = \exp(-\frac{h}{l_e}), \tag{2.54}$$

where T is the transmittance, R is the reflectance and h is the mirror thickness [72]. However, this simple expression cannot distinguish the essential difference between transverse electric (TE) and transverse magnetic (TM) HCG reflectors because this expression ignores the different length of extended evanescent field in region II even though both reflectors have the same reflectance [73]. Since the length of the evanescent tail can influence the energy penetration depth, Eq. 2.54 cannot be used to estimate the vertical confinement. The energy penetration depth is directly found from the numerical simulation. The more detail about the influence of the evanescent field of the two HCG mirrors on the energy penetration depth will be discussed in Chapter 4.

The energy penetration depth of is considered when the longitudinal confinement factor is calculated and the total length including the energy penetration depth along the longitudinal direction is given by

$$L_{eff,e} = L_{cavity} + l_{e,top} + l_{e,bottom}, \tag{2.55}$$

where L_{cavity} is the length of the cavity region (which is previously defined as L) and $l_{e,top}$ and $l_{e,bottom}$ are the energy penetration depth for the top and bottom mirrors, respectively. The total length is used to calculate a modal gain. To simplify, it is assumed that group velocity and refractive index variation inside the optical cavity are small enough to ignore the variation, then the modal gain can be calculated as [38]

$$< g >= g\frac{\int_{L_a} \left|\mathcal{E}^+ + \mathcal{E}^-\right|^2 \mathrm{d}V}{\int_{L_{eff,e}} \left[\left|\mathcal{E}_T^+\right|^2 + \left|\mathcal{E}_T^-\right|^2\right] \mathrm{d}V} = \Gamma_{xy}\Gamma_z g = \Gamma g, \tag{2.56}$$

where g is the material gain, Γ_{xy} is the transverse confinement factor, Γ_z is the longitudinal confinement factor, and Γ is the confinement factor. According Eq. (2.56), if the bottom and top mirrors are designed to squeeze the energy penetration depth further, then the modal gain will be increased and the threshold condition will be alleviated.

2.3.3 Laser threshold condition

Two different types of mirror can be used for a long-wavelength vertical cavity lasers such as a top dielectric DBR and a bottom HCG reflector to replace a thick epitaxial DBR. The reflectance and phase of the two mirrors are used to calculate the lasing condition. The complex reflection coefficient terms in Eqs. (2.41) and (2.42) can be rewritten as

$$r_t = |r_{t,\alpha}|\, e^{-j\varphi_t} \approx |r_{t,\alpha}|\, e^{-j[\varphi_{0,t}+(\beta_m-\beta_0)(2l_{p,t})]}, \tag{2.57}$$

$$r_b = |r_{b,\alpha}|\, e^{-j\varphi_b} \approx |r_{b,\alpha}|\, e^{-j[\varphi_{0,b}+(\beta_m-\beta_0)(2l_{p,b})]}. \tag{2.58}$$

The amplitude of the reflection coefficients in Eqs. (2.57) and (2.58) can be rewritten by explicitly separating the loss terms inside the mirror as

$$|r_{t,\alpha}| = |r_t|\, e^{-\alpha_t(2l_{p,t})} \tag{2.59}$$

$$|r_{b,\alpha}| = |r_b|\, e^{-\alpha_b(2l_{p,b})}, \tag{2.60}$$

where the $|r_t|$ and $|r_b|$ are the reflection coefficients without any loss, α_t and α_b are the top and bottom mirror loss terms, respectively. Usimg Eqs. (2.59) and (2.60), the amplitude and and phase condition are obtained as

$$|r_{t,\alpha}|\, |r_{b,\alpha}|\, e^{(\Gamma_{xy}g_{th}-\alpha_{i,a})L_a} e^{-\alpha_{i,p}L_p} = 1, \tag{2.61}$$

$$\varphi_t + \varphi_b + 2\beta_{th,a}L_a + 2\beta_{th,p}L_p = 2m\pi, \quad m = 1, 2, \cdots. \tag{2.62}$$

where the propagation constants are corresponding to the m-th order. The amplitude and phase equations can be rewritten including the two penetration depths of l_ps. For the amplitude condition, it can be written as

$$\begin{aligned} &|r_t|\, |r_b| \\ &\qquad \times e^{(\Gamma_{xy}g_{th}-\alpha_{i,a})L_a} e^{-<\alpha_{i,p}>(L_p+2l_{p,t}+2l_{p,b})} = 1, \end{aligned} \tag{2.63}$$

and all losses are averaged out as $<\alpha_i>$ and the total length along the axial direction is defined as an effective cavity length,

$$|r_t|\, |r_b| \times e^{\Gamma_{xy}g_{th}L_a} e^{-<\alpha_i>(L_{eff,p})} = 1. \tag{2.64}$$

with

$$L_{eff,p} = L + l_{p,t} + l_{p,b}. \tag{2.65}$$

After taking logarithm of both sides of Eq. (2.64), $\Gamma_{xy}\mathrm{g}_{th}\mathrm{L}_a$ is given by

$$\Gamma_{xy} g_{th} L_a =< \alpha_i > L_{eff,p} + \ln \frac{1}{|\mathrm{r_t}|\,|\mathrm{r_b}|}. \tag{2.66}$$

For the phase condition of a general case, Eq. (2.62) can be explicitly rewritten as

$$\begin{aligned} &\left[\varphi_{0,t}+\beta_{m,t}(2l_{p,t}) - \theta_{0,t}\right] \\ &\quad + \left[\varphi_{0,b} + \beta_{m,b}(2l_{p,b}) - \theta_{0,b}\right] \\ &\qquad + 2\beta_{th,a}L_a + 2\beta_{th,p}L_p = 2m\pi, \qquad m = 1, 2, \cdots . \end{aligned} \tag{2.67}$$

As indicated in Eqs. (2.66) and (2.67), the phase penetration depths into the top and bottom mirror are involved with the threshold and phase condition, respectively.

2.3.4 Dynamic characteristic of laser

Since VCSLEs have a small cavity, it possesses high intrinsic response or high 3 dB bandwidth (f_{3dB}). However, for the conventional long-wavelength VCSEL with epitaxial DBRs, the small Δn is a hurdle to increase the 3 dB bandwidth because the energy penetration depths into mirrors are lengthy, which cause a larger mode volume along the vertical direction. To take the advantage of VCSELs operating at the long wavelength, it should have a small mode volume for the high-speed operation. Therefore, the design of long wavelength VCSEL focusing on the mirror part is essential to reduce the mode volume by suppressing the energy penetration depth into a top and a bottom mirror, respectively. The energy penetration depth is related to the intrinsic characteristic of lasers in terms of the relaxation resonance frequency, ω_R as,

$$\omega_R = \left[\frac{\Gamma v_g a}{qV}\eta_i(\mathrm{I} - \mathrm{I}_{th})\right]^{1/2}, \tag{2.68}$$

where Γ is the confinement factor, v_g is the group velocity, a is the differential gain, η_i is the injection efficiency, and I and I_{th} is the current and the threshold current.

The photon density distributed along the longitudinal direction is related to the longitudinal confinement factor, Γ_L through the energy penetration depth of l_e as

$$L_{eff,e} = L_{cav} + l_{e,t} + l_{e,b} \rightarrow \Gamma_L, \tag{2.69}$$

where $l_{e,t}$ and $l_{e,b}$ are the energy penetration depths into the top mirror and the bottom mirror, respectively. In case of low damping condition, the 3 dB bandwidth is related to the relaxation resonance frequency ($f_R = \omega_R/2\pi$) as

$$f_{3dB} \approx 1.55 f_R. \tag{2.70}$$

Therefore, it is essential to squeeze the vertical confinement, thereby enhancing the modulation bandwidth. Recently, to reduce the mode volume of a long-wavelength VCSEL, a top dielectric DBR and a bottom metal-assisted DBR have been employed and the short-cavity VCSEL achieved 3 dB bandwidth of 17 GHz at room temperature [39].

2.3.5 Mirrors for long-wavelength VCSELs.

After the first suggestion of a vertical-cavity surface-emitting laser (VCSELs) in 1977 [21], the first VCSEL had been demonstrated in 1979 using GaInAsP/InP material system for the active region which emit 1.3μm wavelength [74]. The first CW operation at room temperature (RT) was demonstrated using GaAs material system in 1988 [75]. Then, GaAs-based VCSELs have been intensively studied and short-wavelength VCSELs ($\lambda \sim 800-1{,}000$ nm) have been commercialized. The VCSELs have a lot of advantages compared to the edge-emitting lasers. One of the most attractive feature is that VCSELs consume low energy because of their small cavity volume [20]. The other one is a number of VCSELs can be fabricated by fully monolithic processes which result in very low production cost [74]. In addition, VCSELs can support high-speed data transmission because VCSEL structure can support large relaxation oscillation frequency [20]. These are some distinct features of VCSELs, and there are a lot of excellent features not mentioned here.

For the VCSEL applications, the top and bottom mirror need to have a high reflectance due to the short length of an active layer [20]. As shown in Fig. 2.12, there

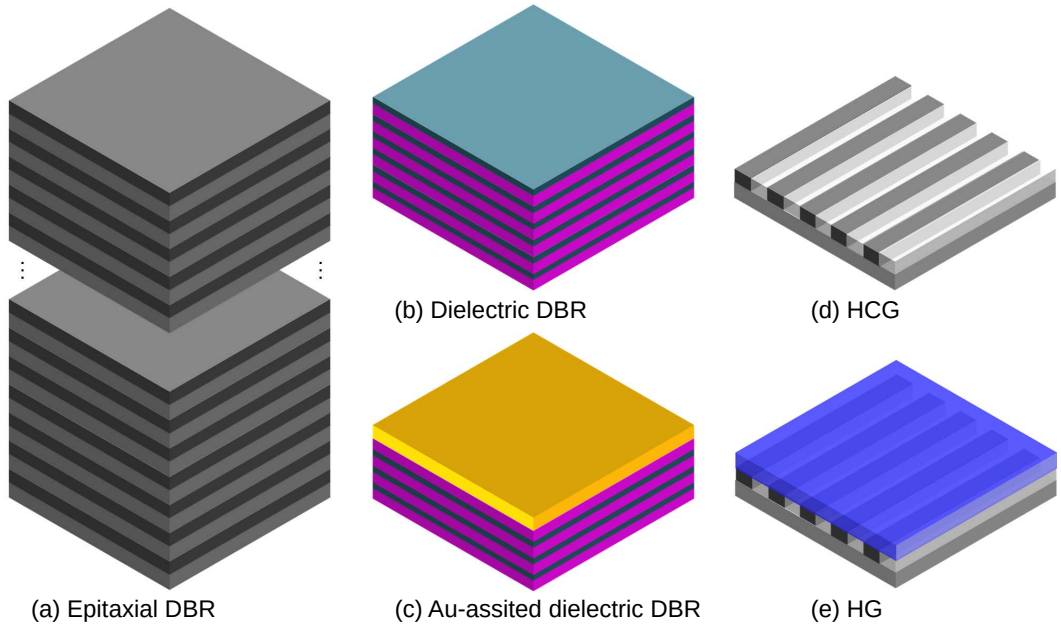

Figure 2.12: Schematic illustrations of mirrors for VCSEL applications. (a) An epitaxial DBR grown with lattice matched material or bonded with fusion bonding process. (b) A dielectric DBR deposited with dielectric materials. (c) An Au-assisted dielectric DBR. (d) A HCG reflector surrounded by low refractive index material. (e) A HG reflector capped with a finite-thick high refractive index material.

are numerous types of mirrors which have been employed for VCSELs. Recently, long-wavelength VCSELs (1.3 or 1.55 μm) have been getting a lot of attention because the long-wavelength VCSELs are compatible with silicon photonics platforms due to their transparency in silicon [30]. Especially, the long-wavelength VCSELs consume less power compared to the short-wavelength VCSELs and have one-tenth of the energy consumption of edge-emitting lasers [30]. The diverse kinds of mirrors, which have been used for the long-wavelength VCSELs, are are summarized in Table. 2.1.

Table 2.1: Material combination of DBR mirrors for long-wavelength VCSELs.

λ (nm)	All-semiconductor Mirror	Dielectric Mirror	Metal-assisted Dielectric Mirror
1300, 1550	GaAs/AlGaAs [43] In(GaAs)P/InP [31] GaAsSb/AlAsSb [46] AlGaInAs/AlInAs [48]	a-Si/SiO_2 [44, 47] SiO_2/TiO_2 [49] CaF_2/a-Si [39] CaF_2/ZnS [39]	(SiO_2/TiO_2)/Au [49] (CaF_2/a-Si)/Au [39]

For short-wavelength VCSELs, epitaxially grown all-semiconductor DBRs have been used successfully based on an AlGaAs/GaAs pair [54]. The AlGaAs/GaAs DBRs possess good thermal conductivity and reasonable Δn [32]. For the long-wavelength VCSELs based on InP system, epitaxially grown InGaAsP/InP DBRs have been applied as well. However, the InGaAsP/InP DBRs have two significant drawbacks. First, the Δn for the InGaAsP/InP DBRs is approximately 0.25 which is half of that of AlGaAs/GaAs DBRs, and it means that the DBRs for the long-wavelength VCSELs need more number of DBR pairs. The number of DBR pair should be more than 40 to meet the lasing condition. Since the DBRs are designed with the quarter-wave thickness, the total thickness of DBR become thicker compared to that of short-wavelength VCSELs. In addition, due to the low Δn, the penetration depth into the DBR is lengthy; and therefore, the long penetration depth deteriorates the ω_R. Second, the lattice-matched InGaAsP/InP materials have relatively poor thermal conductivity compared to AlGaAs/GaAs materials [32]. Then, the DBR with a low thermal conductivity and a bulky structure can hinder the CW operation. Therefore, for the long-wavelength material system, it needs to avoid the low Δn epitaxial DBR.

There have been intense effort to solve the issues related to the long-wavelength mirrors. As an alternative, the AlGaAs/GaAs DBRs are employed using a wafer-fusion process because the AlGaAs/GaAs DBRs are not lattice-matched with the InP system [42]. The use of wafer fusion for long-wavelength VCSELs has been successfully demonstrated. However, it is not easy to combine the top and bottom DBRs using the wafer fusion process. The other way is to grow AlGaAs/GaAs DBRs on InP substrate using metamorphic growth [45], which is not constrained to the lattice-matching condition. However, it still needs 23.5 pairs to reach 99.5% with additional buffer layer to prevent dislocations. The epitaxial DBRs used for long-wavelength VCSELs are summarized in Table 2.2.

Another way is to use dielectric materials for DBRs using deposition or sputtering processes. In Table 2.3, the dielectric materials are summarized. The Δn of dielectric DBRs is higher than that of semiconductor DBRs because there is no need to consider

Table 2.2: Epitaxial DBR mirrors employed for long-wavelength VCSELs.

λ (nm)	Materials	Pair	Δn	Substrate	Method
1540	GaAs/AlGaAs (p-type)	30	0.33	InP	Wafer Fusion [42, 43]
1540	AlAs/GaAs (n-type)	28	0.49	InP	Wafer Fusion [42, 43]
1550	GaAs/AlGaAs (p-type)	23.5	-	InP	Metamorphic Growth [45]
1550	InGaAsP/InP (n-type)	45	0.2	InP	Epitaxial Growth [31]

the lattice-matching condition, which allows to select material combination with higher Δn. Therefore, the number of pairs of the dielectric DBR can be less than 10. Besides, with the help of noble metals such as Au, the number of pair of the dielectric DBR can be reduced further because the metal performs additional high reflective mirror [39]. If the noble metal is deposited on the dielectric DBRs, then it can additionally work as a heat sink to remove the heat generated in the active layer [39]. Since the dielectric DBR materials have a lower thermal conductivity compared to the semiconductor materials, the Au-assisted DBR is essential to operate the laser at room temperature [39]. From Table 2.2 and 2.3, it is evident that dielectric DBRs need less pair of DBRs to reach the desirable reflectivity because of larger Δn.

Last, a novel approach to replace the epitaxial DBRs has been suggested and demonstrated by using a top HCG reflector [27]. This first demonstration has been paved the way to solve the problem of the long-wavelength VCSELs. The HCG mirror is very thin ($<$ 500 nm) and single-layer structure, and possess broad stopband of $\Delta\lambda/\lambda > 30\%$ with reflectivity of 0.99 [50]. Using CMOS-compatible process, the top and bottom DBR has been replaced with HCG mirrors [68]. In addition, using a direct wafer-bonding process, a vertical cavity laser with a bottom

Table 2.3: Dielectric DBR mirrors for long-wavelength VCSELs.

λ (nm)	Materials	Pair	Δn	Method
1540	SiO_2/a-Si	5	2.16	Deposition [44]
1520	SiO_2/TiO_2	3.5	-	Deposition (Ti/Au-assited) [49]
1550	CaF_2/ZnS	5	0.95	Deposition [39]
1550	CaF_2/a-Si	3	2.2	Deposition (Au-assited) [39]

HCG and top dielectric DBR has been demonstrated [40]. Also, a new type 'HG' reflector has been suggested and experimentally demonstrated. The HG reflector consists of a high index membrane and a bottom grating structure. The membrane can possess an active layer. The HG reflector can be employed as a bottom mirror for a hybrid vertical cavity laser [55] as well. Therefore, for the long-wavelength VCSEL applications, the HCG or HG mirrors have promising potential because it is free from the lattice-matching condition, broadband stopband, and very thin mirrors compared to all kinds of DBR mirrors.

2.4 Unique Feature of Grating Mirror

For long-wavelength VCSELs, HCG or HG reflector can be an alternative of one of the epitaxial DBR or both of them of the vertical cavity structures by reducing the physical volume [68]. Not only highly broadband reflectance with a thin layer, there is another distinct feature compared to DBR mirrors. One is the polarization dependent reflectance [27] and the other one is the in-plane guided modes [25], which are excited relative to the vertical direction and then guide some portion of incident light along the in-plane guiding structure. Even though it is not distinct feature, it should be emphasized that the grating reflector can be transferred on a top Si layer of silicon photonics platform [25]. Therefore, by using a direct wafer bonding (DWB) process [76] and via the property of the in-plane guided modes, it is possible to realized an Si-integrated hybrid vertical cavity laser (VCL) which emits light into the in-plane direction [25]. Therefore, there is no need to use bulky or complex integration scheme. In addition, by using the wafer-bonding process to integrate the active layer on a silicon platform, it is feasible to enhance the density of integration of the light source because the light sources can be fabricated by using all CMOS-compatible processes. All these advantageous result from the use of Si grating reflector in the silicon platform.

Before investigating the unique optical properties in detail, the reflectance spectra of the representative HCG and HG reflector are shown in Fig. 2.13. The HCG reflector consists of a single grating layer with a thickness of < 500 nm [73]

and the HG reflector are collectively comprised of a grating layer and a membrane with a total thickness of < 1 μm [55]. With such thin layers, those reflectors show high reflectance in a broad wavelength range. For the HG reflector, the membrane can possess active layer with a proper space layers for a VCL. Then, the membrane directly contacted with the bottom Si layer can contribute to efficient heat dissipation, which is generated on the active layer, transferring thermal energy into the large bottom Si layer. Moreover, the bandwidth is even larger than that of the HCG. The more detail about the HG reflector will be discussed in Chapter 5. The two properties of the HCG or HGR, i.e., thin and high reflective mirror are the fundamental necessity of the reflector for long-wavelength VCSEL applications.

The fractional bandwidth (FB) is used to characterize the DBR mirror. The FB is calculated as [52]

$$\mathrm{FB} = \frac{\Delta\omega}{\omega_0} \approx \frac{4}{\pi} \arcsin\left(\frac{\mathrm{n_H} - \mathrm{n_L}}{\mathrm{n_H} + \mathrm{n_L}}\right). \tag{2.71}$$

The approximation is applied when the Δn is small. In case of a dielectric DBR with 5 pair SiO_2/a-Si ($\mathrm{n_{SiO_2}} = 1.45$ / $\mathrm{n_{a-Si}} = 2.92$), due to the large Δn, the calculated fractional bandwidth of 99% is as wide as ~36%. The larger Δn, the wider bandwidth. The HCG with a thickness of 492 nm, which is shown in Fig.

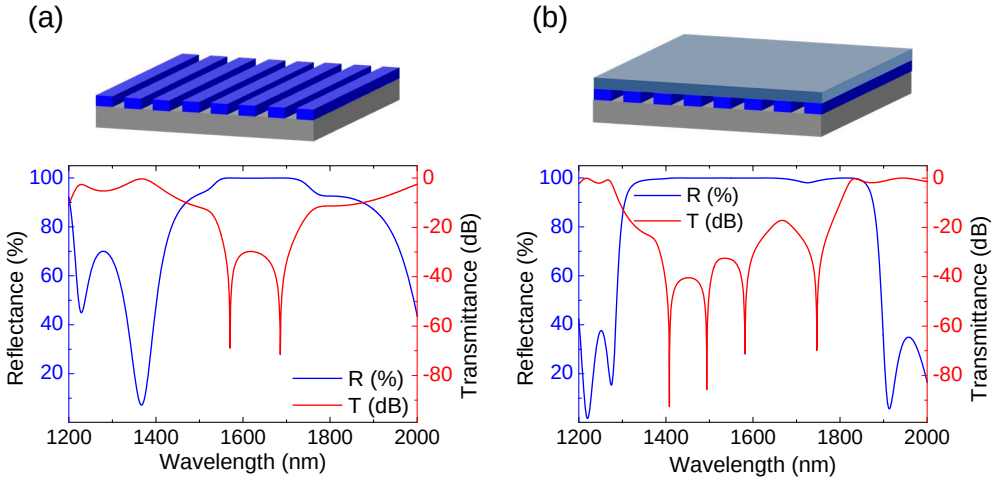

Figure 2.13: Schematic illustrations of (a) HCG and (b) HG reflectors and corresponding reflectance and transmittance spectra, respectively.

Table 2.4: FB and BOT for dielectric DBR, epitaxial DBR, and TM HCG.

Type	λ (nm)	Materials	Pair	Δn	d (μm)	FB (%)	BOT (%)
Dielectric DBR [44]	1550	SiO_2/ a-Si	5	2.16	~2.0	36.4	28.2
Epitaxial DBR [43]	1540	AlGaAs/ GaAs	30	0.33	~7.2	3.3	0.7
HCG	1550	air/c-Si	1	2.48	~0.5	11.8	37.4

2.13(a), possesses a FB of ~12%. For the comparison purpose, the wafer-fused p-type AlGaAs/GaAs DBR for 1540 nm VCSEL is calculated, and the FB of 97% is ~3.3%.

A new figure of merit (FOM) can be defined considering the thickness of mirrors and a bandwidth over thickness (BOT) can be defined as

$$\mathrm{BOT} = \frac{\Delta\omega}{\mathrm{d}}, \tag{2.72}$$

where 'd' is the thickness of the mirror. The FB and BOT for the three mirrors are listed in Table 2.4. When using BOT to characterize the three mirrors, the HCG is the superior mirror due to the single-layered mirror with less than a half micron. The epitaxial DBR is the poorest one due to more than 7 μm-thick DBR. The two FOMs for the HG reflector will be discussed in the later chapter.

In addition, the experimental feasibility of the grating mirrors is estimated in terms of reflectivity variation as the grating parameters vary. For the HCG and HG reflector, the dry etching process is used to introduce the grating patterns. The possible deviation will be caused during the e-beam or photo-lithography process to form a hard mask for the dry etching. This mask pattern will be transferred on the sample with deviation from the design parameters. In addition, the transferred grating thickness can be differ from point to point on a wafer because of the possible non-uniformity of the wafer. To estimate the effect of deviation on the reflectivity of HCG reflectors, a Monte Calro simulation is conducted by generating 10,000 random parameter combinations. The two parameters of width of Si grating bar (s) and grating thickness (t_g) are randomly generated following the probability

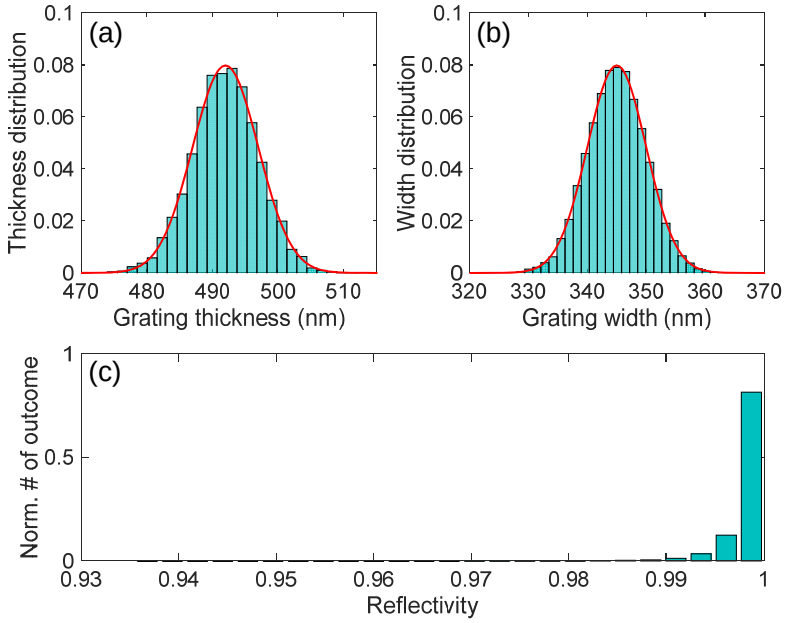

Figure 2.14: Numerical estimation of design tolerance of HCG reflector in terms of reflectivity. Probability distribution of (a) grating thickness ('t_g') and (b) grating width (s). The red lines are the probability density function for a normal distribution with each mean ('μ') and standard deviation ('σ'). (c) Normalized reflectivity distribution of the HCG reflectors.

density function (pdf) for a normal distribution as

$$f(\mathrm{x}, \mu, \sigma) = \frac{1}{\sigma\sqrt{2\pi}} \exp\left[-\frac{(\mathrm{x}-\mu)^2}{2\sigma^2} \right], \tag{2.73}$$

where 'x' is the range for the corresponding parameters, μ is the mean value of the distribution, and σ is the standard deviation. The histograms showing the normal distribution for each parameter and the corresponding pdf with a red line are shown in Figs. 2.14(a, b). The TM HCG design parameters (μ) and the corresponding $\sigma$are given in Table 2.5. It is assumed that the period (Λ) is equal to the design value. The three standard deviation 'σ' ($\pm 3\sigma$) for the 't_g' and 's'

Table 2.5: Design parameters and deviations of the TM HCG.

	period (Λ) (nm)	grating thickness (t_g) (nm)	width (s) (nm)
μ	720	492	345
σ	-	5	5

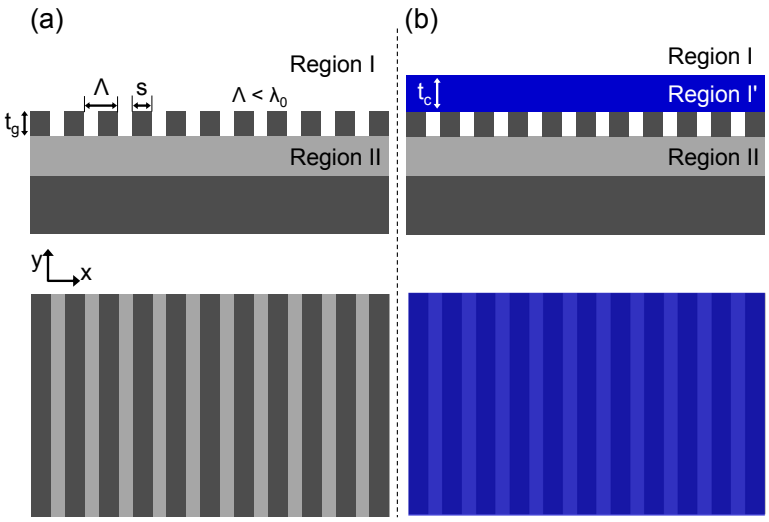

Figure 2.15: Schematic illustrations of the cross-sectional (the first row) and top view (the second row) of (a) HCG and (b) HGR reflectors.

from each design value are ±15 nm, and this deviation is not underestimated. As shown in Fig. 2.14(c), among the 10,000 samples, more than 9,800 samples are of the reflectivity of > 0.99. It shows that most of the HCG reflectors can bu used for the VCSEL application under rather severe deviation.

2.4.1 Polarization sensitivity

The distinct feature of patterned HCG mirrors compared to unpatterned DBR mirrors are the polarization sensitivity [27]. As shown in Fig. 2.15, the HCG and HG reflector possess a single layer of grating structures periodically extended along x-y plane. Therefore, the main difference between HCG or HG reflector and DBRs are the direction of the primitive reciprocal lattice vector. In case of the DBRs, the direction of the reciprocal lattice vector is the same as the propagation direction (z-direction) of the incident light. For the HCG and HGR reflectors, there are periodic grating structure extended along one of the transverse directions (x- or y-direction). As a result, the optical property of the HCG and HG reflectors depend on the polarization of the incident light, which propagates along the z-direction. If a HCG reflector is designed for the TM-polarized light, i.e., the incident H-field is parallel to the direction of the grating bar, then only TM light will be strongly reflected

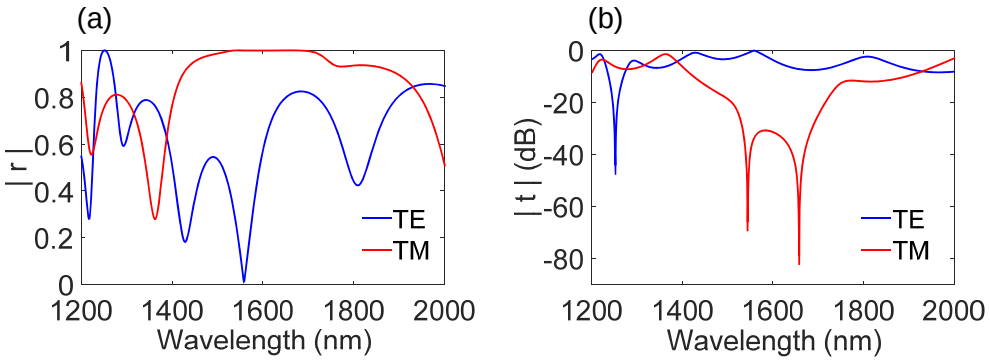

Figure 2.16: Calculated (a) reflectivity in linear scale and (b) transmissivity in dB scale of a TM HCG as a function of wavelength for TM- and TE-polarized normal incident plane wave.

from the HCG at specific wavelength range. As shown in Fig. 2.16 in linear and dB scale, respectively, it is manifest that the TM HCG reflector, which is designed for 1550 nm wavelength, shows high reflectivity of 0.9999 for the TM-polarized light. However, for the TE-polarized light, it shows low reflectivity of 0.1314. The difference of the reflectivity ($\Delta|r|$) at 1550 nm is 0.8685. If the highly reflective HCG or HG reflector is designed for one of polarizations, then the lasing condition of VCSEL is only met at the designed polarization mode [27]. Therefore, it is possible to suppress the other polarization modes with high suppression ratio of 20 dB [27] and prevent the instability of lasing frequency caused by the polarization-mode hopping [77]. In case of the DBR, if the optical property of DBR materials are independent of the transverse direction, then the reflectivity of the TE and TM mode is the same. Therefore, such DBRs employed for VCSELs can excite TE and TM modes and can suffer from polarization-mode hopping [77].

2.4.2 Vertical to in-plane routing property

Since the reflection process of HCGs is involved with in-plane guided mode resonance [72], the HCG can guide some portion of a vertically incident light into the in-plane direction. As an illustration, a finite HCG structure is shown in Fig. 2.17. Around the HCG region, there are unpatterned waveguide region. The vertically-incident Gaussian beam mostly reflect back to region I with $\sim$0 dB because it is designed as a high reflective mirror. At the left- and right-boundary of the HCG and the waveguide

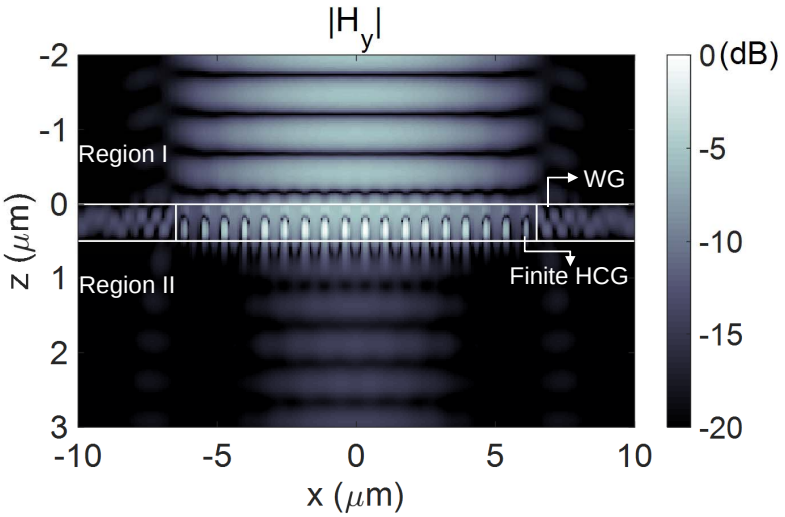

Figure 2.17: $|H_y|$ filed profile of a finite TM HCG (18*Λ) at 1550 nm in wavelength under the incidence of Gaussian beam with a width of 9 μm. In the waveguide region of the unpatterned Si layer bordered to the finite HCG, waveguide modes are excited by the Bloch eigenmodes of the HCG. [WG: waveguide]

regions, in-plane guided modes in the unpatterned waveguide regions are excited by the Bloch eigenmodes of the HCG. Then, small amount of light propagate along the waveguide as shown in Fig. 2.17. Therefore, the HCG can work as highly reflective mirror along the vertical direction (z-direction) and route part of the incident light into the in-plane direction (x-direction) as well. For the numerical simulation of the finite-sized TM HCG, the average parameters in Table 2.5 is used and the absorbing boundary is introduced on the left and right boundaries, respectively [78].

2.5 Summary

To sum up, the new functionality of HCG and HG mirrors have been introduced. The progress of the mirrors for the conventional long-wavelength VCSELs has been introduced as well. The novel HCG and HG mirror can be strong alternatives for VCSELs application due to their highly broadband stopband with a thin layer. Moreover, the unique property of in-plane guiding property of the HCG or HG reflector can be employed for vertical cavity laser (VCL) with in-plane emission.

To investigate the optical property of the patterned and unpatterned mirrors, RCWA method has been explained. Using RCWA method, DBR, HCG

and HG mirrors can be analyzed in terms of phase penetration depth, energy penetration depths, and polarization-dependent reflectance, which influence on the laser characteristics such as lasing frequency, intrinsic resonance frequency and polarization-mode hopping.

You can observe a lot just by watching.

— Yogi Berra

3 Device Fabrication

Contents

In this chapter, it is explained in detail how the overall fabrication processes are designed and developed for realizing long-wavelength hybrid vertical cavity lasers (VCLs) on a silicon-on-insulator (SOI) platform. The hybrid VCL consists of 1) a top dielectric DBR, 2) a III-V active layer, 3) an air gap, and 4) a bottom grating mirror on the top silicon (Si) layer of a SOI. Also, a Si waveguide is put near the one boundary of the grating region, which enables the vertically-resonant

light to emit the output into the in-plane Si waveguide.

The main part of this thesis work is the experimental demonstration and the validation of the concept of hybrid VCLs using the novel bottom grating mirror on the SOI platform. Among the multistage fabrication procedures, one of the primary process steps is the direct wafer bonding (DWB) process, which enable the III-V gain layer to be integrated with the SOI platform. Using the DWB process, the hybrid or heterogeneously-integrated structure is realized. The other one is a lift-off process to form a dielectric distributed Bragg reflector (DBR) as a top mirror of the hybrid vertical cavity laser structure. The dielectric DBR possesses a high index contrast between the high-index material and the low-index one, which allows it to have a fewer pair when compared to a conventional epitaxial DBR. Therefore, it can be a compact DBR. These two primary processes are CMOS-compatible processes and the others as well.

First, an overview of exemplary wafer bonding processes is introduced, and then the DWB process is explained in Section 3.3, which includes two surface treatment processes. The key processes and their corresponding explanations for the DWB can be found in [76, 79] in detail. For the hybrid vertical-cavity laser structure, a precise control of the vertical-cavity length is necessary. Otherwise, the lasing wavelength will be shifted away from the target wavelength. Therefore, the thickness control of the vertical cavity is the critical factor to be considered. In this thesis work, the DWB is conducted without any intermediate layer such as SiO_2 [76]. The control of the vertical cavity length solely depends on the thickness of the III-V epitaxy grown using a metal organic chemical vapor deposition (MOCVD), which guarantee the high accuracy of thickness control.

Second, a lift-off process and an etch-back process are compared and explained schematically in Section 3.5. The lift-off is a standard process for the metallization, but it is not for the DBR formation. Since the principle of the lift-off process is the same as the one for the metallization, a proper thickness of a photoresist (PR), which works as a mask to form the DBR, should be chosen considering the thickness of the DBR. The thickness of a dielectric DBR is in the range of 2.5 to 3.5

μm; and therefore, the PR mask should be thicker than the DBR. Otherwise, the DBR layer will block the sidewall and the undercut, which finally make the lift-off process impossible. As well as the thickness condition of the PR mask, its thermal stability needs to be considered because the DBR sources with a heat energy is evaporated and deposited on the surface of the PR. Then, if the PR has a low thermal resistance, then it become solidify, which hinder the lift-off process. Last, an undercut should be wider and thick enough to remove the PR efficiently. The other process to form a DBR, an etch-back process is used. The etch-back process is developed to make the DBR more flat over the entire area. Besides, the area of the DBR can be smaller than the DBR formed by the lift-off process because the DBR using the lift-off process suffers from the round-down problem around the boundary. The round-down boundary reduces the effective region of the DBR, which work as a high-reflective mirror. Because of these reasons, there is a size limit of the DBR which can be formed by the lift-off process. For the etch-back process, a thick enough PR is utilized as a mask considering the selectivity to the PR and the DBR.

Furthermore, to introduce the air gap above the bottom grating and below the III-V active layer using a wet etch process, the sacrificial layer etching is carried out using the connected two channels: 1) two via holes and 2) the air part of the bottom grating. Since the position of the via holes about both the DBR and the bottom grating can influence the etch rate of the sacrificial etching process, it is important to design it carefully.

3.1 III-V Epitaxy and SOI Structure

For light sources in silicon photonic integrated circuits (PICs), the 1310 or 1550 nm long-wavelength light is preferred because it shows the small absorption loss in Si [17, 80]. Therefore, it is possible to transmit optical signal longer distance compared to the shorter wavelength, which suffer from the optical loss. Of the two popular wavelengths, the longer wavelength is chosen because the quasi-Fermi level related to a voltage, $V \approx \hbar\omega/q$ (where $\hbar$ is the reduced Planck constant, ω is the angular frequency, and q is the elementary charge), is lower than the shorter

Table 3.1: III-V epitaxial structure.

Layer #	Period	Material	Thickness (nm)	Function	Comment
9	1	InGaAs	20	Cap layer	-
8	1	InP	20	-	-
7	1	InGaAs	240.3	Sacrificial layer	-
6	1	InP	191.7	Bottom cladding layer	-
5	7	InGaAlAs	7.5	Barrier layer	-
4	7	InGaAlAs	6.5	Well layer	7 QWs
3	1	InGaAlAs	7.5	Barrier layer	-
2	1	InP	191.7	Top cladding layer	-
1	1	InGaAs	250	Etch stop layer	-
0	1	InP	350 (μm)	Substrate	-

one [81]. Therefore, the threshold power to operate the laser can be further reduced. In this thesis work, to prove the concept of the Si-integrated hybrid vertical cavity laser (VCL), a III-V epitaxy as a gain material is designed. The epitaxy structure and the function of each layer are shown in Table 3.1. The optical property of the quantum wells (QWs) was confirmed by mapping photoluminescence (PL) as shown in Appendix A and the peak gain was at 1541 nm considering the gain-cavity detuning due to thermal effect. The layer structure of a SOI wafer is shown in Table 3.2. On the top crystalline silicon (c-Si), a bottom grating and a waveguide will be transferred. The buried oxide (BOX) layer is the low index material of SiO_2. Therefore, an optical mode can be confined inside the top c-Si waveguide when a low index material is introduced above it as well.

The representative hybrid laser structure using the III-V epitaxy as a gain

Table 3.2: SOI structure.

Layer	Material	Thickness (μm)	Function
2	c-Si	0.5	Top silicon layer
1	SiO_2	3.0	BOX layer
0	c-Si	-	Substrate

Table 3.3: Device structure of hybrid vertical cavity lasers.

Layer	Material	Period	Function
7	a-Si / TiO_2	6 / 7	High index layer for DBR (top mirror)
	SiO_2 / SiO_2	6 / 7	Low index layer for DBR (top mirror)
6	InP	1	Cladding
5	InGaAlAs / InGaAlAs	7	7 QWs
4	InP	1	Cladding
3	Air	1	Low index layer for HCG
2	c-Si	1	HCG (bottom mirror)
1	SiO_2	1	Low index layer for HCG
0	c-Si	1	Substrate

material (Layer: $4 \sim 6$) and the SOI platform (Layer: $0 \sim 2$) is shown in Table 3.3. In case of the DBR (Layer: 7), two different material combinations for the high and low index pairs are used.

3.2 Preparation of III-V and SOI Chips

3.2.1 Sample cleaving

For a chip-scale process, a 2-inch III-V wafer and a 5-inch SOI wafer, which are covered with a PR, are cleaved into square chips with 0.7 cm $\times$ 0.7 cm and 1.5 cm $\times$ 1.5 cm, respectively. The PR protect the surface from possible scratches during cleaving the wafers. The III-V chip size is determined by considering the two factors. One is the overall size of the bottom patterns which is transferred to the SOI chip, and the other one is a substrate removal process. The bottom Si patterns are mainly comprised of 1) the gratings and waveguide patterns and 2) the photolithography alignment marks. The III-V chip should thoroughly cover the gratings and the waveguides. However, the III-V chip should not cover the alignment marks for the following photolithography processes. The other consideration is a wet etching process to remove a thick InP substrate of the III-V chip right after a direct wafer bonding process. During the wet etching process, the etchant can etch the other InP layer among the whole epitaxial layers (Layer: 2, 6, and 8 in

Table 3.1) from the boundary as well. It was observed that the four boundaries with a width of ∼500 μm was finally etched and broken away from the center of the III-V membrane. Therefore, when determining the size of the III-V chip, the bottom pattern size and the wet etching process should be carefully considered. If the size is too large, the alignment mark will be blocked by the III-V chip. If too small, then the grating and waveguide pattern cannot be entirely covered with the active material. Importantly, during the wet etching process, the exposed large patterns on the SOI such as the waveguide patterns can guide the wet etchant, and it can destroy the bonding interface of the two chips and finally detach them. Therefore, it should not be overlooked how to decide the size of the III-V chip. The other consideration is that, during the sample cleaving process using a tungsten tip, the bonding surface should not be directly scratched using the tip. Instead, the backside of the wafers is scratched and then it is cleaved to prevent it from creating the micro-sized fragments along the cleaved edges of the surface.

3.2.2 Bottom HCG patterning

The SOI chip is cleaned with a solvent cleaning process to remove the PR on top of the SOI chip. Then, a diluted e-beam resist, ZEP520A (5.5%, ZEON Chemicals) is spun on the SOI. Before the spin coating, the SOI surface should be cleaned with N_2 gas to blow small particles off from the surface. Because if there are small particles near the center of the SOI, the particles can finally block the area where the grating or the waveguide pattern should be transferred. Next, the SOI chips are loaded and then the patterns are transferred. After the electron beam lithography process, the patterns are developed using a ZED-N50 developer (ZEON Chemicals) and then a post-bake process is carried out to harden the ZEP520A, which work as a hard mask. To transfer the pattern on the Si layer, an advanced silicon etcher (ASE) is used using an 11-cycle Bosch process, which allow the grating to have a deep anisotropic profile, i.e., vertical grating and waveguide patterns. Finally, the ZEP is stripped with Microposit Remover 1165 (DOW Electronic Materials). The transferred pattern on the SOI is shown in Fig. 3.1. The straight lines in the HCG (1D grating) and

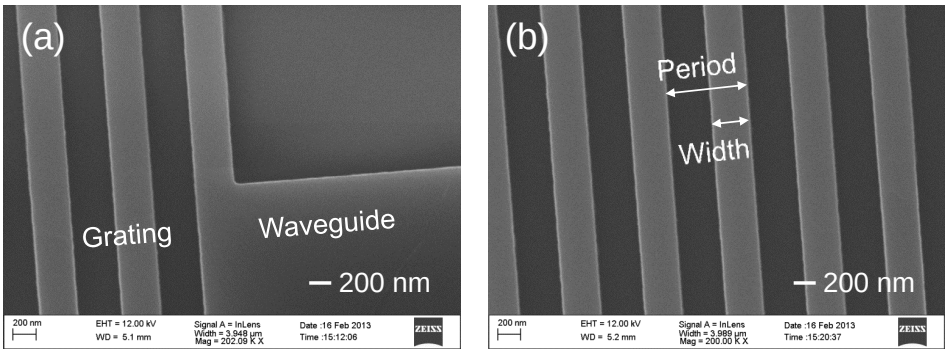

Figure 3.1: Scanning electron microscope (SEM) images of the transferred pattern on the top c-Si layer of the SOI. (a) The bottom HCG pattern and the waveguide put next to the one end of the grating boundary. (b) Two design parameters of the HCG, a period (Λ) and a width of the Si bar (s), are shown.

the waveguide are well defined as shown in Fig. 3.1(a). For the HCG pattern, it is necessary to confirm two parameters, i.e., a period (Λ) and a Si bar width (s) as shown in Fig. 3.1(b). Since the two parameters will determine a lasing wavelength, it should be validated that the design and experimental parameters are matched within a tolerance. Considering the possible experimental deviation during the e-beam exposure and the dry etching process, the four groups are designed and then those patterns are transferred on the SOI as shown in Fig. 3.2.

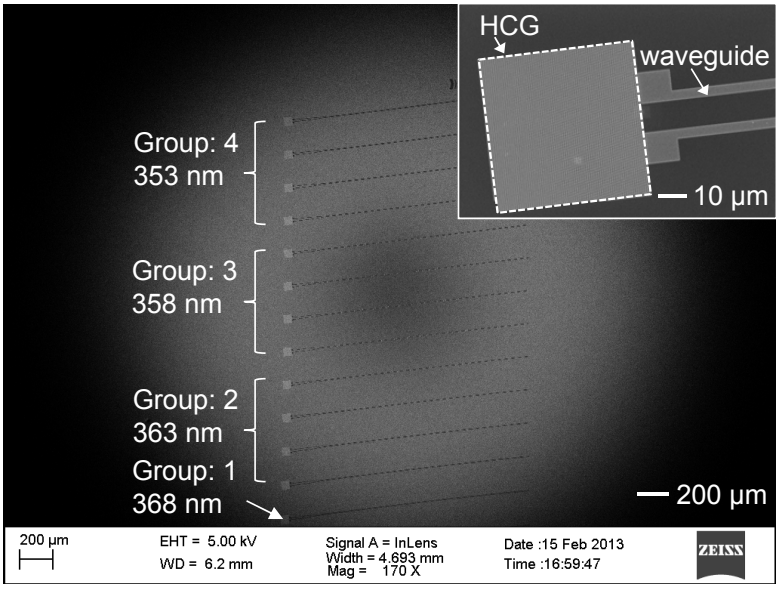

Figure 3.2: SEM image of four different HCG groups. Each group has a different width. The inset shows the zoom-in image of one of the grating patterns.

3.3 Direct Wafer Bonding

3.3.1 Overview

In the electronic industry, Si has been the central material as a bulk platform of being used for complementary metal-oxide-semiconductor (CMOS) integrated circuits [4]. Nowadays, SOI platform has become popular instead of the bulk Si substrate because the SOI employs an insulator (BOX) layer below the top Si which can effectively reduce the parasitic capacitance and, therefore, can reduce operating voltage and enhance operating speed [82, 83]. Based on the matured bulk CMOS technology, the SOI CMOS technology has been developed and successfully met the demands of being low-power consumption and high-speed operation [82, 83].

The CMOS integrated circuit technology is not limited to the electronic realm, but now it extends to the optical area. The ultimate goal is to integrate the electrical devices and the optical devices on the same silicon chip [4, 84]. Because the electronic circuits reach the limit of reducing the energy consumption further, the idea to solve this issue has been suggested and investigated by using a light signal, which can potentially reduce power consumption and enhance the signal speed. The SOI platform is attractive not only for electronics but also for photonics because the BOX layer has a low refractive index ($n_{BOX} = 1.45$). If the Si layer is surrounded by a low-index material like air or SiO_2, an optical mode can be well confined in the Si layer, which function as a waveguide. Until now, based on the SOI platform, there have been a lot of effort to build optical circuits including active and passive devices. Based on these efforts, it becomes feasible to integrate the electrical and optical circuits on the SOI platform altogether [4, 84, 85].

Of the passive and active optical devices, one of the most challenging devices to implement on a SOI platform is a light source because Si itself cannot be an efficient light-emitting material [9, 16]. Since it is an indirect band gap material, it cannot be an effective light source like III-V compounds which has a direct band gap [8, 9]. Even though there have been remarkable results such as a continuous-wave (CW) Raman laser and a periodic nanopatterned Si laser demonstrated

by using an optical pumping scheme [10, 11], the output power is still low, and the efficiency is quite small.

As an alternative to the Si gain material, there have been intense efforts to grow germanium (Ge) on a SOI platform [12, 13]. Since Ge and Si have ∼4% lattice mismatch, a thick buffer layer with ∼1 μm is needed to overcome the rough surface and threading dislocations. Besides, Ge is an indirect band gap material. A high n-doped Ge layer with a strain used to tailor the indirect band gap, and then it modified the indirect band gap to a direct band gap Ge [12]. Recently, a direct band gap GeSn has been grown without introducing additional strain [13]. Even though such kinds of Ge-based light sources can be a breakthrough to implement a real monolithically-integrated light source on the SOI, considering the efficiency, it is still far to be applicable for the moment.

The other way to integrate the light source on the SOI platform is a flip-chip bonding [86]. It combines a laser diode die on the SOI platform. First, the laser is fabricated using a III-V epitaxy and then it is cut into a single device. On the laser die and the bottom SOI, metal pads are formed. On top of the pad, solder metals are formed. Then, the laser die and the SOI platform are aligned and bonded using the solders as an adhesive material. This flip-chip bonding process requires an accurate alignment in position because it is necessary to align the top and bottom position of the bumps precisely. Also, using the flip-chip bonding process, it is tricky to integrate the light source densely on the SOI platform [9].

Another way is to grow a direct band gap material on a Si platform: a hetero-epitxy growth [87]. For a 1.55 μm light source, the InP material system is necessary. Since the lattice mismatch between the InP and the Si is ∼8%, it causes the huge density of threading dislocation. The dislocations degrade the optical property of the III-V epitaxy grown on the Si substrate when compared to the III-V epitaxy grown on its own material system. Likewise, for 1.3 μm light source, GaAs material system is used which has a lattice mismatch of ∼4% between the GaAs and the Si. Comparing to the InP system, it has 50% better condition in terms of the mismatch; however, it still needs thick buffer layer to grow high-quality active layer.

Last, it is the wafer bonding process [76, 79]. The III-V active material is grown on its lattice-matched substrate. Therefore, it possesses high-quality optical properties. Then, the III-V active layer is bonded on a SOI platform with or without an adhesive material. The following processes for fabricating the laser device can be done using the CMOS-compatible processes after completing the direct wafer bonding and then removing the substrate. The CMOS-compatible processes can increase the integration density of the III-V active layer on the SOI. Using the oxygen (O_2)plasma-assisted DWB, the electrically-pumped in-plane laser was demonstrated, for the first time. It showed a maximum output power of 1.8 mW and operated up to 40°C [15].

As an illustration, the DWB process for Si-Si is exemplary [76, 88]. The involved DWB process is described in Eqs. (3.1 - 3.3). The left of Eq. (3.1) describes the two surfaces after a hydrophilic surface treatment which is terminated with hydroxyl groups (OH-). The two surfaces are mated via Van der Waals force. After applying high temperature, a sable bonding interface is formed through Si-O-Si described on the right of Eq. (3.1) by generating by-product (H_2O). The by-product H_2O will diffuse out through the interface and react with Si then according to Eq. (3.2). Another by-product gas, H_2 is generated as shown in Eq. (3.2).

$$\mathrm{Si-OH + Si-OH \rightarrow Si-O-Si + H_2O}, \tag{3.1}$$

$$\mathrm{Si + 2H_2O \rightarrow SiO_2 + 2H_2\,(g)}. \tag{3.2}$$

This DWB for the Si-Si can be done at low-temperature (<350°C) due to the hydrophilic surface treatment [79]. For the commercial SOI, the DWB is conducted at high temperature (>800°C) because the generated by-product gases such as H_2 and H_2O can be readily diffuse out from the bonding interface or be absorbed into the porous BOX layer at such high-temperature condition [76]. Therefore, the high-temperature direct wafer bonding results in a strong and a void-free bonding interface.

For the DWB between a III-V chip and a SOI, hydroxyl groups are formed on the surface of the III-V chip by combining metal component, M, in the form

of M-OH [76]. Therefore, the polymerization process in Eq. (3.1) is replaced with the following equation.

$$\mathrm{Si-OH+M-OH \rightarrow Si-O-M+H_2O.} \tag{3.3}$$

For a vertical-cavity laser, a DWB without any adhesive material is chosen because a small change in the laser cavity length can significantly influence the lasing wavelength. There are four important considerations to implement the DWB without any adhesive layer between a III-V active layer and a SOI platform. First, the DWB should be conducted at a low temperature (<400°C). The thermal expansion mismatch between the III-V layer and the Si will cause debonding of the mated sample while cooling down to room temperature (RT) because of the stress. Furthermore, the high-temperature condition can cause decomposition of the III-V compound semiconductors which will degrade the material quality [16, 76]. Therefore, the DWB is conducted at 300°C.

Second, a flat surface is necessary to initiate a manual bonding using Van der Waals force. The flat surface indicates, 1) the surface flatness of the III-V epitaxy and 2) no external particles on the surface of the III-V and SOI chips. Fig. 3.3 shows different kinds of removable and immovable particles on the surface of the III-V sample. As shown in Figs. 3.3(a, b), there are removable particles on the III-V chip, while preparing the chip III-V sample. These particles are usually larger that the immovable particles deposited during growing the III-V epitaxy as shown in Figs. 3.3(c, d). In addition, the surface itself was not flat due to the crosshatch (Fig. 3.3(b)) and the wavy patterns (Fig. 3.3(d)), which could result from the strain in the epitaxy. It is reported that, for the DWB process, a root mean squared (RMS) micro-roughness of 0.5 nm is typically required [9]. In addition, if there is a particle with a 1 μm in diameter trapped during the DWB process, then it can create the unbonded area with 1 cm in diameter [79]. Therefore, it is essential to check the surface of the III-V and the SOI chips. If there are removable particles, then it should be removed.

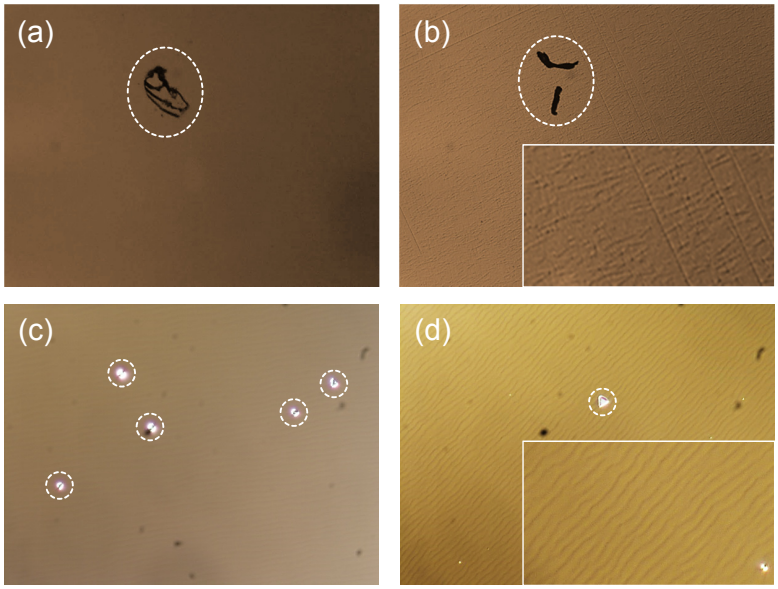

Figure 3.3: Nomarski microscopic images of different kinds of surfaces of III-V wafers. (a) Removable III-V debris adhering on the chip during cleaving the III-V wafer. (b) Removable thread or fiber from swab or from cleanroom wiper. The surface roughness shown in the inset due to the crosshatch during the epitaxy growth. (c) Immovable particles captured inside the epitaxy layers during growing the epitaxy. (d) Immovable particle and the wavy pattern on the surface.

Third, surface treatment processes are essential because there is no adhesive material; and hence, the bonding strength mainly depends on the surface treatments which will work as an agent for the covalent or ionic crystal bonds. The purpose of the surface treatments is primarily to increase the hydrophilicity of the surfaces and then the surface will be terminated with OH- groups more [76, 79]. In addition, during the covalent bond formed, the by-product gases such as H_2O or H_2 are generated and these by-product gases will degrade the bonding strength. The gases will form unbonded area at the interface and finally weaken the average bonding strength of the bonded sample.

Fourth, the generated by-product gases should be removed from the bonded interface to form a strong DWB. The by-product gases can be removed by introducing vertical outgassing channels. The outgassing channels will work as a gas container and as a passage to the bottom porous BOX layer where the gases can be diffused out [17, 76]. Therefore, the influence of the by-product gases can be effectively

Table 3.4: Direct wafer bonding procedure.

Step	Process	Function
1	RCA-1 cleaning	Rigorous cleaning for SOI and III-V chips
2	O_2 plasma treatment	1^{st} hydrophilic process
3	DIW treatment	2^{nd} hydrophilic process
4	Manual bonding	Bonding two chips using Van der Waals force
5	Mechanical bonding	Applying force and temperature to get strong bonding strength

removed by using the outgassing channel. Reflecting the four factors, the procedure of DWB process is summarized in Table 3.4.

3.3.2 RCA-1 cleaning

The III-V chip is covered with the PR to prevent from the physical particles and the possible surface scratch. Also, the InGaAs cap layer (Layer: 9) of the III-V chip protect the underneath layer from the organic contamination. First, the PR is stripped with the solvent cleaning process in an ultrasonic cleaner. Then, using a piranha solution (8 H_2O: 1 H_2SO_4 (97%): 8 H_2O_2 (30%)), the cap layer is removed. Next, RCA-1 solution (5 H_2O: 1 NH4OH (95−97%): 1 H_2O_2 (30%)) is prepared and then it is heated up to 80°C. If there are bubbles on the surface of beakers, then it is ready to conduct RCA-1 cleaning process. The SOI chip and the III-V chips are dipped into the solution. Since, the bubbles can easily swing the light-weight III-V chip, the two chips are put into the two different beakers. Otherwise, the III-V chip can land on top of the SOI chip, which may cause an undesirable scratch. After the RCA-1 clean, the chips are rinsed with DIW and then they are dried with N_2 gas.

3.3.3 Oxygen plasma and deionized water surface treatment

Two-step surface treatments are carried out to change the surface to a strong hydrophilic state. The RCA-1 cleaning process contributes to hydrophilicity as well. For the strong hydrophilic surface, O_2 plasma treatment is conducted using a

III-V reactive-ion etcher (RIE) [79, 89]. The plasma treatment with a low RF power is used to avoid creating surface roughness because the ions with intense energy can physically etch the surface. The O_2 plasma, therefore, chemically activate the surface as the hydrophilic state, and physically do not make the surface rough [79]. During the O_2 plasma treatment, the hydrocarbons and water-related species are removed, and the surface becomes more hydrophilic by forming a very thin oxide layer. After the plasma treatment, additional DIW treatment is carried out to further form polar hydroxyl groups($OH-$). The hydroxyl groups are involved in a Van der Waals interaction when approaching two chips closely. This force help the two samples mate spontaneously.

3.3.4 Manual and mechanical bonding

The two chips are carefully put on a clean wiper. If necessary, the surface of two chips is cleaned with N_2 gas to remove the possible physical particles. The back side of the III-V chip is held by using a sticky tip, and the chip is lifted up and then it is carefully put upside down on the center of the SOI. Then, the backside of the III-V chip is pressed down by applying force from the center to the boundary gradually. Then, this manual bonding process is confirmed by firmly pushing one side of the III-V chip with a tweezer. During the manual bonding process, if the surface of the III-V chip is flat enough with the RMS roughness of $\leq$1.0 nm and there is no particle on the surface, and then the mated sample is still strongly bonded after the test.

The bonded sample is loaded into a bonding machine (EVG NIL) to apply a force at an elevated temperature, which results in a stronger bonding strength. After loading the sample on the bonding machine, 4,000 N is applied for 2 hours at a temperature of 300°C . During this mechanical bonding process, a covalent bonding layer between two surfaces is formed, and by-product gases are generated. Under the 4,000 N, the applied pressure is about 3 MPa, which squeeze the by-product gases and help them to move into the outgassing channels [76]. To see the effect of introducing the outgassing channel on the top Si layer, the DWB was carried out without any outgassing channel. Figures 3.4(a, b) show the III-V

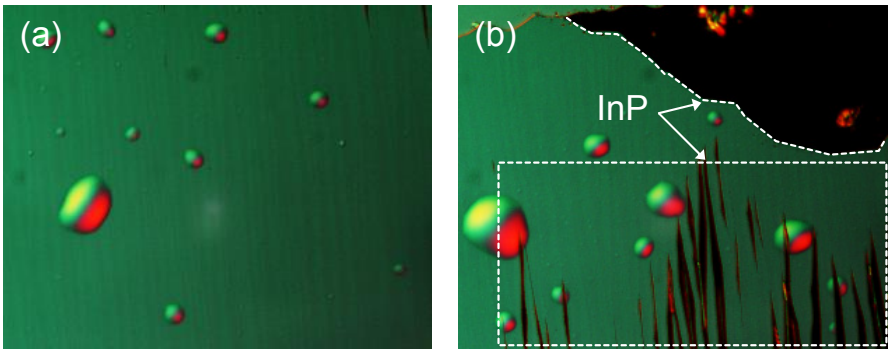

Figure 3.4: Nomarski microscope images of the bonded sample near the center and near the boundary of the III-V chip. (a) The by-product gases are captured at the interface between the III-V membrane and the SOI, which cause the diverse size of voids. (b) The remained InP is observed as black lines inside the white-dashed box and as black area indicated as the white-dashed line.

chip surface of a bonded sample after removing an InP substrate. The bonding process without transferring the outgassing channel was successful. However, there are a lot of voids with diverse sizes. Especially, if these voids are on the bottom grating patterns, the III-V layer is maybe detached from the SOI after defining a small III-V mesa. In Fig. 3.4(b), it shows the little amount of the remained InP substrate as black lines and black area. The impact of the remained InP will be explained in Section 3.3.5 in detail.

The schematic illustration of how to remove the by-product gases through the outgassing channel is described in Fig. 3.5(a). During the mechanical bonding

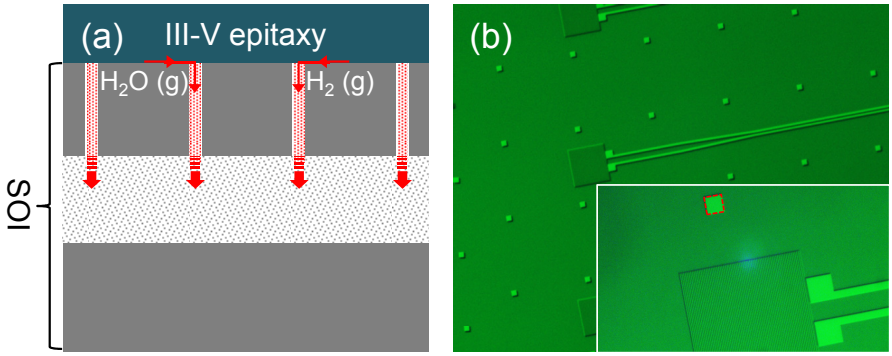

Figure 3.5: (a) Schematic illustration of the principle of removing the by-product gases via the outgassing channels. (b) Microscope images of ZEP mask pattern including the outgassing channels with 10 μm $\times$ 10 μm square pattern indicated as red-dashed square in the inset.

process, the generated gases can move along the boundary, and finally they can be captured inside the channel. Some gases can move further into the porous BOX layer while the the machine applies the force. The 7 μm $\times$ 7 μm square patterns are formed on the SOI for the outgassing channels. The distance between the square outgassing channels is 100 μm. Figure 3.5(b) shows the ZEP hard mask after developing it. In the inset of Fig. 3.5(b), the red-dashed square next to the HCG pattern indicates one of the outgassing channel masks. These patterns are transferred while the ASE process is conducted for forming the bottom HCG as explained in Subsection 3.2.3. The effect of introducing the outgassing channels is apparent as shown in Fig. 3.6. It illustrates the void due to the small particles and relatively large pattern. However, the voids due to the by-product gases are efficiently removed.

3.3.5 Substrate removal

The 350 μm-thick InP substrate needs to be removed. It is possible to use completely wet etching process without any mechanical lapping process. If the bonding process is done correctly, the bonding strength is high enough to resist the wet etchant. A magnetic stirrer is used to do uniform wet etch for the entire surface of the III-V chip, and HCl (37%) wet etchant is used. After reaching to the InGaAs etch stop layer, it is seen as a mirror-like surface. Then, the sample is rinsed with DIW and then it is dried with N_2 gas. It is essential to observe the surface with a nomarski microscope to confirm that there are no micro-sized InP residuals as shown in Fig. 3.6. Otherwise, the remaining InP will act as a hard mask during removing the InGaAs etch stop layer. As shown in Fig. 3.6, the hatched patterns on the entire surface of the InGaAs etch stop layer result from being slightly etched away by the HCl solution. Also, during the 1 hour-long wet etching process, the edges are slightly etched from the boundary as shown in Fig. 3.6(a). This is because the other InP layers such as the cladding layers are etched away slowly from the side. When determining the size of the III-V chip as explained in Section 3.1, the width of the etched boundary was considered as well. Therefore, the final III-V membrane still covers the entire bottom patterns. The effect of the small particles or relatively

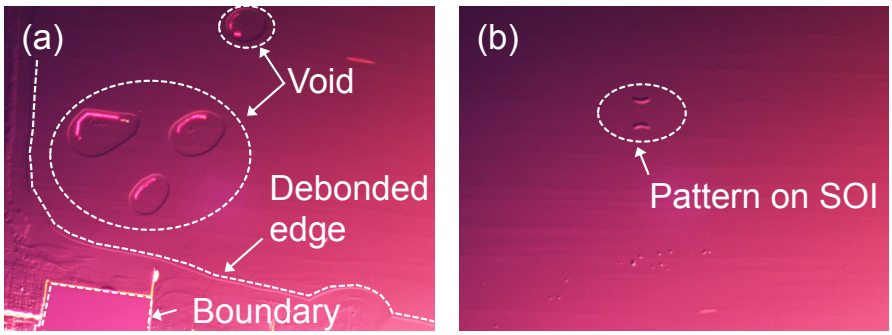

Figure 3.6: Nomarski microscope images of the surface of the III-V chip after removing the InP substrate. (a) Small particles or local surface protrusion can cause the unbonded or void area. The un-bonded area in the left lower side shows the edge of the III-V chip. (b) The center of the III-V chip shows the void-free area except the voids due to a relatively large pattern on the bottom SOI indicated as white-dashed circle.

large patterns can be seen as well in Fig. 3.6. These particles cause unbonded area where the byproduct gases are accumulated; and therefore, the voids finally appears after removing the InP substrate. In addition, if there is large enough pattern such as alignment marks or waveguides, then these patterns can become the container of the by-product gases as well. It is common that, around the boundary of the III-V chip sample, there are protruded InP structures as shown in Fig. 3.4(b). This is because of the anisotropic etch rate [90]. The width of the protruded InP structures are $\sim$500 μm and the edges are still far away from the central grating and waveguide patterns. For the purpose of planarization, the boundary protrusions are easily removed by using the tungsten tip by pushing them from inside to outside direction. The relatively bulky InP is easily broken and it detached from the III-V membrane.

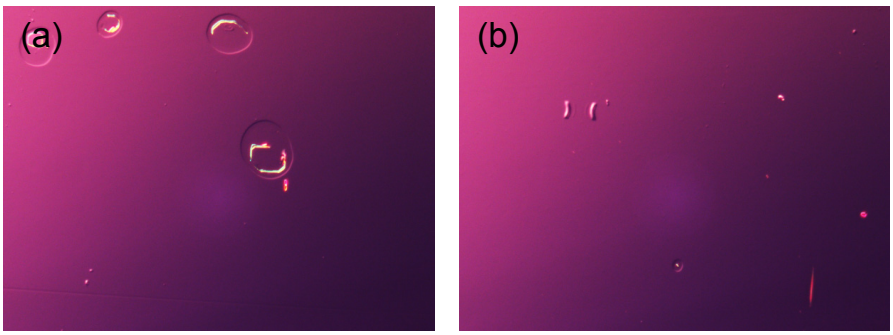

Figure 3.7: Nomarski microscope images of the surface of the III-V chip after removing the InGaAs etch stop layer. The two images show flat surface except the voids due to the particles, protrusion, or relatively large patterns.

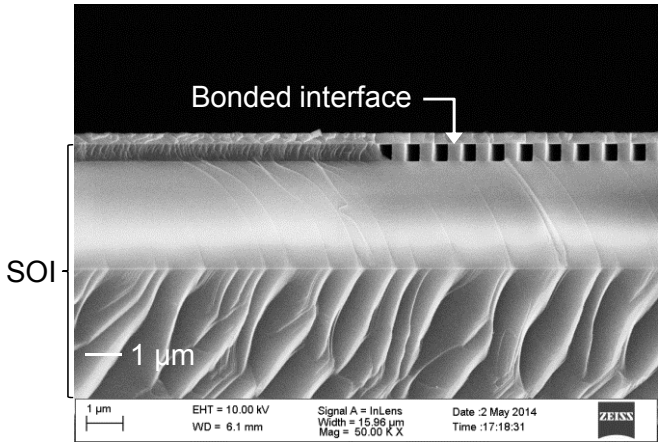

Figure 3.8: Cross-sectional SEM image of the bonded sample shows the interface of the III-V chip membrane and the SOI near the boundary of the HCG and the un-patterned Si region.

Sequentially, the InGaAs etch stop layer is removed by using piranha solution and then it become the flat surface as shown in Fig. 3.7. The exposed top layer is then InP cladding layer (the 2-nd layer in Table 3.1) and the bonding process is done. The cross-sectional SEM image of the bonded interface near the bottom HCG is shown in Fig. 3.8. It is evident that not only the unpatterned area but also the patterned area are bonded well. Now, the heterogeneously integrated sample is ready for the subsequent photolithography processes to fabricate the laser device on top of the SOI chip. It should be mentioned that the surface inspection should be done under the nomarski mode microscopy to observe these patterns.

3.4 Mesa Definition

After the substrate removal process, the III-V chip becomes a membrane with a thickness of ∼749.2 nm. To define a mesa pattern, a silicon nitride (Si_3N_4) hard mask with a 200-nm thickness is used, which has a high selectivity (>10) to the underlying III-V material. Using a plasma-enhanced chemical vapor deposition (PECVD), a Si_3N_4 layer is deposited. The chamber temperature of the PECVD is 250°C, and during the deposition, the thin III-V layer is not delaminated or debonded due to the applied temperature. To define Si_3N_4 mesa, a positive AZ 5214E PR is used as a mask. With the PR mask, Si_3N_4 hard mask is formed using

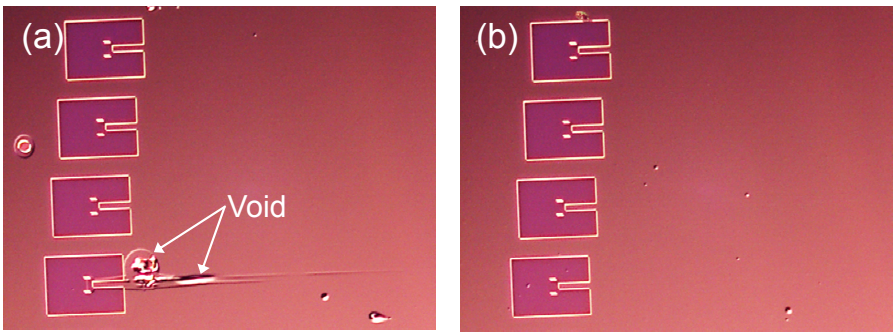

Figure 3.9: Microscope images of Si_3N_4 hard mask patterns. (a) Voids outside the hard mask. (b) Hard masks transferred on the void-free sample.

a III-V reactive-ion etcher (RIE). After removing the PR mask, the transferred Si_3N_4 mask is shown in Fig. 3.9. With the Si_3N_4 hard mask, a III-V mesa is defined using the III-V RIE. If there is a void near the mesa pattern, the III-V mesa can be detached from the SOI after all. However, if it is outside of the mesa region as shown in Fig. 3.9(a), the III-V mesa will not be detached after conducting the mesa definition. During the dry etching process, the sample is observed using the installed IR camera and the laser endpoint detector. The real-time IR image is used to determine when the dry etching should be stopped. While the dry etch continues, the thickness of the III-V membrane become thinner; and hence, the bottom outgassing channels and the waveguide patterns are observed. In addition, the signal of the endpoint detector is used to determine whether the III-V mesa

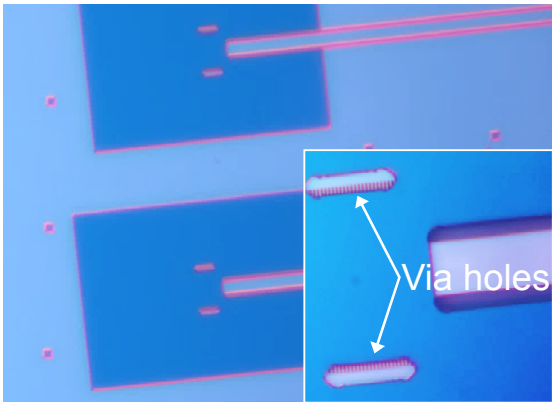

Figure 3.10: Microscope image of the transferred III-V membrane mesa with the Si_3N_4 hard mask. The inset shows the zoom-in microscopy image and the bottom grating can be seen via the two via holes.

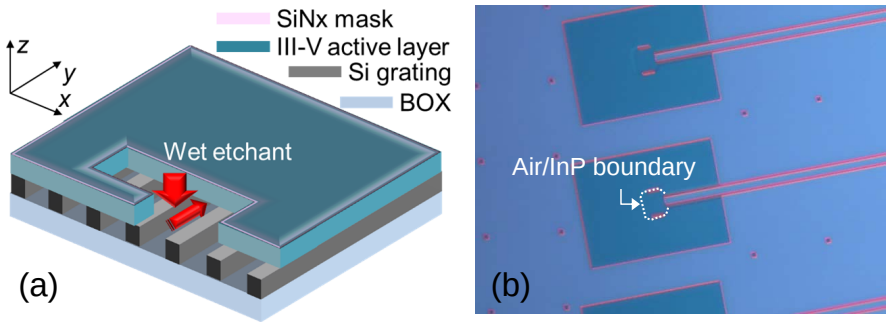

Figure 3.11: (a) Schematic illustration of how the InP bonding layer is removed using both the via holes and the air part of the bottom HCG. (b) Nomarski microscope image of the sample after removing the InP bonding layer.

pattern is completely done. If there is no signal variation, then it indicates that the dry etching process is done. After finishing the dry etch, the sample is inspected under the nomarski microscope whether the dry etch is done without any remaining thin layer as shown in Fig. 3.10. Next, the thin bottom InP layer (the 8-th layer in Table 3.1) should be removed. The InP layer works as a bonding interface outside the bottom HCG and as a part of a sacrificial layer around the HCG. Around the HCG region, the InP layer should be removed to introduce a low-index air gap. To remove the InP layer, HCl solution is used, and the Si_3N_4 mask is still on the III-V sample on top of the top InP cladding layer because it can protect the top InP layer from the HCl solution. Fisrt, the wet etchant flows along the two via holes and then passes along the air part of the bottom HCG as schematically explained in Fig. 3.11(a). In this way, the thin InP layer is removed as shown in Fig. 3.11(b). At particular condition of the nomarski mode, the air/InP boundary is observed as shown in Fig. 3.11(b), which was not observed in Fig. 3.10. This boundary is used to confirm whether the bottom InP is removed or not. Then, the Si_3N_4 mask is removed using HF solution by dipping the sample in the solution for ∼2 min. During the HF wet etching process, it is observed that the air/InP boundary and the mesa boundary are slightly affected by the HF wet etchant as shown in Fig. 3.12. If there is a thin InP layer or some part of it is remained inside, then it will block the piranha solution to remove the next InGaAs sacrificial layer. Especially, if there is the remained part around the center of the HCG, then this will drop the reflectance

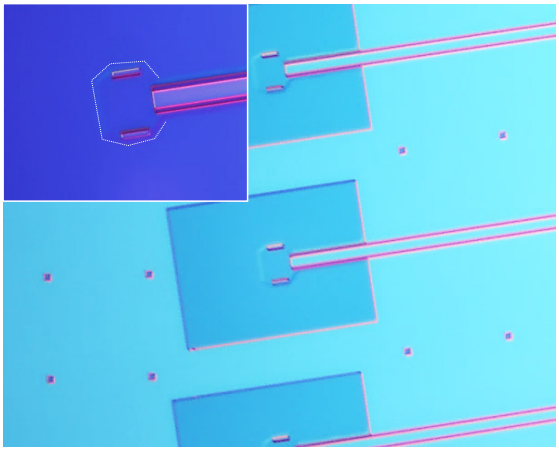

Figure 3.12: Nomarski microscope image of the sample after removing the Si_3N_4 hard mask. The inset shows the zoom-in image, and the area of the boundary indicated with a white dotted line is almost same after removing the hard mask.

of the bottom HCG. Then, the low reflectance will not meet the lasing condition. In addition, it is impossible to do additional wet etch for the remained InP after doing the InGaAs etching process. This is because of the some exposed InP cladding layers (the 4-th and 6-th layer in Table 3.3) after removing the InGaAs layer.

One important consideration to do uniform and complete sacrificial etching inside the HCG region is that the position of two via holes should be introduced along the direction perpendicular to the grating bars as shown in Fig. 3.11(a). Otherwise, the wet etching rate of InP and InGaAs will become slower because each Si grating bar will block the wet etchant. This will increase the total etching time, leading to damage of the cladding InP and InGaAlAs active layers.

3.5 DBR Formation

For a top mirror, a dielectric distributed Bragg reflector (DBR) is employed because the refractive index contrast (Δn) is larger when compared to an epitaxial DBR. The epitaxial DBR needs to consider the lattice matching condition, which limit the range of material selection, and it provides a small index contrast [47, 49]. As shown in Fig. 3.13, there are two ways to form the dielectric DBR: an etch back process and a lift-off one. The both processes are used to form DBR considering deposition machines and dielectric material compositions.

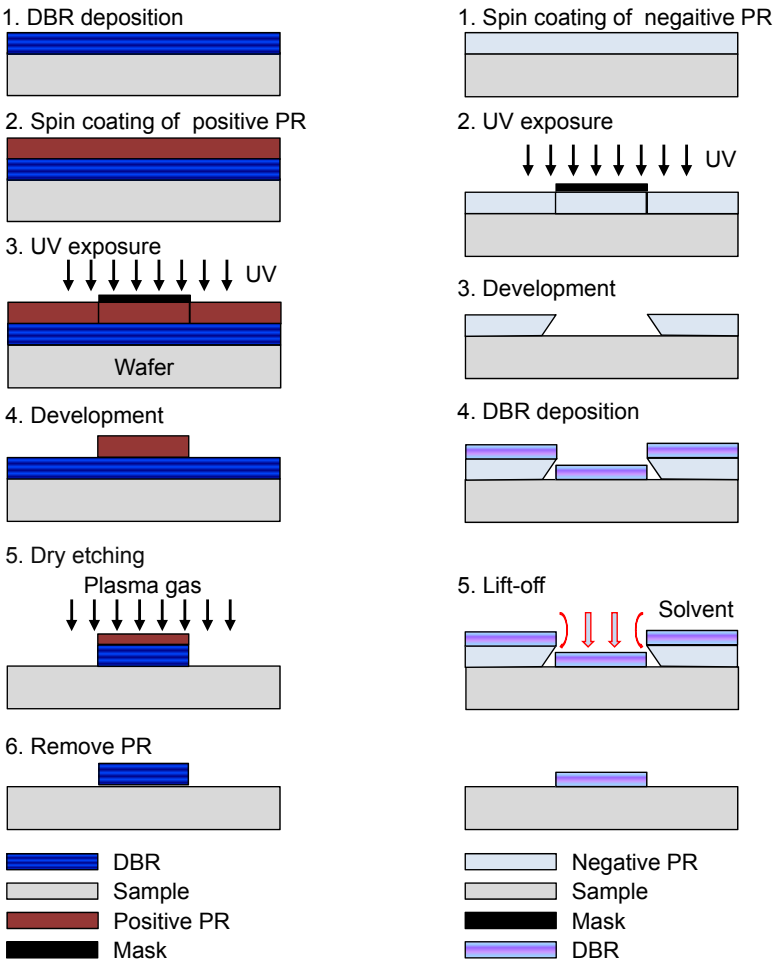

Figure 3.13: Schematic illustrations of two kinds of DBR formation procedures. Etch-back procedure in the left column and lift-off procedure in the right column.

The lift-off process is developed for the DBR formation using an ion beam deposition (IBD) machine. The high-index material of titanium dioxide (TiO_2) and the low-index material of silicon dioxide (SiO_2) are used. The etch-back process is done using a III-V dielectric evaporator. For the III-V dielectric evaporator, a-Si and SiO_2 sources are used, and the Δn is higher than that of the TiO_2/SiO_2 composition. Therefore, the number of pairs of the DBR is reduced to obtain the same reflectance, and an energy penetration depth can be shorter than that of TiO_2/SiO_2 DBR. The optical properties of each material are shown in Appendix C.

3.5.1 Lift-off process

A lift-off process is a well-known process for the ohmic contact metallization process in semiconductor fabrication technique. To employ the lift-off process for DBR formation, the similar factors should be considered. First, the thickness of the PR should be larger than that of the DBR. Second, an undercut should be wide enough to open a path for the solvent to melt the PR during lifting off the PR. These two factors will determine the success of the lift-off process. A negative AZ nLOF 2070 PR is chosen because of the thermal stability up to 250°C and the maximum thickness as much as ∼7 μm. In addition, the undercut profile can be easily adjustable to prevent the sidewall being coated. The PR is spun on the sample at 4000 rpm and the measured thickness is ∼6.5 μm. By controlling the developing time of the PR, the undercut width is controlled. The cross-sectional SEM images of the controlled undercut using a ridge mask are shown in Figs. 3.14(a, b). The development time is 85 and 110 sec, respectively, and the corresponding

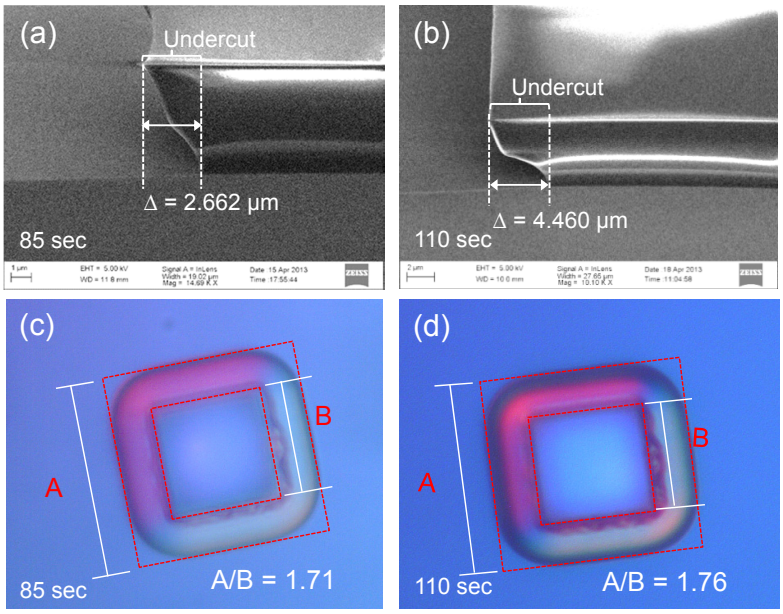

Figure 3.14: (a, b) SEM images of the cross-sectional view of the undercuts patterned with a ridge pattern mask. The width of the undercut is controlled by the developing time of (a) 85 and (b) 110 sec, respectively. (c, d) Nomarski microscope images of the top view of the square opening for DBR formation developed for (c) 85 and (d) 110 sec, respectively. The 'B' indicates the length of the aperture and the 'A' indicates the width of the undercut.

undercut width is 2.662 and 4.460 μm. Using the square mask for forming a DBR, the negative PR is tested as well. The top-view microscope images of the PR mask are developed for 85 and 110 sec, respectively, and they are shown in Figs. 3.14(c, d). The ratios of the undercut (A) to the aperture width (B) are 1.71 and 1.76, respectively. Based on the development condition of 85 sec, IBD is used for depositing a DBR with a SiO_2 and a TiO_2 materials. The width of the undercut is within the two via holes as shown in Figs. 3.15(a, b). If the undercut is wider that the two via holes, then the DBR sources is deposited along the sidewall and block the via holes which are used for the last sacrificial etch. Before depositing the full DBR, each single layer is deposited to measure the refractive index of the SiO_2 and the TiO_2, respectively, using an Ellipsometer VASE (J.A. Woollam Co., see Appendix C). The calculated deposition rates are around 0.5/1.0 Å/sec. These refractive indice and deposition rates are used to deposit the full DBR. Besides, the measured temperature of a sample holder during the single layer deposition process is below 100 °C. Nevertheless, the long deposition process can influence the PR in the end;and hence, a cooling gas from the backside of the sample holder is applied. After

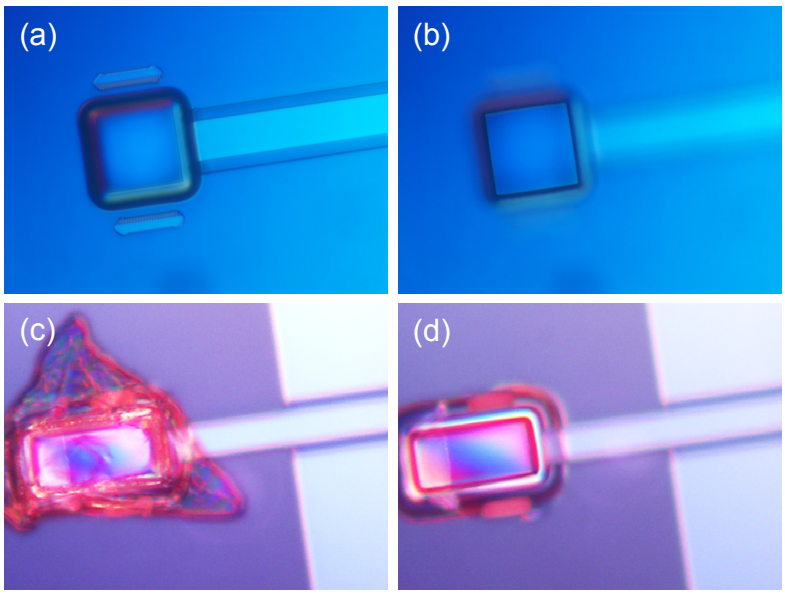

Figure 3.15: (a, b) Microscope images of a developed negative 2070 PR pattern which are taken by focusing (a) on the undercut and (b) on the opening. (c) Microscope image of an entangled PR and sources along the boundary of the DBR. (d) Microscope image of the DBR after removing the entangled residue by using a plasma asher.

the deposition is finished, the sample is dipped in acetone until the PR is removed. Around the DBR boundary, due to the small amount of sources deposited along the sidewall, entangled residues are remained as shown in Fig. 3.15(c). Using a plasma asher with a 40% power, the residue is effectively removed and finally the DBR is remained as shown in Fig. 3.15(d). The formed DBR shows uniform thickness around the center part of the DBR, whereas around the boundary it is deformed due to scattering of the deposition sources at the boundary of the PR. Therefore, using the lift-off process, there is a limit to define the DBR smaller than a certain area because of the non-uniform surface. Around the boundary, the reflectance and the phase are differ from the center of the DBR, which influence the lasing condition.

3.5.2 Etch-back process

The etch-back process is a top-down process to define a DBR area. For the etch-back process, a III-V dielectric evaporator is used, which contains high-index and low-loss a-Si as a high index material and SiO_2 as a low index material for DBR formation. For the a-Si source, it is necessary to heat up the source up to 250°C to get low loss material. This makes the use of a-Si impossible for the lift-off process, which needs a low temperature condition. For the etch-back process, it is possible to form a uniform and smaller DBR when compared to the DBR formed using the lift-off process. After depositing the DBR layer, a positive AZ 4562 PR is used as a mask. The 4562 PR is spun at 3000 rpm and then it is exposed to UV for 14 sec. The exposure time of the UV is influenced by the reflectance of the DBR as well. If the DBR exhibit a high reflectance to the UV light, then the UV-exposed PR shows a lot of bubble-like pattern on the PR layer, which may not work as a mask correctly. To solve this problem, the exposure time is reduced. Next, the dry etching is carried out using a III-V inductively coupled plasma RIE (ICP RIE). Then, acetone/ethanol/isopropyl alcohol (IPA) are subsequently used to strip the PR. Last, the plasma asher is used to remove the remained PR along the DBR boundary. The transferred DBR is shown in Fig. 3.16(a) and the inset shows the boundary of the DBR defined by the

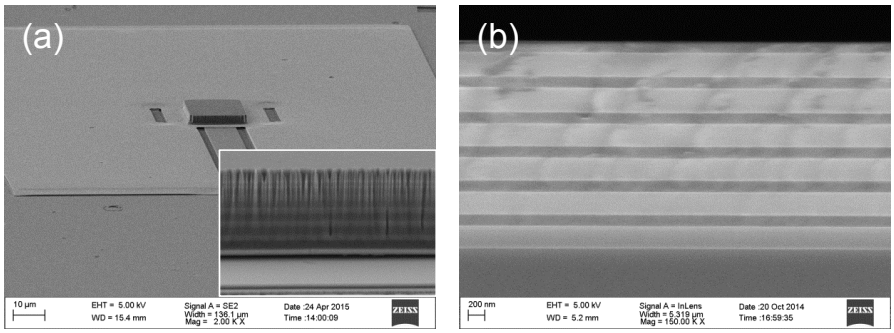

Figure 3.16: (a) SEM image of the fabricated laser and the small square on the center indicates the DBR formed by using the etch-back process. The inset shows the zoom-in image of the side will of the DBR. (b) SEM image of the cross-sectional view of the DBR.

ICP RIE. The cross-sectional SEM image of the DBR is provided in Fig 3.16(b) and the low- and high-index alternating layers are clearly seen.

3.6 Sacrificial Layer Etching

Last, it is necessary to introduce thick-enough low-index material above the grating. Otherwise, the bottom grating cannot work as a HCG reflector. The thin InP layer was already removed and then the remaining InGaAs sacrificial layer should be removed using a wet etchant, piranha solution. For this etching process, it does not need any mask to protect III-V layer because the top and bottom cladding layer will work as a mask from the InGaAs etchant. Fig. 3.17(a) shows the failed case of the sacrificial wet etch due to the mistakenly repeated InP and InGaAs wet etch. When conducting the InGaAs sacrificial etch, it seemed that the thin InP layer was not clearly removed, which was conducted after the mesa definition (see section 1.4 and Fig. 3.11). To remove the probably remained InP layer, the InP wet etching is carried out one more time. However, this process remove the top InP cladding layer, which is not covered with a Si_3N_4 hard mask any more. Also, the bottom InP cladding (Layer: 6) is removed because the thin InP layer (Layer: 8) and InGaAs (Layer: 7) were subsequently removed during the former etching processes. As a result, the whole III-V layer was destroyed and the bottom HCG can be seen through the DBR. Fig. 3.17(b) shows the sample after carrying out

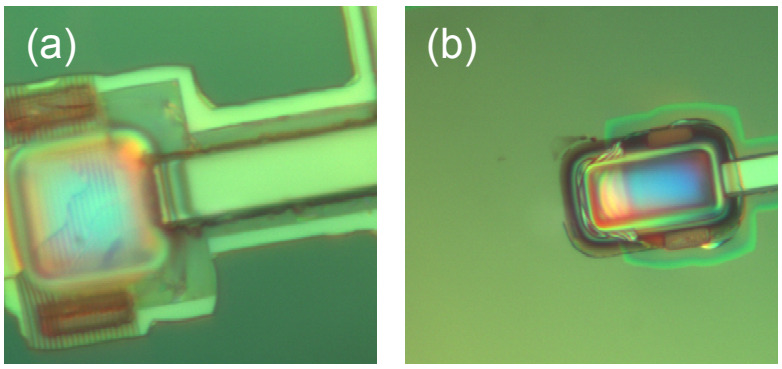

Figure 3.17: (a) Microscope image of one sample undergone repeated InP and InGaAs wet etching process. It removes the InP cladding and MQWs, and then the bottom grating is seen through the top DBR. (b) Microscope image of the sample after a successful sacrificial wet etching process to introduce air layer above the bottom HCG.

successful sacrificial wet etch. The differently colored region near the DBR and the waveguide indicate the boundary where the sacrificial layer etch was done.

3.7 Summary

To sum up, the overall fabrication procedures for implementing Si-integrated hybrid VCLs have been developed. For the hybrid VCLs, the direct wafer bonding (DWB) is the key fabrication process to integrate the III-V active layer with the bottom HCG transferred on the top Si layer of SOI platform. More importantly, the DWB process has been conducted at a temperature as low as 300°C. In addition, for the long wavelength VCLs, the 'lift-off' and 'etch-back' process were developed to form top dielectric DBRs. All the fabrication steps, which developed for realizing the hybrid VCL, are CMOS-compatible processes.

"To invent,
you need a good imagination and a pile of junk."

— Thomas A. Edison

4

Si-integrated Long-wavelength Hybrid Vertical Cavity Laser

Contents

4.1 Introduction

Recently, there has been growing interest in the research and experimental demonstration of silicon-integrated long-wavelength (λ = 1310 or 1550 nm) lasers in order to fulfill the need for optical interconnects or silicon (Si) photonics applications. The first Si-integrated laser was demonstrated using an evanescent laser structure with a Si waveguide transferred on the top Si layer of a silicon-on-insulator (SOI)

platform [15,91]. Thereafter, using a Si grating structure on a SOI as a cavity [18,92], Si-integrated lasers were demonstrated with a threshold current of 8.8 mA with a short cavity distributed feedback laser (SC-DFB) [18] and 4 mA with a resonant grating cavity mirror [92]. The SC-DFB has a 3 dB bandwidth of 9.5 GHz and 12.5 Gb/s direct modulation as well. This edge-emitting type laser has similar properties as the conventional edge-emitting laser, and they both consume more energy when compared to a small cavity lasers such as vertical-cavity surface-emitting lasers (VCSLEs) or photonic-crystal (PhC) lasers. To reduce the energy consumption dramatically, a PhC cavity is used which can reduce the cavity mode volume to less than 1 μm^3 [93, 94]. The Si-integrated PhC laser with a threshold current of 31 μA has been reported [19]. The two types of lasers structurally emit light into the in-plane direction which makes them relatively convenient to couple the output into silicon photonic-integrated circuits.

The other type of laser is VCSEL which is a proven excellent light source because of small energy consumption and high-speed modulation response with high-enough output power [39, 95, 96]. Recently, using a 1530 nm VCSEL, a modulation speed of 56 Gb/s without forward error correction (FEC) has been demonstrated [97]. Furthermore, it has been numerically demonstrated that light can be emitted from a vertical cavity laser (VCL) laterally into a Si waveguide using a high-contrast grating (HCG) reflector [25]. The laterally-emitting VCL can have the same optical property as the VCSELs: a high relaxation oscillation frequency and a low threshold current. Therefore, for on-chip optical interconnect applications, a Si-integrated long-wavelength hybrid VCL which can emit light along the in-plane direction will be an attractive option.

In this chapter, Si-integrated long-wavelength hybrid VCLs are investigated focusing on two points: 1) the possibility of in-plane emission and 2) the feasibility of high-speed operations. First, an in-plane hybrid VCL structure is explained and then experimentally demonstrated using a bottom Si HCG transferred in the top Si of a SOI platform. The experimental results show the possibility of the in-plane coupling of the vertically-resonant light laterally into an in-plane Si

waveguide by using the bottom HCG as a bottom reflector as well as an in-plane light guiding structure. Second, a high-speed hybrid VCL using a high-index-contrast dielectric DBR and a bottom transverse magnetic (TM) HCG is experimentally demonstrated. It shows a 3 dB frequency of 27 GHz and an estimated modulation current efficiency factor of 42.1 GHz/mA$^{1/2}$ at a lasing wavelength of 1541 nm. This property proves that the high-speed VCL structure has the potential to transmit data at high-speeds with low-energy consumption.

4.2 In-plane Emission Laser with Vertical Cavity Structure

VCSELs have many advantages for energy-efficient short-reach optical communication purpose [96], and one of them is the high coupling efficiency between the VCSELs and an optical fiber aligned in vertical direction [98–100]. When it comes to on-chip optical interconnect application, VCSELs become less favorable light source due to the vertical cavity structure. For the optical interconnects, it is needed to use additional complex scheme such as flip-chip bonding process and additional in-plane guiding structures to couple the vertical emission into in-plane direction [22, 101].

For in-plane emission lasers using vertical cavity structure, the fully monolithically-integrated structure was numerically suggested using shallow gratings on a waveguide

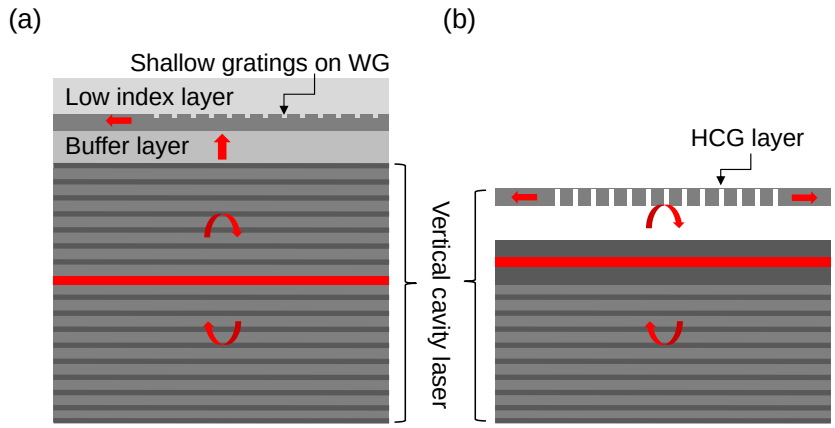

Figure 4.1: Schematic illustrations of VCSELs with in-plane emission. (a) Monolithically-integrated VCSELs with an in-plane waveguide [23]. [WG: waveguide] (b) VCSELs with a top HCG layer working as a top mirror and an in-plane waveguide [24].

layer as shown in Fig. 4.1(a). Above the vertical cavity laser, the additional low-index buffer layer and waveguide layers are epitaxially grown. On the waveguide layer, shallow gratins are introduced to guide the vertically emitted light into the in-plane direction [23]. Additional low index layer is deposited on top of the grating to make an almost symmetric slab waveguide. The other approach was suggested in [24], which uses a HCG mirror as a reflector as shown in Fig. 4.1(b). The top HCG is a top mirror of the vertical cavity laser as well as in-plane guiding structure. The in-plane emission can be dominantly achieved by tailoring the HCG parameters. If the photon lifetime to the in-plane direction (τ_g) become shorter than that of the vertical direction (τ_r), the in-plane emission become dominant [24]. Similarly, a HCG is used to guide a vertically incident light into an in-plane direction and the guided light is detected by using a photo-detector (PD), which is incorporated on the same layer where the HCG is formed [64]. Nevertheless, these structures cannot be directly used for the on-chip optical interconnect applications because the in-plane output still needs to be coupled into a Si waveguide.

4.3 Hybrid Vertical Cavity Laser with In-plane Emission

For the short-reach optical interconnect and silicon photonics applications, it is needed to integrate a light source onto a Si platform with high integration density. Since edge emitting lasers emit light along the in-plane direction, it is more favorable to adopt edge-emitting type lasers on the platform with less complexity because there will be less difficulty to couple the laser light into the planar photonics integrated circuits. By using a direct wafer bonding (DWB) process and grating mirrors which is transferred in a Si platform for an in-plane cavity, a Si-integrated edge-emitting lasers has been demonstrated [15]. Since the bottom Si grating is directly connected to a Si waveguide, there is no need to introduce additional light coupling structure. In a similar way, vertical cavity lasers (VCLs) with an in-plane emission can be demonstrated by employing a bottom HCG and/or HG reflector. Using the DBW process and the bottom HCG transferred on a SOI platform, a

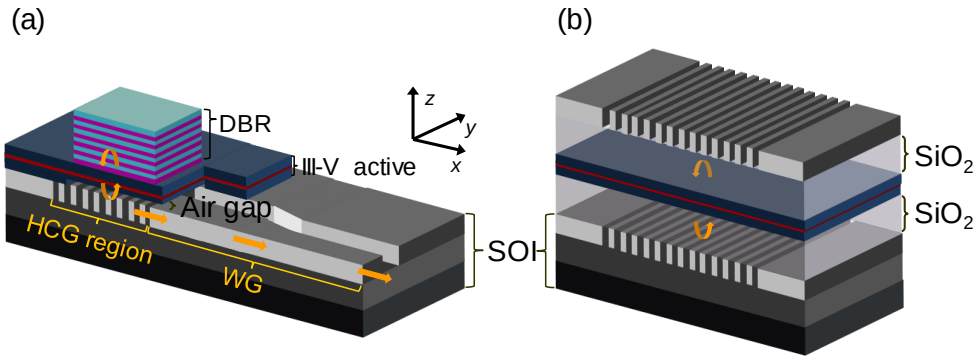

Figure 4.2: Schematic illustration of Si-integrated hybrid vertical cavity lasers (VCLs) with in-plane emission integrated on a SOI platform. (a) Hybrid VCL with a top dielectric DBR and a bottom HCG transferred on the SOI platform. [WG: waveguide] (b) Double-HCG VCL on the SOI platform.

hybrid VCL have been suggested as shown in Fig. 4.2(a) [25]. The bottom HCG is surrounded by a thin air gap (region I) and a buried oxide layer (BOX, region II). In addition, double-HCG VCL structure have been suggested as shown in Fig. 4.2(b) [68]. For the double HCG structure, there are thick SiO_2 low-index spacers because the top and bottom HCG need to be surrounded by the thick low-index materials. The thickness condition, which depends on the type of HCG, will be discussed in the next section. The direction of in-plane emission of the double-HCG structure relative to the grating bar was not mentioned in [68]. The VCL structures are similar to VCSEL structure, which has small cavity, except for the direction of light emission; and hence, it can inherit all the advantages of VCSEL, i.e., low threshold level and high relaxation resonance frequency, which are ideal for the short-reach optical interconnect and data center applications. For the high-speed operation of VCLs at the long wavelength of 1550 nm, it is needed to investigate the energy penetration depth into the mirrors, which is related to the intrinsic resonance frequency via the vertical confinement factor [38].

4.3.1 Laser structure

To use long-wavelength VCLs for optical interconnect applications, it is desirable to use a bottom Si HCG transferred in the top Si layer of a SOI wafer where the silicon photonic-integrated circuits (PICs) are established for on-chip or chip-to-chip

optical interconnects. As shown in Fig. 4.2(a), the vertical cavity structure can emit light laterally [25]. The hybrid VCL consists primarily of three parts: 1) a top dielectric DBR, 2) an InP-based III-V active layer, and 3) a bottom HCG region which is used as high reflective mirror. Besides, the HCG can route the vertically-resonant light into an adjacent in-plane Si waveguide. This in-plane emission can be efficiently done by tailoring the position of the excited beam relative to the boundary between the one end of HCG and the waveguide. Below the buried-oxide (BOX) layer, there is a thick Si substrate which is not shown in here. The top dielectric DBR is comprised of 7 pairs of TiO_2/SiO_2 ($n_{TiO_2} = 2.32/n_{SiO_2} = 1.47$). The III-V layer is 1λ thick and contains 7 InGaAlAs/InGaAlAs strained quantum wells (QWs). The bottom HCG is surrounded by low refractive index materials; and hence, it can show a high reflectivity over a broad wavelength range. The top low index material is air and the bottom is BOX. Both the HCG and the Si waveguide are formed in the top Si layer of the SOI wafer.

In the vertical cavity as shown in Fig. 4.2(a), light is amplified vertically between the top DBR and the bottom HCG reflector, and then the vertically-resonant light can be emitted through the Si waveguide. The HCG is designed to have reflectivity of more than 99.5% for a TM-polarized light. Since TM HCGs need generally thinner low index layer above and below the grating when compared to TE HCGs, a TM HCG reflector is employed. The effect of employing TM HCG on the dynamic property of a laser will be discussed in the next section. If TE HCGs are employed, the laser structure become relatively bulky as shown in Fig. 4.2(b), which results from the SiO_2 spacers. Figure 4.3(a) shows an excited fundamental mode profile of $|H_y|$ field of the long-wavelength Si-integrated hybrid VCL with an in-plane emission which is obtained using the finite-difference time-domain (FDTD) method [25]. The fundamental mode is excited inside the vertical cavity, and at the boundary between the HCG and the Si waveguide indicated with the white dashed circle, a small portion of the tail of the fundamental mode excites the Si waveguide mode and it is guided along the Si waveguide. As shown in Fig. 4.3(b), the lasing mode inside the cavity and the propagation mode in the Si waveguide

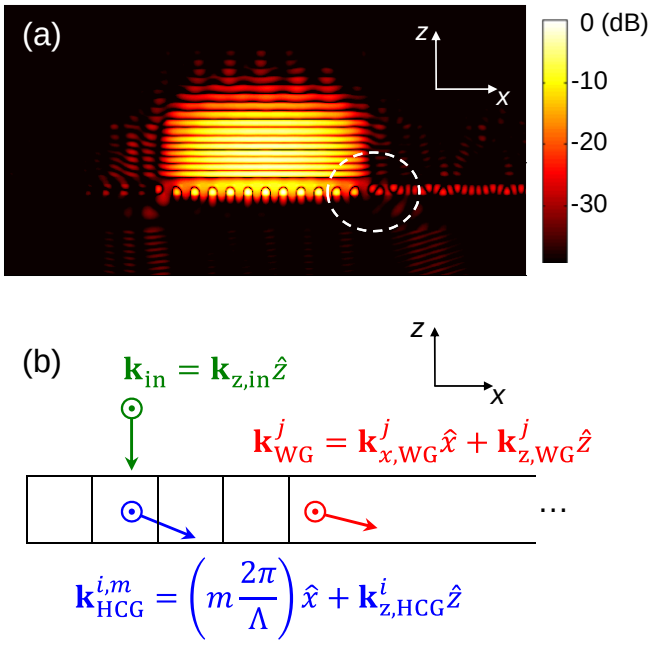

Figure 4.3: (a) Fundamental mode profile of $|H_y|$ field of the long-wavelength Si-integrated hybrid VCL and (b) H_y fields and wave-vectors of modes within the white dashed circle. $\mathbf{k}_{in}$: wave-vector of the vertically incident light. $\mathbf{k}_{HCG}{}^{i,m}$: wave-vector of the m-th harmonic of the i-th HCG eigenmode. $\mathbf{k}_{WG}{}^{j}$: wave-vector of the j-th waveguide mode.

are illustrated with the wave-vectors around the white dashed circle. The vertically incident light with a wave-vector of $\mathbf{k}_{in}$ excites the eigenmodes of the HCG expressed with wave-vectors, $\mathbf{k}_{HCG}{}^{i,m}$. Since the $\mathbf{k}_{HCG}{}^{i,m}$ includes harmonic components of x-direction, the excited HCG eignemodes can be coupled to the Si waveguide mode with a wave-vector, $\mathbf{k}_{WG}{}^{j}$. The mode conversion scheme and the maximum mode conversion efficiency can be found in [25], which suggested the in-plane hybrid VCL and conducted the numerical investigation of it.

4.3.2 Fabrication result

To confirm the feasibility of in-plane emission using the vertical cavity structure, an optically-pumped laser structure shown in Fig. 4.2(a) is fabricated using the CMOS-compatible processes: 1) electron-beam lithography, which is used for transferring the HCG region and the Si waveguide onto a SOI wafer, 2) a direct wafer bonding process for heterogeneously integrating the III-V active layer onto the SOI wafer [76, 79], and 3) a lift-off process for forming a dielectric DBR. In addition, a selective wet

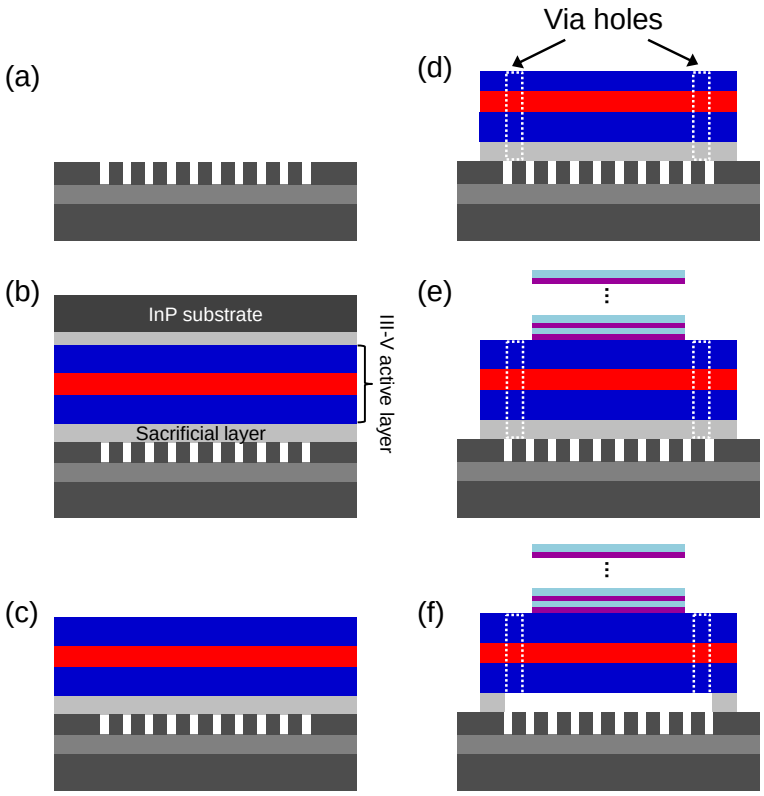

Figure 4.4: a) HCG and Si waveguide pattern (not shown here) were formed in the Si layer of a silicon-on-insulator (SOI) wafer by using electron-beam lithography and dry etching. b) The SOI and a III-V sample were rigorously cleaned using a standard RCA-1 (H_2O:H_2SO_4:H_2O_2) cleaning process. The III-V sample was put upside down on the SOI sample manually; and then, the bonded sample was loaded on a bonding machine with applying force and temperature. c) InP substrate and thin InGaAs etch stop layers were removed using wet etchant in sequence. d) Mesa pattern for the III-V layer was defined by using a Si_3N_4 hard mask and reactive ion etching (RIE) process. At the same time, two via holes were defined to introduce an air gap above the HCG. e) Then, using a lift-off process, 7 pair SiO_2/TiO_2 DBR layer were formed. f) To introduce the air gap, the sacrificial layer were subsequently removed through the two via holes by using wet etchant.

etching process is conducted to introduce an air gap between the III-V layer and the HCG. Each fabrication process is explained in Chapter 3 in detail. The simplified fabrication procedure is illustration in Fig. 4.4. The fabricated Si-integrated long-wavelength hybrid VCL is shown in Fig. 4.5 as well as the depiction of light propagation along the in-pane waveguide. The DBR boundary is rounded due to the property of the lift-off process, which is explained Chapter 3. To measure the in-plane emission from the Si waveguide, the fabricated device was cleaved so that the Si waveguide end is exposed to the air.

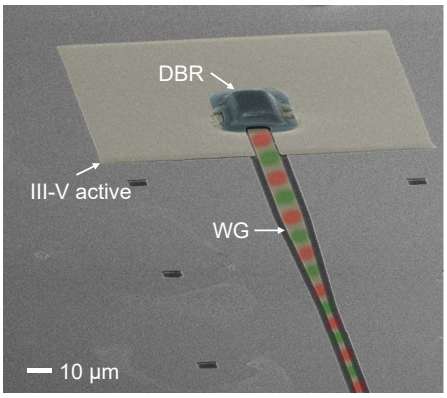

Figure 4.5: A false colored SEM image of the fabricated sample with an overlaid light propagation image along the waveguide.

4.3.3 Characterization result

The optically-pumped in-plane hybrid VCL is characterized using the setup shown in Fig. 4.6(a). The microscope unit is used to guide a pump laser into the top DBR of the test sample vertically. To collect the lasing output of the hybrid VCL, the objective lens and the fiber coupler are used for the vertical emission, and a lensed or multi-mode (MM) fiber is used for the in-plane emission. The collected output is sent to the micro-PL setup. A 980 nm pump laser is used under a pulsed operation with a 2% duty cycle (f_{pump}) and 5 MHz repetition rate. The top DBR stopband extends to 1300 nm (see Appendix C), so a 1300 nm laser, which would avoid light absorption in the Si layer and subsequent heating problem, cannot be used. This is the reason why the pulsed operation is used. For Si-integrated long-wavelength hybrid lasers, a thermal shunt design can be adopted to dissipate the thermal energy accumulated in the active region efficiently [108]. The sample is loaded onto an un-cooled stage. Then, the pump laser is focused onto the top DBR using the microscope setup that includes a 50x near-infrared (NIR) objective lens. The transmitted power, T_a of the pump laser after passing through OL is 21%. The pump level is controlled by using an attenuator and monitored by reading an optical power meter which is connected 1% branch of an optical fiber coupler. To characterize the in-plane emission, the MM or lensed fiber is approached and

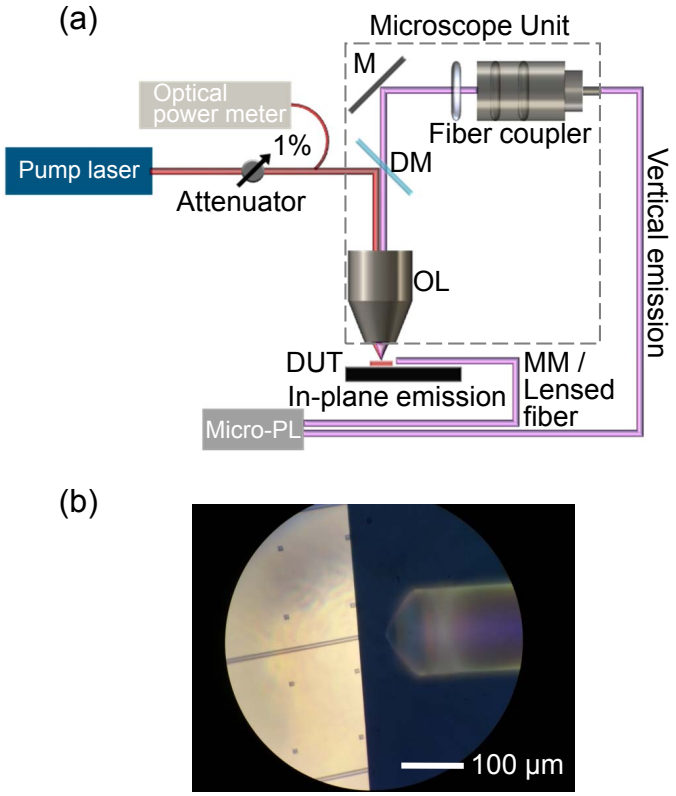

Figure 4.6: (a) Characterization setup for the hybrid VCL with an in-plane emission. [M: mirror, DM: dichroic mirror, OL: objective lens, Micro-PL: micro-photoluminescence setup, DUT: device under test, MM fiber: multi-mode fiber] (b) Microscope image of the cleaved end of a Si waveguide and a lensed fiber.

aligned it until obtaining a maximum output power. Figure 4.6(b) shows the lensed fiber in front of the end facet of the Si waveguide.

The position of a pump beam on top of the top DBR is indicated as white dotted circle in Fig. 4.7(a). To estimate the profile of a lasing mode, it is captured using an InGaAs camera after filtering the pump laser via a long pass filter. To obtain the profile of the pump beam, the pump beam is positioned on the flat Si layer and then captured. The captured images of the pump beam and the lasing mode are shown in Figs. 4.7(b, c), respectively. The e^{-2} diameters for the pump beam, d_{pump} and the transverse mode seen from the top, d_{mode} are 5.84 and 5.99 μm, respectively. In Appendix D, the procedure to obtain the beam waist is explained in detail. The measured light-in (L_{in}) versus light-out (L_{out}) curve (LL curve) is shown in Fig. 4.8(a). The light-in represents the power absorbed in the QWs and

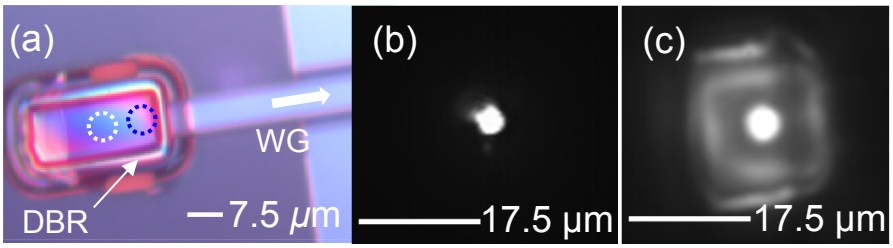

Figure 4.7: (a) Microscope image of the Si-integrated hybrid VCL seen from the top. IR images of (b) the pump beam and (b) the vertically-emitted lasing output.

separate confinement heterostructure (SCH) layers. It is estimated as:

$$L_{\mathrm{in}} = P_{\mathrm{m}} \times T_{\mathrm{a}} \times (\mathrm{d}_{mode}/\mathrm{d}_{pump})^2 \times A, \tag{4.1}$$

P_{m} is the incident pump power and A is the absorption efficiency, which was estimated as ∼30% by FDTD simulation. The LL curve clearly shows the lasing property with a threshold level of 29 μW. The converted threshold current, I_{th} can be estimated as:

$$I_{\mathrm{th}} = 29\,\mu\mathrm{W}/E_{980} \times q/f_{\mathrm{pump}}, \tag{4.2}$$

E_{980} is the photon energy at 980 nm and q is the elementary charge. The estimated I_{th} is then ∼1.1 mA which is similar to that of long-wavelength VCSELs, which have a similar mode size [39]. The in-plane output power can be enhanced by optimizing

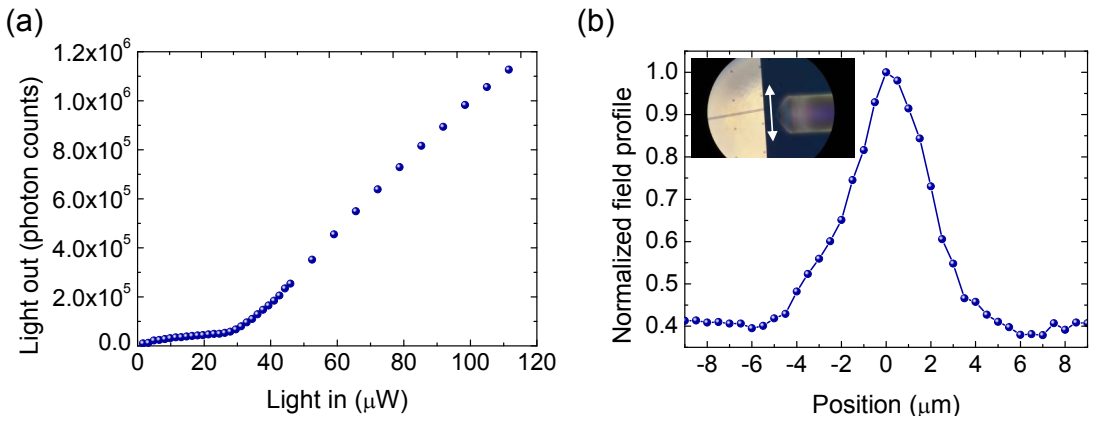

Figure 4.8: (a) In-plane light output from the Si waveguide as a function of absorbed input light. (b) Intensity profile of the in-plane output from the waveguide as a function of the waveguide position along the direction indicated as a double arrow. The relative position of '0' corresponds to the waveguide position.

the position of the tail of the excited transverse mode. Then the tail overlaps the one end of the Si waveguide [25]. To achieve this, the pump indicated as the white dotted circle in Fig. 4.7(a) should move to new position indicated as a blue dotted circle. However, the laser output power was maximum when the white dotted circle was pumped. This is attributed to the non-uniform DBR around the boundary, which results in lowering a reflectance and deteriorates the threshold condition of the laser. The non-uniform thickness of the DBR can be solved by using an etch-back process to form a DBR. The other possibility is to change the HCG and waveguide design so that the optimum lasing position is located in the center of a DBR [111]. Since the pumping position is away from the optimum position by ∼10 μm, the in-plane emission become much lower. The measured photon count is 1.15 $\times$ 10^6 in Fig. 4.8(a) and the corresponding continuous wave power is 0.013 μW. The in-plane emission is well confined in the Si waveguide as shown in Fig. 4.8(b). To characterize the in-plane emission, a lensed fiber is used and is swept along the direction indicated with a white double arrow in the inset of Fig. 4.8(b). The beam profile is maximized around the center position of the Si waveguide and the full width at half maximum (FWHM) of the measured beam profile is ∼5 μm.

4.3.4 Vertical cavity dispersion

Figure 4.9(a) shows the in-plane emission spectrum, which is measured by butt coupling between the Si waveguide and the MM fiber, at a pump power of $4P_{\mathrm{th}}$. In the inset of Fig. 4.9(a), the vertical emission spectra measured around P_{th} is shown as well. Around the threshold, three peaks with a wavelength spacing of 4.5 to 5.0 nm are observed in the vertical spectrum. Above the threshold, the longest wavelength mode overwhelms the other two peaks with a side-mode suppression ratio (SMSR) of 27.5 dB. It is noteworthy that, with such a SMSR, the spectral linewidth (FWHM) of the lasing peak is 0.66 nm. This linewidth is relatively broad when considering that the input pump level is far above the threshold level. Also, it is observed that the dominant peak is comprised of approximately 3 sub-peaks. If three sub-peaks exist within the broad peak, then the sub-mode distance is

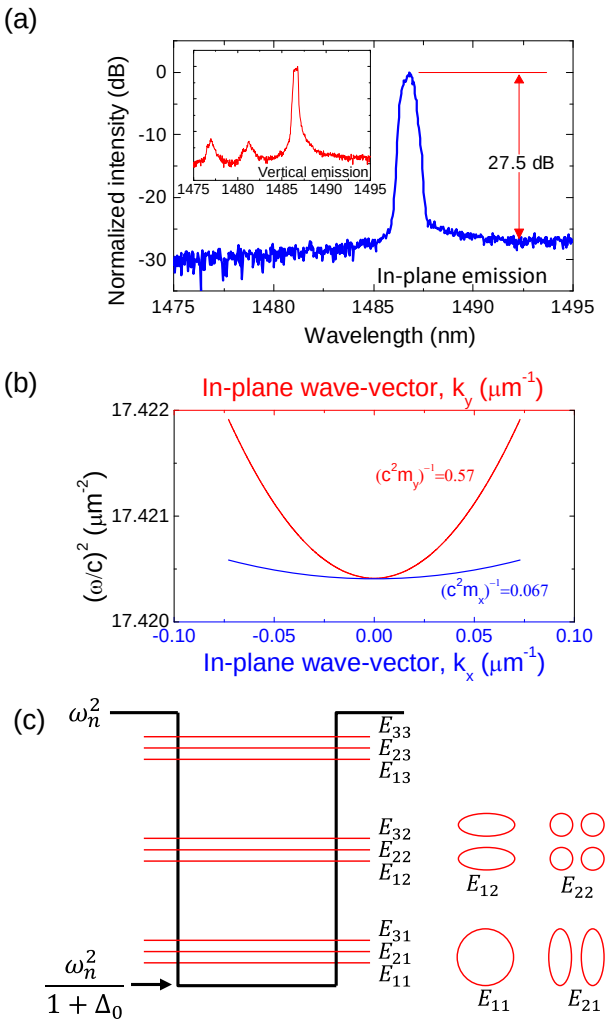

Figure 4.9: (a) Measured in-plane output spectrum at $4P_{\text{th}}$. The inset shows a vertical emission spectrum at P_{th}. (b) Angular-frequency square versus in-plane wave-vector. (c) Band-edge envelope approximation of a photonic quantum well, confined states E_{ij}, and corresponding transverse mode profiles.

approximately 0.2 to 0.3 nm. These closely arranged sub-peaks can be attributed to anisotropic dispersion property, which results from the bottom HCG. The vertical cavity resonance frequency (ω) depends on the transverse wave-vectors of k_x and k_y, which is determined by the transverse dispersions of the propagation within each mirror, as well as the multiple layers between the mirrors [109]. In the long-wavelength hybrid VCL structure, except for the bottom HCG, all the layers are uniform, which contributes to isotropic dispersion, while the HCG results in anisotropic one due to 1D structure. The highly anisotropic dispersion of the hybrid VCL is shown in Fig. 4.9(b). The band curvature along the x-direction, which

is perpendicular to grating bars, $\partial^2\omega^2/\partial {k_x}^2$ ($\equiv 1/m_x$) is 8.5 times smaller than that along the y-direction which is parallel to the grating bar, $\partial^2\omega^2/\partial {k_y}^2$ ($\equiv 1/m_y$). The definition of the band curvatures are found in [110], which is about photonic crystal heterostructures. For this optically-pumped laser, the outside of the pump region can be assumed as a lossy region because of the absorption loss in the QWs, which determines the transverse mode size. Then, the exponential decay of the transverse mode in the lossy region is considered as the decay in the barrier region of a quantum well. Therefore, to estimate the resonance frequency of the vertical cavity structure, it can be modeled as the band-edge frequencies of the gain and lossy region as shown in Fig. 4.9(c). Then, using the envelop approximation for photonic crystal heterostructure [110], angular frequencies of $\omega_{i,j}$, which correspond to confined transverse states of $E_{i,j}$, can be derived as

$$\omega_{ij}^2 = \frac{1}{1+\Delta_0}\left[\omega_n^2 + \frac{(a_i i\pi)^2}{2m_x L_x^2} + \frac{(b_j j\pi)^2}{2m_y L_y^2}\right] \qquad i,j = 1,2,3,\cdots . \tag{4.3}$$

where i and j are quantum numbers for x- and y-direction, respectively, and a_i and b_j are rational factors because of the finite barrier. As indicated in Fig. 4.9(c), the cut-off frequency and the barrier height are determined by angular frequency ω_n and Δ_0, respectively. Also, it is assumed that quantum well widths, L_x and L_y are determined by the d_{pump}. The estimated wavelength positions of the confined states $E_{i,j}$ are shown in Fig. 4.9(c) and explained the grouping of modes observed in Fig. 4.9(a). The corresponding transverse mode profiles are shown in Fig. 4.9(c) as well. The lasing peak should be a mixture of $E_{i,j}$. This result proves that the anisotropic dispersion in a HCG-based vertical cavity has significant influence on the vertical-cavity resonance frequency and transverse mode profile. Therefore, the HCG-based vertical cavity needs to be carefully considered when designing vertical cavity including a HCG mirror.

By employing HCG heterostructures along x- and y-direction, not only the band curvature, m_i but also the barrier height, Δ_0 can be controlled separately. This will provide cavity design flexibility, which allows for the transverse mode control of the VCL [111]. As mentioned above, this is the one way to control the lasing mode position as well.

4.4 High-speed Hybrid Vertical Cavity Laser

4.4.1 Hybrid mirrors for small mode volume

For a 1550 nm high-speed vertical cavity laser structure, two mirrors in the laser cavity should have the short energy penetration depth into the two mirrors which is added to the laser cavity length. The sum of the laser cavity length and the energy penetration depth is defined as the effective cavity length as discussed in Chapter 2. The energy penetration depth is related to the 3 dB bandwidth via the confinement factor, $\Gamma = \Gamma_z \Gamma_{xy}$, where Γ_z is the vertical confinement factor and Γ_{xy} is the transverse confinement factor. The confinement factor influence the intrinsic characteristic of the laser in terms of the relaxation oscillation frequency of ω_R as;

$$\omega_R = \left[\frac{\Gamma v_g a}{qV} \eta_i (\mathrm{I} - \mathrm{I}_{th}) \right]^{1/2}, \tag{4.4}$$

v_g is the group velocity, a is the differential gain, η_i is the injection efficiency, V is the active region volume, and I and I_{th} is the current and the threshold current. According to the Eq. 4.4, the larger the Γ, the higher ω_R. For the vertical cavity structure, the vertical confinement factor (Γ_z) is relevant to the energy penetration depth into the mirrors. Therefore, for the high-speed long-wavelength VCL, the mirrors should possess >99.5% reflectance as well as a short energy penetration depth.

Using a bottom HCG structure and a top dielectric DBR, a high-speed hybrid VCL is investigated with the goal of demonstrating a Si-integrated long-wavelength high-speed laser. The structure is basically the same as the in-plane laser as shown in Fig. 4.2(a). The primary difference is the top and bottom mirrors used for this high-speed vertical cavity structure. First, the bottom HCG, which is formed on a SOI wafer, is investigated to confirm that how thick low index layers above and below the HCG are needed to obtain high reflectivity. The low index above the HCG, which is introduced inside the vertical cavity, can influence the effective cavity length. Even though the thickness of the HCG is thin, if the HCG needs a thick low index layer, then it could degrade the vertical confinement factor. For the

low index layer below the HCG, it will determine how thick BOX layer is needed for a realistic SOI structure as well. Therefore, The thinner BOX layer may be better. Besides, for on-chip optical interconnects, a bottom HCG is required. It reduce the burden of integrating vertical cavity structure with a silicon photonics platform because the bottom HCG can route the vertically-amplified light laterally into a Si waveguide. Second, a top dielectric DBR mirror with a high index contrast (Δn) is formed using an etch-back process. The etch-back process is chosen to overcome the problem of the curved-edge DBR. Also, the dielectric DBR with 6 pairs of SiO_2/a-Si (Δn = 1.47) possesses a larger Δn when compared to the SiO_2/TiO_2 DBR (Δn = 0.85), which is used for the in-plane hybrid VCL; and hence, the SiO_2/a-Si DBR has a shorter energy penetration depth as discussed in Chapter 2. For reference, these dielectric DBRs have better performance in terms of the energy penetration depth when compared to the wafer-fused epitaxial AlGaAs/GaAs DBR (Δn = 0.49) [43]. Besides, they are physically thinner because of the higher index contrast.

The bottom HCG can be designed for TM- or TE-polarized incident light. The HCGs should be surrounded by low index materials in the above (region I) and the below (region II) HCGs, respectively, in order to obtain a high reflectance [50, 112]. The HCG reflector needs to have more than 99.5% [27]. For a Si-integrated hybrid VCL, the low index material in region II is buried oxide (BOX, n = 1.48). Region I can be air or SiO_2 [25, 40, 68, 106]. In the vertical cavity laser structure investigated in this work, there is a high-index III-V active layer above the air gap. If the air gap thickness is not sufficient, there will be an evanescent coupling to the III-V layer which will drop the surface-normal reflectance [73]. At the same time, the air gap should be as thin as possible to minimize the effective cavity length ($L_{eff,e}$), and hence increase Γ_z of the vertical cavity.

First, to verify the evanescent field around the HCGs, the field profiles of a TM and TE HCG are obtained and shown in Fig. 4.10. The design parameters for the 1550-nm HCGs are shown in Table 4.1. The incident region is assumed to be filled with air and the exit region is filled with a half-infinite BOX layer. The 2D profiles show the total field amplitude, and the 1D profiles show the decomposed

Table 4.1: TM and TE HGC parameters (λ = 1550 nm).

Type	Period (Λ, nm)	Grating thickness (t_g, nm)	Width (Si bar) (fΛ , nm)
TM	703.42	492	323.0
TE	1000.0	238	322.0

field amplitude at x = 0. In region II, there is no noticeable propagating harmonic because of its small amplitude, which indicates that the two HCGs perform as a highly reflective mirror at 1550 nm. In region I of the TM and TE HCG, the total field amplitude only resulted from the 0-th harmonic and is close to 2. Near the upper and lower HCG boundaries, there are evanescent fields that extended mainly through the 1-st order into the low index layers as shown in Figs. 4.10(b, d), respectively. The higher order harmonics (> 0-th order) are evanescent field

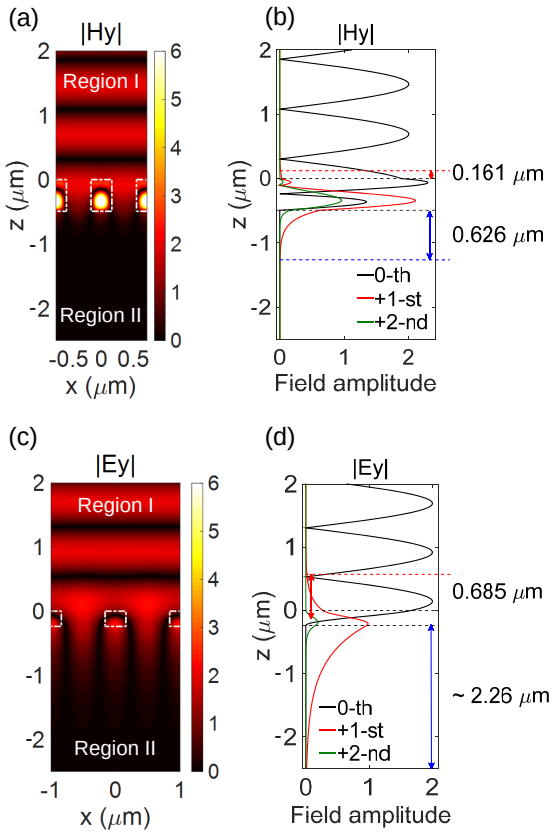

Figure 4.10: (a, c) 2D amplitude field profiles of periodic TM and TE HCGs for the normal incident plane wave from the top and (b, d) corresponding decomposed 1D field amplitude profiles at x = 0.

along the surface-normal direction because the period of the HCG (Λ) is less than the incident wavelength (λ). Then, the propagation constant of the higher orders along the vertical direction become a imaginary and it is given by,

$$\mathrm{k_{l,zm}} = -\mathrm{j}[(m\frac{2\pi}{\Lambda})^2 - (\mathrm{n_l}\frac{2\pi}{\lambda})^2]^{(1/2)}, \quad \left|m\frac{2\pi}{\Lambda}\right| > \mathrm{n_l}\frac{2\pi}{\lambda}, \quad \mathrm{l} = \mathrm{I}, \mathrm{II}. \tag{4.5}$$

where $m = \pm 1, \pm 2, \cdots$, and $\mathrm{k_0}$ is $2\pi/\lambda$. Then, the field component of the higher orders become an evanescent field and it is proportional to

$$\mathrm{E_z} \propto \begin{cases} \exp(-\mathrm{jk_{zm}z}) & \mathrm{z} > 0 \quad (\text{region I}) \\ \exp(+\mathrm{jk_{zm}(z-d)}) & \mathrm{z} < -\mathrm{d} \quad (\text{region II}), \end{cases}$$

, where 'd' is the HCG thickness. TE HCGs usually have a larger period than TM HCGs, even though the two HCG are designed for the same target wavelength [73]. According to Eq. 4.5, the imaginary $\mathrm{k_{l,zm}}$ is smaller for the TE HCG because of the larger Λ. Therefore, for the same higher order harmonic, the TE HCG possesses a longer evanescent tail [73]. In region I of the air layer and in region II of the BOX layer, the evanescent tail length of the TE HCG is 3.9 and 3.6 times longer than that of the TM HCG, respectively.

To confirm the evanescent field effect on the reflectance, a half-infinite InP ($\mathrm{n_{InP}} = 3.1661$) layer is approached to each HGC from the top by assuming that the BOX layer is a half infinite as shown in Fig. 4.11(a). The reflectance spectra observed from the InP is shown in Fig. 4.11(b). To obtain 99.99% reflectance, the air gap thickness should be thicker than 158 nm for the TM HCG and 744 nm for the TE HCG. The minimum air gap thicknesses of the TM HCG to obtain 99.9% reflectance is 4.7 times thinner when compared to the TE HCG. If the air gap is not thick enough, the evanescent tail couples to the top InP layer and then the the reflectance become lower. Therefore, a HCG designed for TM-polarized light allows the thickness of air gap to be as thin as 0.1λ. For comparison, the thickness of this low-index gap layer in previous HCG-based VCSELs ranges from 0.85λ to 1.25λ [27, 28]. When a low-refractive index material such as SiO_2 is used for the gap layer [28, 68, 106], then the TM HCG has advantages in terms of heat dissipation because of the thinner layer.

When considering the full structure of a SOI wafer, it is necessary to consider a finite BOX layer on top of a thick Si substrate. As shown in Fig. 4.11(c), the bottom Si layer is added. With the fixed air gap thicknesses, which gives 99.99% reflectance for the TM and TE HCG in Fig. 4.11(b), the thickness of BOX layer is reduced, and the bottom Si layer is accordingly approached to the HCGs from the bottom. The extended evanescent field in the exit region is starting to interact with the bottom Si layer, which will influence the reflectance seen from the top InP layer. As shown in Fig. 4.11(d), the reflectance spectra as a function of the BOX thickness shows the effect of the extended evanescent field in the exit region on the reflectance as well. The longer the evanescent tail, the thicker the BOX layer needs to be in order to get 99.99% reflectance. The TM HCG needs a 1μm BOX layer, while for the TE HCG, while the BOX layer in the TE HCG should be more than 3.5 μm. On the whole, the TM HCG design will be beneficial in terms of the optical confinement along the vertical direction and the physical volume of the SOI platform.

To further squeeze the mode volume, the energy penetration depth into the

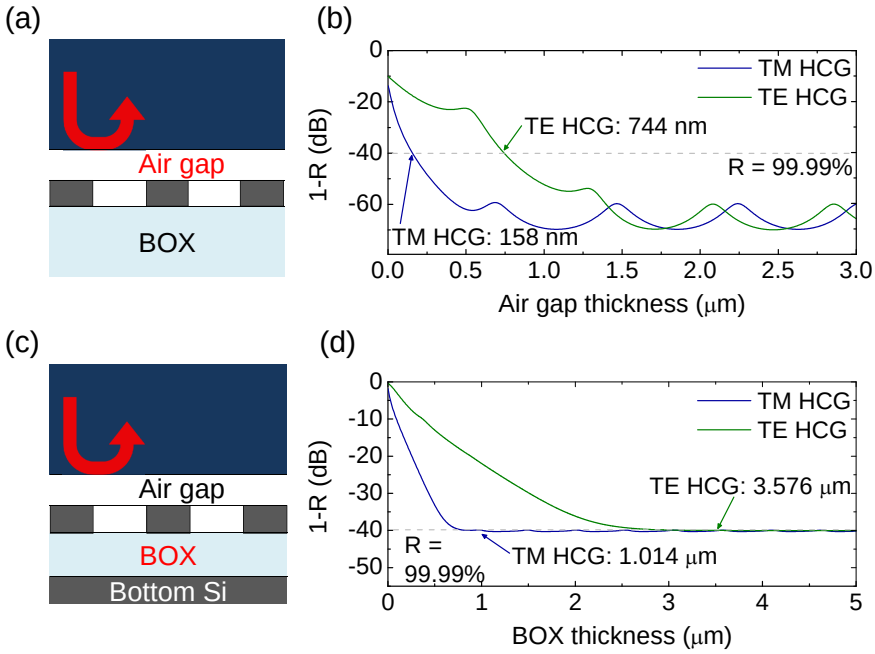

Figure 4.11: (a) Calculated (1-R) of representative TM and TE HCGs seen from half-infinite InP layer as a function of the air gap thickness with a lower half-infinite BOX layer and (b) as a function of the BOX thickness with the fixed air gap which guarantees 99.99% reflectance and a lower half-infinite Si layer.

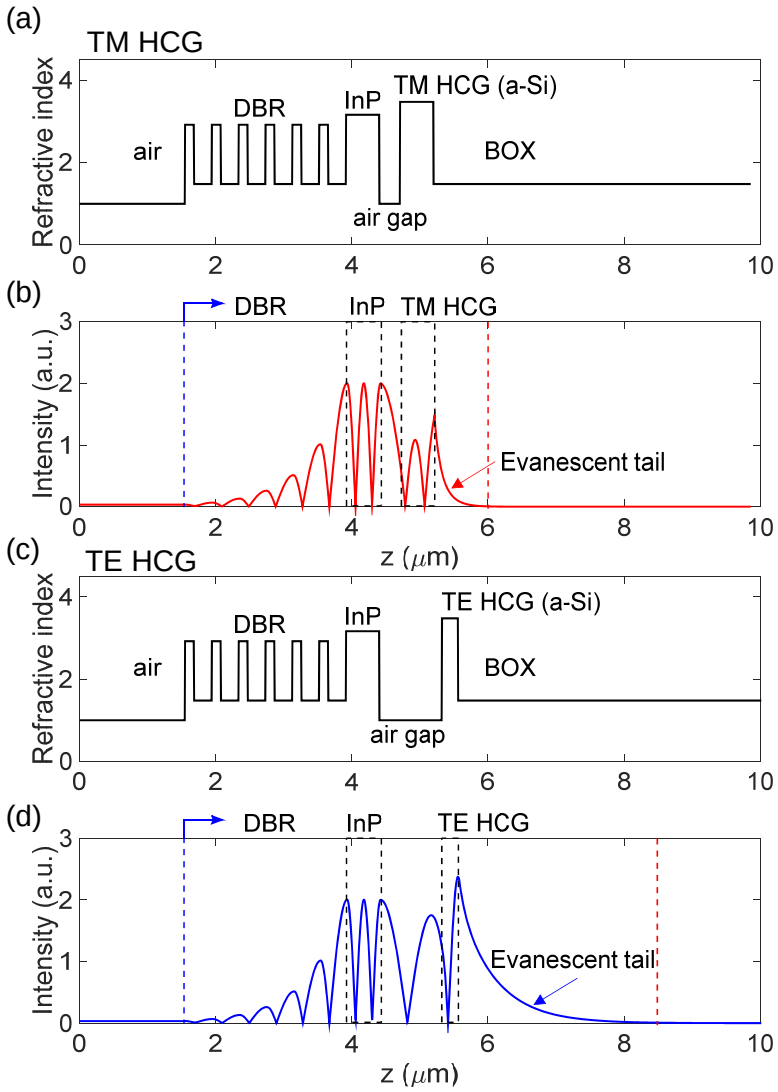

Figure 4.12: Refractive index profile of hybrid VCL structures employing (a) a bottom TM HCG reflector and (c) a bottom TE HCG reflector. Field intensity distribution of the hybrid VCLs with (b) the TM HCG structure and (d) the TE HCG structure.

top mirror is reduced by using a dielectric DBR. For the top DBR, SiO_2 with a refractive index of 1.45 and a-Si with a refractive index of 2.92 are used, which has a high index contrast of 1.47. This index contrast is larger than that of the 7 pair SiO_2/TiO_2 DBR, which has $\Delta n = 0.85$, and hence; it is expected to squeeze the energy penetration depth further.

The effect of the top dielectric DBR and the bottom TM HCG mirror on the hybrid VCL structure is investigated in terms of the vertical confinement factor. As mentioned above, the TM HCG requires thinner air gap and BOX layer when

compared to the TE HCG. It needs to confirm that the thinner layers can contribute to squeeze the vertical mode volume. For this purpose, the two hybrid VCL with the same structure, except for the bottom HCG and the air gap thickness, are numerically investigated (see Appendix E for the parameters). Then, the vertical confinement factors are calculated. The top mirror is a 6 pair SiO_2/a-Si DBR and a single InP layer is used for the sake of simplicity. The thickness of the InP layer is the same. Inside the InP layer, it is assumed that quantum wells (QWs) are positioned in the middle, and the position of QWs is used to calculate the vertical confinement factors. The incident and exit medium are air and BOX layer, respectively, with half-infinite thickness. The top DBR for the two lasers are located at the same position on the z-axis to compared the entire field distribution along the z-axis.

Figure 4.12 shows the refractive index profile and the field distribution of hybrid VCL structures, which employ the bottom TM HCG and TE HCG. The TM and TE HCG thicknesses are 492 and 238 nm, respectively, and the corresponding air gap thicknesses are 303.8 and 919.8 nm. The TM HCG is 2 times thicker than the TE HGC, while it needs 3 times thinner air gap. Therefore, the total thickness of the TM and TE HCG including the air gap are 795.8 and 1157.8 nm, respectively. The evanescent tails, which are extended into the BOX layer, are clearly shown in Figs. 4.12(b, d). The evanescent tail for the hybrid VCL with the TM mirror decays fast and, after a distance on the z-axis of 6 μm indicated as a dashed red line in Fig. 4.12(b), the tail almost become 0. For the TE HCG structure, the evanescent tail penetrates far into the BOX up to 8 μm on the z-axis. The distance of field distribution from the DBR indicated as a dashed blue line to the end of the evanescent tail is shorter when the TM HCG is employed. The TM HCG curtails the distance by $\sim$2 μm. The calculated vertical confinement factor for the TM HCG structure is 9.87% and, for the TE HCG structure, it shows 9.06%. The TM HCG structure shows a slight higher confinement. This difference result from the evanescent tails above and below the HCG layer. Therefore, by using TM HCG design, it is possible to obtain a higher vertical confinement factor as well as a physically thinner vertical cavity structure.

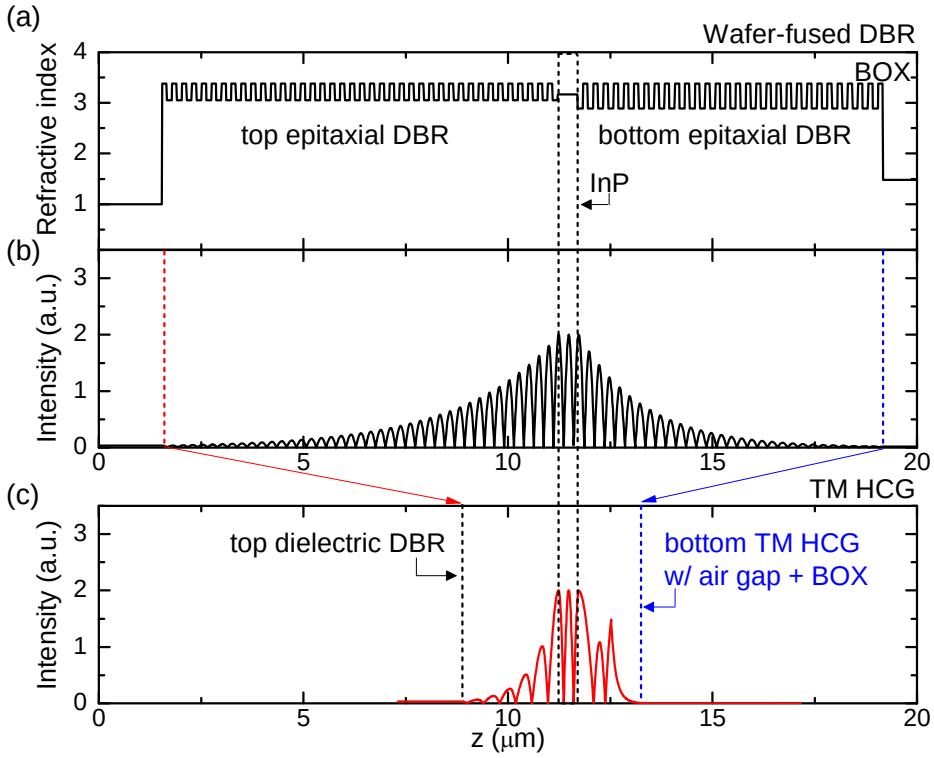

Figure 4.13: (a) Refractive index profile of a VCSEL with double wafer-fused AlGaAs/GaAs DBRs and (b) its field intensity distribution. (c) The field intensity distribution of the hybrid VCLs with the TM HCG, which plotted in the same z-axis of the VCSEL. The black and blue dotted lines indicate the top and bottom mirror region. For the bottom TM HCG region, it includes the air gap and the BOX region where the evanescent tail is extended.

For reference, the field profile of a double wafer-fused AlGaAs/GaAs DBR VCSEL is illustrated [43]. For a 1.55 μm long-wavelength DBR, the double wafer-fused AlGaAs/GaAs DBRs are used because they have a higher index contrast (Δn$\approx$0.5) and a better thermal conductivity compared to the lattice-matched InGaAsP/InP DBR (Δn$\approx$0.2) [30, 31]. Figures 4.13(a, b) show the refractive index profile and field distribution of the epitaxial DBR VCSEL (see Appendix E for the parameters). The top and bottom DBRs possess 40 and 30 pairs, respectively, to have the similar reflectance condition to the two hybrid VCLs. The hybrid VCL with the TM HCG is shown together in order to compare with the double wafer-fused AlGaAs/GaAs DBR VCSEL. It is evident that the field intensity is distributed along the top and bottom epitaxial DBR with a substantial portion, which leads to the vertical confinement factor as low as 2.95%. As shown in Fig.

4.13(c), the hybrid VCL with the 6 pair dielectric DBR and the TM HCG is plotted on the same z-axis for comparison purpose. The top dielectric DBR compresses the field distribution inside the 6 pair DBR, which is narrower than the distribution inside the epitaxial DBRs. The dielectric DBR curtails the length of the field distribution by 7.3 μm. Besides, the bottom HCG including the air gap and the BOX layer where the evanescent field spreads over, is much thinner than the bottom epitaxial DBR. It decreases the field distribution by 5.9 μm. Importantly, the total thickness of the HCG is even thinner than the top dielectric DBR. These two mirrors contribute to the high confinement factor of the 9.87%. It should be noted that the confinement factor of the hybrid VCL with a TM HCG could be enhanced further by optimizing the HCG parameter, considering the entire vertical cavity structure and keeping the HCG thickness.

4.4.2 Experimental and characterization result

Using the two hybrid mirrors, a VCL is fabricated. The fabrication processes used here are explained in the previous section, except the top DBR is 6 pair SiO_2/a-Si which is formed using an etch-back process, not the lift-off process. Figure 4.14 shows the fabricated hybrid VCLs on a SOI wafer. As shown in Fig. 4.14(a) it is possible to integrate many light sources on the SOI platform. As shown in Figs. 4.14(b, c), the top DBR is well defined with a flat surface on the entire area, even at the boundary.

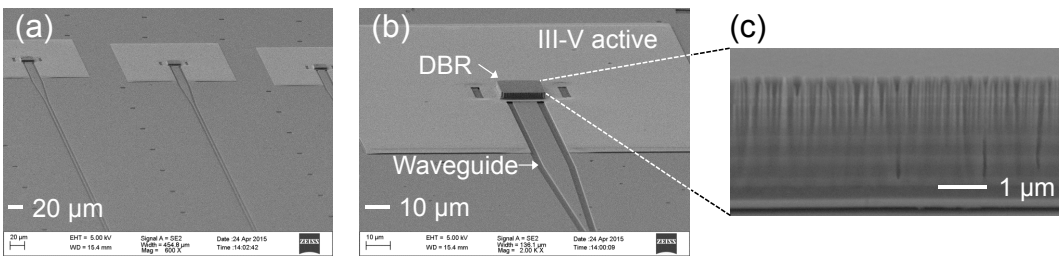

Figure 4.14: SEM images of the fabricated hybrid VCLs. (a) The SEM image shows the fabricated hybrid VCLs using CMOS-compatible process which can enhance the integration density of the light source on a SOI platform. (b) The zoomed-in SEM image shows the structure of Si-integrated hybrid VCL. (c) Cross-section SEM image of the DBR fabricated by using an etch-back process.

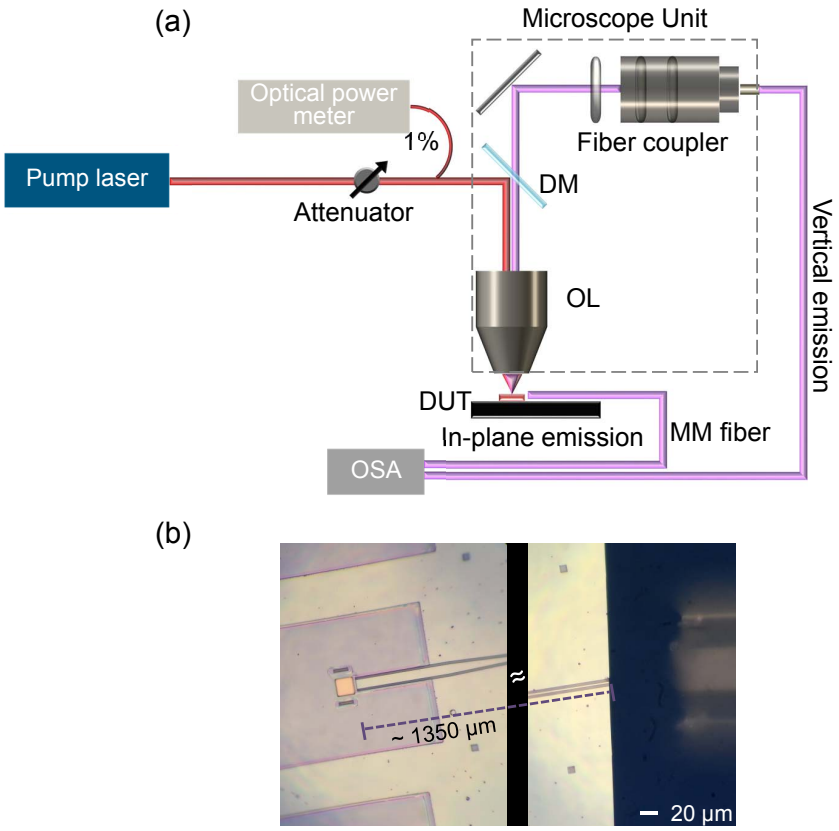

Figure 4.15: (a) Static characterization setup for the high-speed hybrid VCL. (b) Microscope image of the fabricated hybrid VCL seen from the top and the multi-mode (MM) fiber near the end of the Si waveguide for the in-plane characterization. [MM fiber: multi-mode fiber, OSA: optical spectrum analyzer]

To characterize the static property of the fabricated VCL, a microscope setup is used and is shown in Fig. 4.15(a). This is the same setup taht was used for the in-plane hybrid VCL, except that the optical spectrum analyzer (OSA) is used instead of the micro-photoluminescence setup. The un-cooled hybrid VCL is optically-pumped using a 980 nm pump laser in pulsed operation mode with a 10% duty cycle (f_{pmp}) and a 5 MHz repetition rate. The pulsed operation is needed because of the heat problem. The transmitted power of the microscope setup, T_a is between 10.5 and 13.4%, depending on the optical alignment of the setup. The vertical output through the top DBR is collected by the same objective lens, coupled to a fiber coupler, and sent to an optical spectrum analyzer (OSA). The in-plane output is collected by a cleaved multi-mode (MM) fiber directly coupled to the end of the Si waveguide as shown in Fig. 4.15(b). The light input power

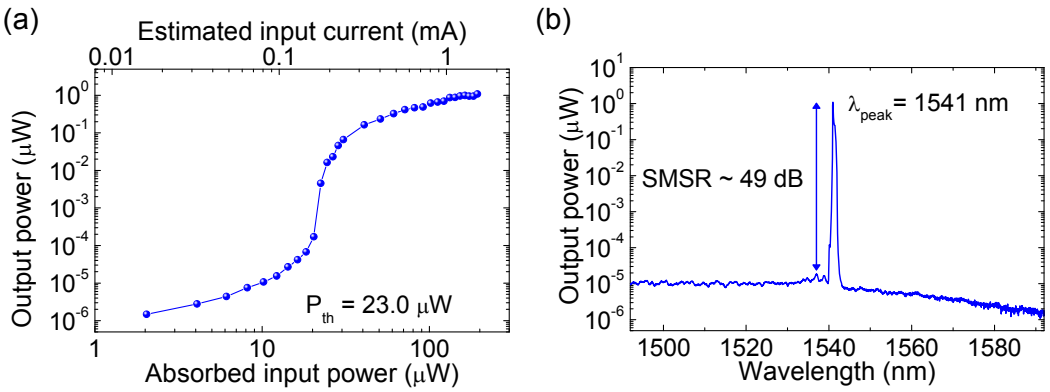

Figure 4.16: (a) Light-in versus vertical light-out curve for the high-speed VCL at RT in pulsed operation. (b) Representative lasing spectrum at $8.4P_{th}$.

(P_{in}) is estimated as $P_{in} = P_{pump} \times T_a \times \eta_{abs}$, where P_{pump} is the power level of the pump laser and η_{abs} is the absorption efficiency, which is the fraction of absorbed power in the QWs and barrier layers. The estimated absorption efficiency of η_{abs} using the FDTD method is 9.1%. For the CW estimation, the current for a continuous-wave case (I) is estimated as $I = P_{in} \times q/E_{980}/f_{pmp}$, where E_{980} is the photon energy at 980 nm and q is the elementary charge.

Figure 4.16(a) shows the vertical output power as a function of input power (P_{in}). The threshold input power (P_{th}) is 23.0 μW and the corresponding threshold current is estimated to 0.18 $\pm$ 0.02 mA. As shown in Fig. 4.16(b), the lasing wavelength is 1541 nm and the side-mode suppression ratio (SMSR) is about 49 dB. The in-plane static results are shown in Fig. 4.17 as well. The representative spectrum indicates that the lasing wavelength is 1540.4 nm and the SMSR is about 33 dB, which can

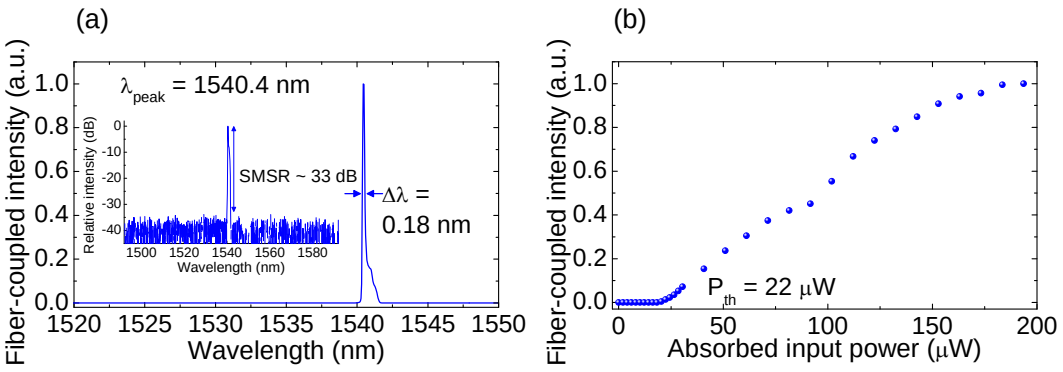

Figure 4.17: (a) Representative lasing spectrum and (b) Light-in versus in-plane light-out curve at RT in pulsed operation.

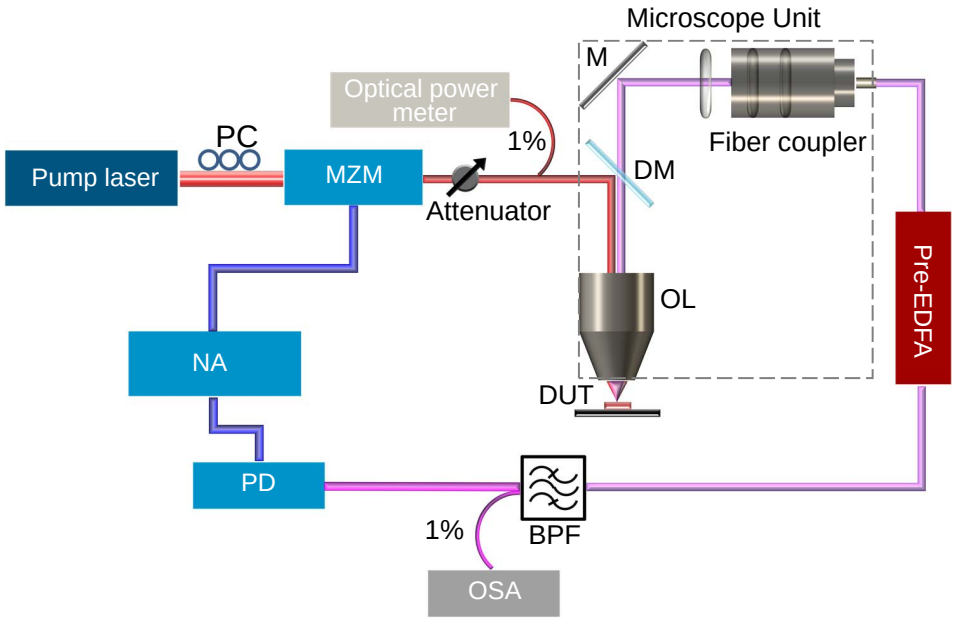

Figure 4.18: (a) Schematic illustration of the measurement setup for the dynamic characterization. [PC: polarization controller, MZM: Mach-Zehnder modulator, EDFA: erbium-doped fiber amplifier, BPF: band pass filter, NA: network analyzer, PD: photo-detector]

be attributed to the loss at the boundary of the HCG and the Si waveguide. The threshold input power (P_{th}) is 22.0 μW. The slightly different observed threshold and lasing wavelength between the vertical and the in-plane results can be explained by the different alignment of the microscope setup for each measurement.

The setup used for characterizing the small-signal frequency responses of the hybrid VCL is shown in Fig. 4.18. The 980 nm pump laser is operated with a 4% duty cycle and a 5 MHz repetition rate. The laser output is sent to a Mach-Zehnder modulator (MZM) controlled by a network analyzer with -5 dBm input power to the modulator. The modulated output is delivered to the hybrid VCL via the microscope setup. The vertical output power is collected by the objective lens (OL) and then fed into a fiber coupler. The fiber coupled output is amplified by an erbium-doped fiber amplifier (EDFA). Then, after passing through a band pass filter (BPF), the amplified noise is filtered out and the amplified laser output is detected by a high-speed photo-detector [1]connected to the network analyzer.

[1]up to 40 GHz

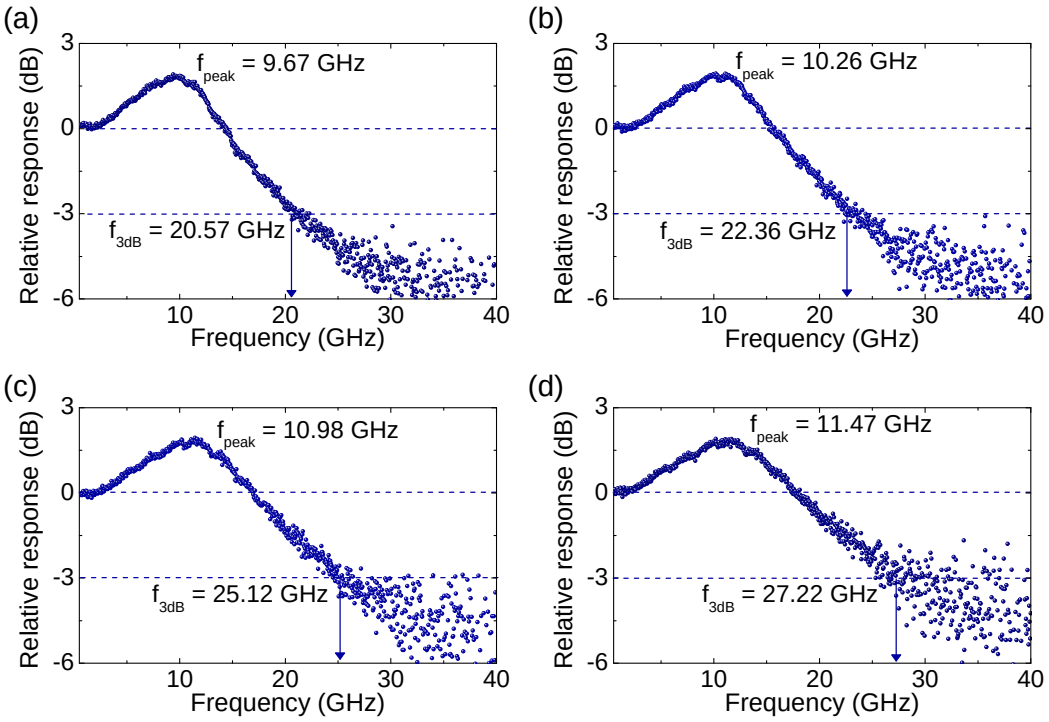

Figure 4.19: Measured small-signal frequency response spectra at absorbed input powers of (a) 24.45, (b) 27.51, (c) 31.59, and (d) 34.65 μW.

Figures 4.19(a-d) shows the measured frequency responses at the absorbed input powers of (a) 24.45, (b) 27.51, (c) 31.59, and (d) 34.65 μW, respectively, and the corresponding 3 dB frequencies are (a) 20.57, (b) 22.36, (c) 25.12, and (d) 27.22 GHz. The corresponding estimated currents are (a) 0.48, (b) 0.54, (c) 0.62, and (d) 0.68 ($\pm$ 0.08) mA . The peak frequencies for each frequency response are (a) 9.67, (b) 10.26, (c) 10.98, and (d) 11.47 GHz. To compare the the 3 dB frequency and the peak frequency, D-factor and modulation current efficiency factor (MCEF), which are the slopes of the f_{peak} and f_{3dB} curves as the function of $(I\text{-}I_{\mathrm{th}})^2$, respectively, are shown in Fig. 4.20. The estimated MCEF and D-factor are 42.1 GHz/mA$^{1/2}$ and 11.2 GHz/mA$^{1/2}$, respectively. The MCEF is 3-times larger than that of the 850 nm VCSEL in [95] and is 2/3 of the PhC laser in [94], which proves that the the 3 dB frequency is enhanced by the squeezed mode volume along the vertical direction. However, the D-factor with 11.2 GHz/mA$^{1/2}$ is similar to the 850 nm VCSEL. In case of the response with the small damping, the f_{3dB} is approximately 1.55 times as large as the f_R [38], so the large difference between

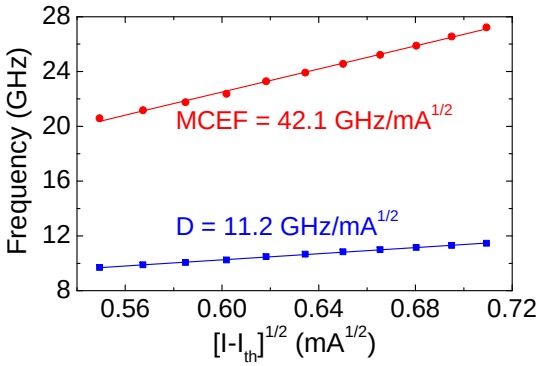

Figure 4.20: (a) Estimated MCEF (3 dB frequency) and D factor (peak frequency), respectively.

the MCEF and D-factor cannot be explained only with the squeezed mode volume. It can be explained by using an internal optical feedback which can enhance the 3 dB bandwidth and can suppress the peak response at the same time [113, 114]. The suppressed peak response will change the peak intensity frequency and it will move towards a shorter frequency. As a result, the difference between the two frequencies becomes widen and results in the ∼4-times slope difference. In a short-wavelength VCSEL, a monolithically-integrated feedback structure was reported [113, 114]. The VCSEL is comprised of a 26 pair AlGaAs/AlGaAs top DBR and a 41.5 pair AlGaAs/AlGaAs bottom DBR with a 1λ cavity. In contrary to the bulky VCSEL structure, this 1λ hybrid VCL consists of the 6 pair thin top dielectric DBR and <500 nm bottom mirrors. The bottom HCG contributes to reduce the overall volume of the long-wave VCL. Besides, as mentioned in the previous section, the transverse dispersion can be controlled by tailoring the HCG design [111]; and hence, the group index along the x-direction can be enhanced further, which can reduce the length of the lateral feedback channel as short as 20 μm [114]. Therefore, the hybrid VCL structure can be a compact integrated feedback laser with design flexibility. The analysis of the internal feedback effect on the 3 dB frequency response for the hybrid VCL is now in progress.

4.5 Summary

In summary, the optically-pumped Si-integrated long-wavelength VCLs have been experimentally demonstrated using the CMOS-compatible processes. First, by using the bottom HCG as the bottom mirror of the hybrid vertical cavity, the feasibility of the in-plane emission into the Si waveguide was proven. The in-plane hybrid VCLs integrated on a SOI can be used as light sources for on-chip optical interconnects. Second, to verify the possibility of high-speed operations at long wavelength, i.e., 1550 nm, with the vertical cavity structure, the vertical cavity with the SiO_2/a-Si top dielectric DBR and the bottom TM-HCG has been suggested to squeeze the vertical mode volume. The high-speed hybrid VCL was fabricated and characterized. It showed the 3 dB frequency of 27.2 GHz with the damped peak intensity of ∼2 dB, which attributed to both the small mode volume and the internal optical feedback. The estimated MCEF factor of 42.1 GHz/mA$^{1/2}$ was obtained which is 3 times higher than that of the 850 nm VCSEL. This high-speed VCL design can be adopted for in-plane emission and inherit the high-speed property by tailoring the bottom HCG design.

"If you thought that science was certain - well, that is just an error on your part."

— Richard Feynman

5 Hybrid Grating Reflector

Contents

5.1 Introduction

In this chapter, a new type of mirror based on a grating structure is rigorously investigated and experimentally demonstrated, which is suggested in [55, 115, 116]. Hybrid grating (HG) reflectors with a high-refractive-index membrane directly integrated on the grating structure can work as a high broadband reflector with an even broader wavelength range than the high contrast gratings (HCGs). It is well-known that the HCGs should be surrounded by low-refractive-index materials in the upper region (region I) and the lower region (region II), respectively [50,112,117]. Otherwise, higher reflected and transmitted diffraction orders are excited and the

excited off-normal orders will deteriorate the diffraction efficiency of the 0-th or the surface-normal diffraction order [53]. In particular, for the vertical cavity laser (VCL) applications, the surface normal reflectance needs higher than 99.5% [27,105]. However, if the HCG is covered with a high index material, then the surface-normal reflectance will be decreased to $< 95\%$, which cannot be used as a mirror for VCLs.

The new type of mirror, the HG reflector, is not constrained to the low index requirement needed for the HCG [55]. Even though the high-index layer above the grating structure (region I′) can excite higher reflected diffraction orders, the off-normal diffraction orders can escape back to region I through the interaction between the cap layer and the bottom grating. The cap layer with a proper index can excite the '0-th order' with the highest diffraction efficiency which introduces Fabry-Perot (FP) resonance as well as $\pm$1-st diffraction orders which is involved in guided-mode resonances (GMRs) [118]. Then, the off-normal orders experience multiple diffraction processes, while propagating inside the cap layer. Among the diffracted orders, the 'surface-normal orders' leak out and the off-normal orders propagate along the cap until they have completely leaked out fully. Therefore, the off-normal orders can gradually leak out through each diffraction process. If the '0-th order' is *in phase* with the 'surface-normal orders' which are initiated from the $\pm$1-st order, then the incident field will be reflected with a reflectivity of $\sim$1.

The cap layer of the HG reflector possesses an active material; hence, it can be beneficial for the Si-photonics light sources. Now that the active layer has contacted with the bottom Si layer, the heat generated inside the active layer can be efficiently dissipated through the Si layer. Not only that, the HG reflector can support the in-plane emission as well.

5.2 Numerical Investigation of HG Reflector

The main difference between a HCG and a HG reflector is whether there is a high-refractive index layer on top of the grating structure. This is shown in Fig. 5.1(a, b), respectively. The HCG and the bottom grating part of the HG can be transferred to the top Si layer of a silicon-on-insulator (SOI) platform. The main

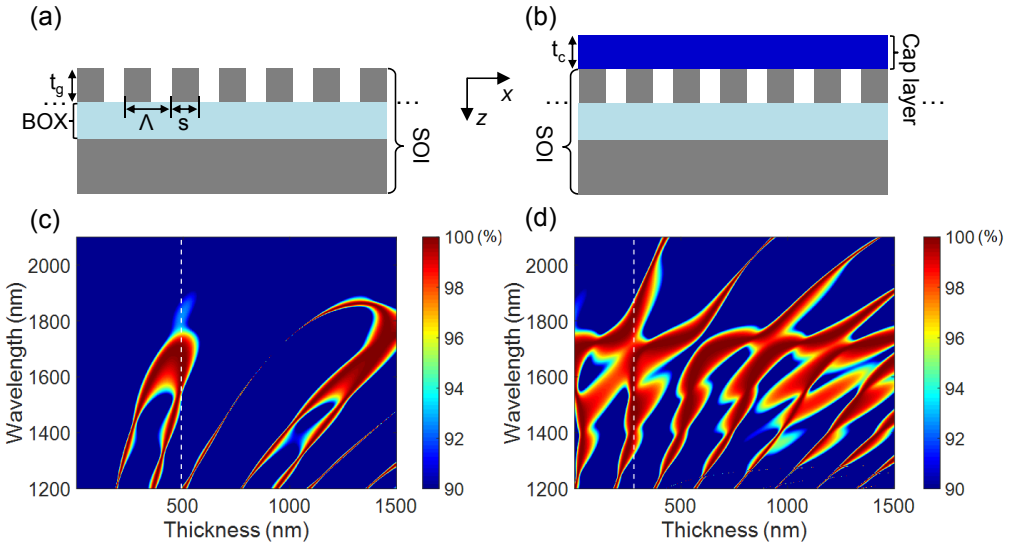

Figure 5.1: Schematic illustrations of (a) HCG and (b) HG reflectors and corresponding reflectance contours as varying the thickness of grating (t_g) of the HCG and cap layer thickness (t_c) of the HG with a t_g of 492 nm.

parameters for the HCG and the bottom grating which will determine the optical properties are period (Λ), width (s), and thickness (t_g). In addition to those grating parameters, for the HG reflector, there is an additional parameter which is the thickness of the cap layer (t_c) with a refractive index of n_c. Figures 5.1(c, d) show the reflectance contour plots of a TM HCG and a TM HG reflector, respectively, as a function of t_g and t_c in a wavelength range from 1200 to 2100 nm. The parameters used in the simulations are shown in Table 5.1 with the refractive index information. The white dashed lines in the contours indicate the thickness where the broadband reflectance spectra were obtained. With a grating thickness of 492 nm, the HCG

Table 5.1: HCG and HG parameters.

	Period (Λ, nm)	Width (s, nm) (n_{Si} = 3.477)	Grating thickness (t_g, nm)	Cap thickness (t_c, nm) ($n_{InGaAlAs}$ = 3.583)
Incident			air (n_{air} = 1)	
HCG	720	360	492	-
HG	720	360	492	279
Exit			BOX (n_{BOX} = 1.48)	

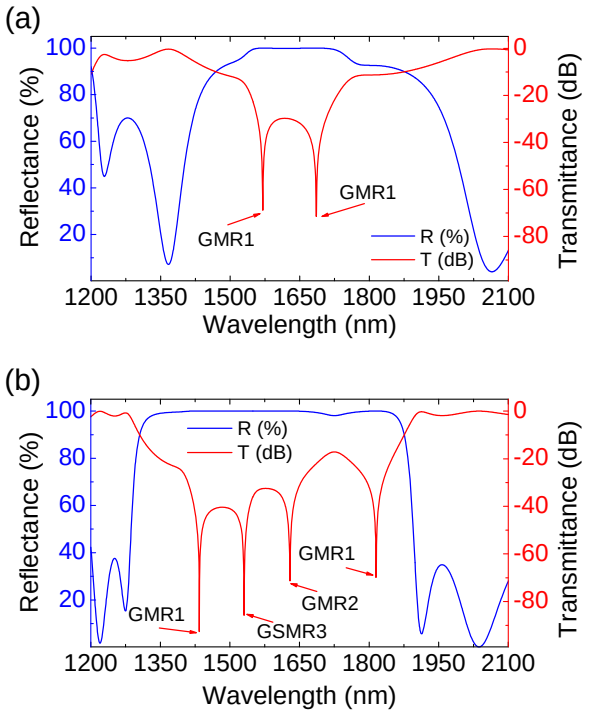

Figure 5.2: Reflectance and transmittance spectra of (a) the HCG with a grating thickness of 492 nm and (b) HG reflectors with a cap layer thickness of 279 nm indicated as the white dashed lines in Fig. (5.1c-d), respectively.

shows the broadest reflectance spectrum. Using the same grating parameters, but covering the grating with a high-index membrane with a thickness of 279 nm shows the broadest reflectance. The index of the cap layer is even higher than that of the Si grating bar. Figure 5.2 shows the reflectance and transmittance spectra for the HCG and HG reflector with the thickness indicated by the white dashed line Figs. 5.1(c, d), respectively. The HCG shows the two GMRs and the HG shows four GMRs. The closely arranged three GMRs contribute to the broader bandwidth. Even though the bottom grating of the HG reflector is designed with the same parameters as the HCG and is covered with the high-index cap layer with the finite thickness, it shows the broader stopband. The bandwidths for the HCG with $>$ 99% reflectance are 187 nm and 445 nm, respectively.

5.2.1 Polarization dependent reflectance

A HG reflector consists of an unpatterned structure and 1D bottom grating structure. The high reflectivity comes from the interaction between the cap and the bottom

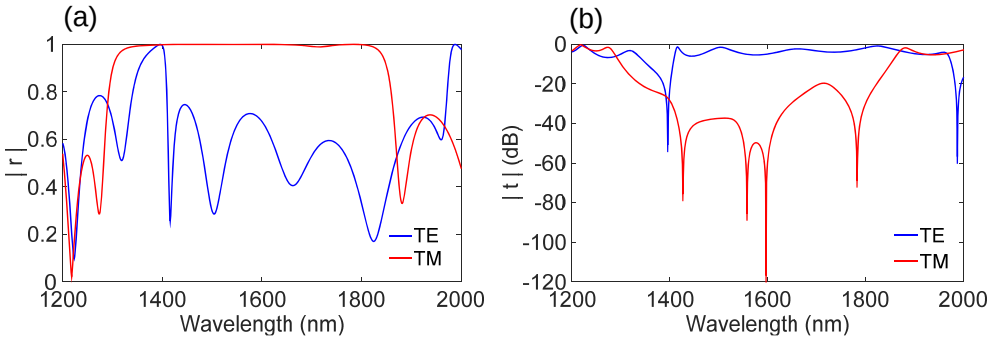

Figure 5.3: Calculated (a) reflectivity in linear scale and (b) transmissivity in dB scale of a TM HG reflector as a function of wavelength for TM- and TE-polarized normal incident plane wave.

grating. If the cap layer is linear, homogeneous and isotropic material, it will not depend on the polarization of an incident light. In contrary, the bottom grating is structurally anisotropic and it will cause the polarization dependency. If the bottom grating of the HG reflector is designed for either TE- or TM-polarized light, then it can selectively reflect TE- or TM-polarized light with a high reflectivity in a broad wavelength range. Therefore, the polarization sensitivity of the HG reflector comes from the bottom grating. As shown Fig. 5.3, the reflectivity spectra of the TM HG reflector for the TE- and TM-incident plane wave show a reflectivity difference of 0.34 at 1550 nm. This difference can stop polarization-mode hopping similarly to HCG.

5.2.2 Heterogeneously-integrated mirror

For long-wavelength VCL applications, from epitaxial DBRs to HCG reflectors, diverse kinds of mirrors are introduced. As a new type of mirror, the HG reflector will be an attractive bottom mirror because 1) the cap layer can include an active material that can be heterogeneously integrated on a SOI platform and 2) the HG reflector makes it possible for VCLs to emit light into an in-plane waveguide as the HCGs do [25, 40]. When considering a VCL with an in-plane emission, it is necessary to use a bottom grating mirror on a SOI platform. For the HCG bottom mirror, it is necessary to introduce a low-index gap above the bottom HCG to obtain high reflectance. Otherwise, the surface-normal reflectance will be dropped below 99.5% and then it cannot be used for the mirror. Low index materials such as BCB,

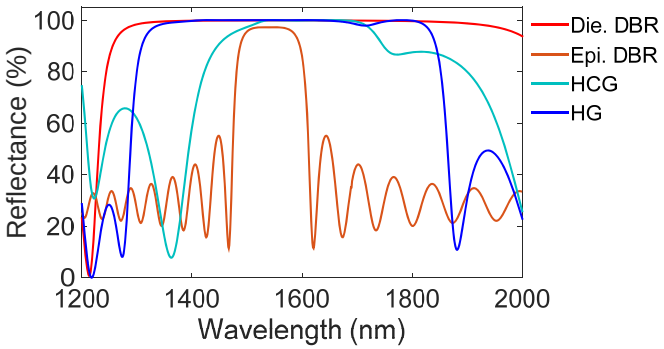

Figure 5.4: Calculated reflectance spectra for LW mirrors: dielectric DBR, epitaxial DBR, TM HCG, and TM HG mirrors.

SiO_2 or air should be introduced and on top of these layers an III-V active layer is positioned [106]. In addition, these materials possess low thermal conductivity, so the heat generated at the active region cannot dissipate efficiently towards the bottom layer. In the case of the HG reflector, the cap layer integrated on the SOI can transfer heat energy into the bottom Si layer efficiently. The long-wavelength mirrors are compared in terms of reflectance in Fig. 5.4. The dielectric DBR with 5 pair SiO_2/a-Si possesses the broadest bandwidth and the epitaxial DBR using wafer-fusion process shows the narrowest mirror. The HG mirror is the second broadest mirror and the bandwidth of the HCG mirror is wider than the epitaxial DBR. The HG reflector is compared with the dielectric DBR and HCG reflectors in terms of fractional bandwidth (FB) and bandwidth over thickness (BOT) introduced in Chap. 2. As shown in Table 5.2, the dielectric DBR has the highest bandwidth; hence, it has the highest FB. If the total thickness of the mirrors is considered, then

Table 5.2: FB/BOT for the dielectric DBR, TM HCG, and TM HG (λ = 1550 nm).

Type	Materials	Pair	Δn	d (μm)	FB (%)	BOT (%)
Dielectric DBR	SiO_2/ a-Si	5	2.16	~2.0	36.4	28.2
TM HCG	air/c-Si	1	2.48	~0.5	11.8	37.4
TM HG	InGaAlAs/ InP cap air/c-Si	1	3.583/ 3.1661 (n) 2.48	~0.77	25.7	51.6

the HG reflector shows the superiority due to the enhanced bandwidth obtained from using a thin cap layer. The InGaAlAS/InP cap layer of the HG reflector, which includes an active layer is used and the design parameters are shown in Table 5.3.

5.2.3 Fabrication tolerance

Considering the experimental feasibility of HG reflectors, it is necessary to estimate the effect of the possible experimental deviation on the reflectivity. For the HG reflectors, there is an additional possible deviation factor, t_c. A III-V cap layer, which includes an active material, will have multiple layers with different thicknesses. The parameters for a bottom grating, InGaAlAs-cap and InP-cap layers with corresponding μ and σ are given in Table 5.3. It is assumed that the period of Λ is close to the design. The thickness variation in the cap layer used for this analysis may be overestimated because the III-V epitaxy is grown using molecular beam epitaxy (MBE) or metalorganic chemical vapor deposition (MOCVD) with *in-situ* monitoring [119, 120]. The other possible deviations are from the bottom grating during an e-beam or a photolithography process to form a hard mask, which is used for the dry etching. Also, the possible non-uniformity of the Si layer can cause the deviation of the grating thickness. To estimate the effect of the deviation on reflectivity of HG reflectors, a Monte Carlo simulation is conducted by generating 10,000 random parameter combinations. The four parameters are randomly generated following the probability density function (pdf) for a normal distribution as

$$f(\mathrm{x}, \mu, \sigma) = \frac{1}{\sigma\sqrt{2\pi}} \exp\left[-\frac{(\mathrm{x}-\mu)^2}{2\sigma^2} \right], \tag{5.1}$$

Table 5.3: Design parameters and deviations of the TM HG reflector.

	Period (Λ, nm)	Grating thickness (t_g, nm)	Grating bar width (s, nm)	InGaAlAs (nm)	InP (nm)
Design (μ)	720	492	360	105.5	191.7
σ	-	4	4	2	2

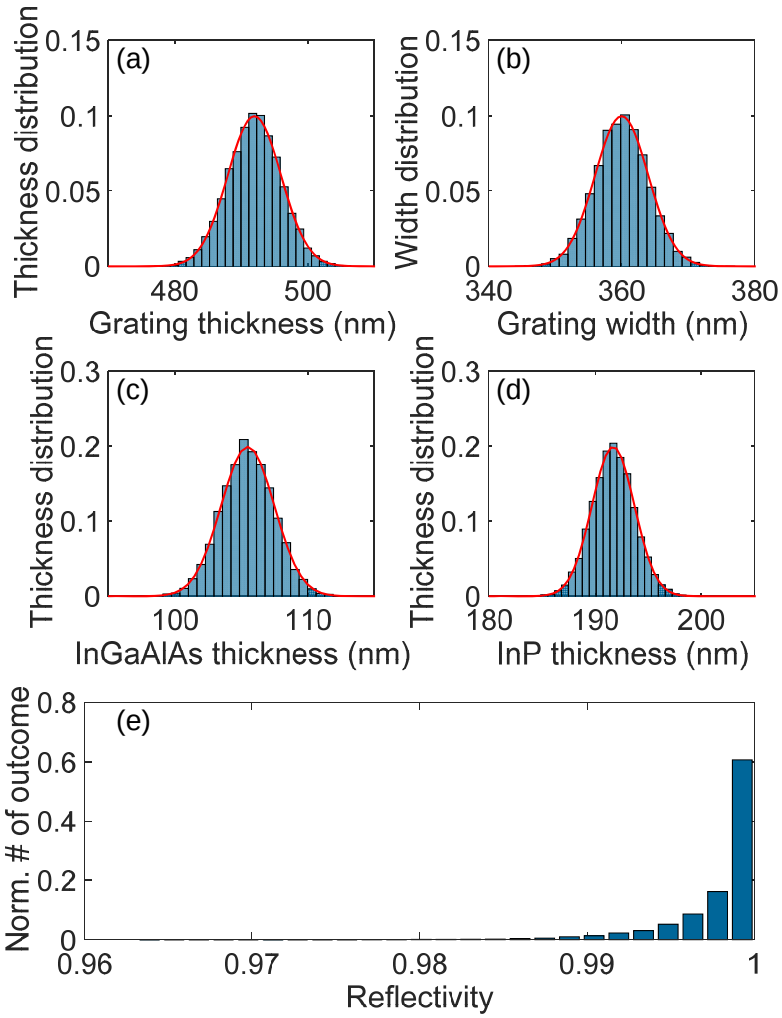

Figure 5.5: Numerical estimation of the design tolerance of HG reflector in terms of reflectivity. Probability distribution of (a) grating thickness, 'd', (b) grating width, 's', (c) thickness of InGaAlAs cap layer, and (d) thickness of InP cap layer. Overlayed red lines are the probability density function for a normal distribution with each mean, μ and standard deviation, σ, respectively. (e) Normalized reflectivity distribution of the HG reflectors.

where 'x' is the range for the corresponding parameters, μ is the mean value of the distribution, and σ is the standard deviation. The histograms showing the normal distribution for each parameter and the corresponding probability distribution function (pdf) with a red line are shown in Figs. 5.5(a-d). The total thickness deviation (Δt_c) considered here is ± 12 nm, and this may be a harsh estimation than a real deviation. Nevertheless, the total number of samples with reflectivity greater than 0.99 is 9740. This indicates that the HG reflectors have strong resistance to the potential experimental deviation.

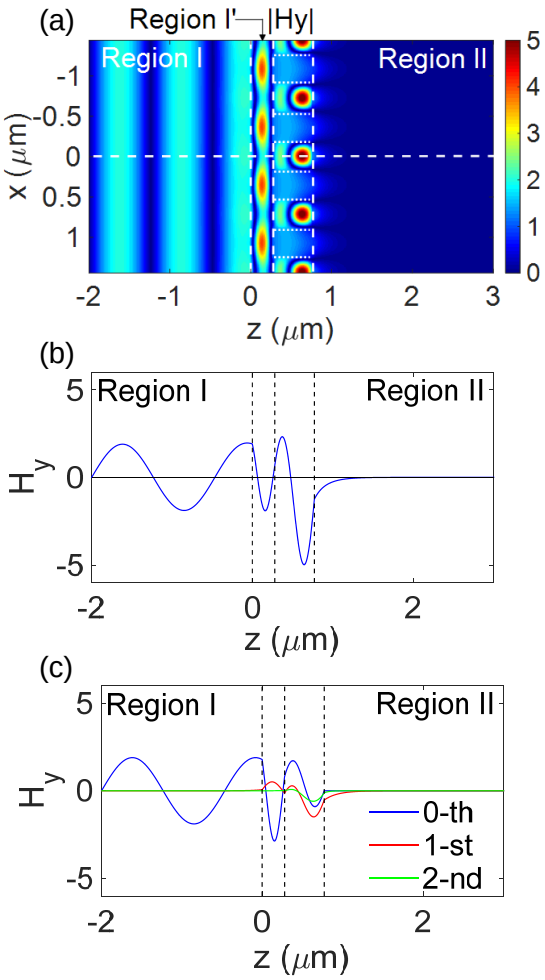

Figure 5.6: (a) 2D $|H_y|$ field profile of the HG reflector with a t_g of 279 nm at a wavelength of 1531 nm, (b) H_y field along the x = 0 as indicated as the white dashed line in (a), (c) and the decomposed harmonic components of the H_y field.

5.2.4 Role of high-refractive-index cap layer

5.2.4.1 Excitation of higher diffraction orders

To investigate the role of the cap layer, the 2D $|H_y|$ field profile is first shown in Fig. 5.6(a) and the total H_y field as a function of z at x = 0 and the lowest three harmonic components of the H_y field are plotted in Figs. 5.6(b, c), respectively. In the incident region (air, region I), there is a propagating plane wave along the z-direction. In region I′ which is the high-index cap layer, it seems that there are modes propagating along the x-direction only through the 0-th harmonic. Inside the grating region, there are excited Bloch eigenmodes, and in the exit region (region II, BOX), there is no field propagation. As shown in Fig. 5.6(a) in region I, the incident field are

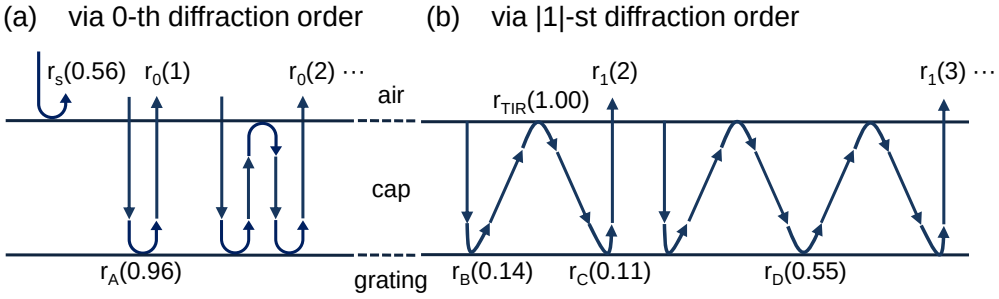

Figure 5.7: Diverse reflection and diffraction processes related to the broadband reflectance of a HG reflector.

almost reflected back from the HG reflector with a field intensity of ∼2 and this is confirmed by the H_y profile in Fig. 5.6(b) as well. In region II, there is an evanescent tail, which extends less than 1 μm into region II. The decompose field profile shows that the 0-th harmonic is related to the propagating wave in region I′ and in the HG structure. The 1-st harmonic component is an interrelated component, bridging the cap and the bottom grating. In contrast,the 2-nd harmonic component is only related to the bottom grating. The 1-st harmonic supports guided mode along the x-direction via the interaction between the cap and the bottom grating.

Figure 5.7 shows the potential diffraction orders excited inside the cap layer and the multiple round-trip supported by the bottom grating and total internal reflection (TIR) from the cap-air boundary. The high-index cap layer can excite higher diffraction orders according to the diffraction equations given as

$$\mathrm{n_{cap}}\sin(\theta_{\mathrm{diff},m}) = \mathrm{n_{cap}}\sin(\theta_{\mathrm{inc}}) - m\frac{\lambda_0}{\Lambda}, \qquad m = 0, \pm1, \pm2, \cdots, \tag{5.2}$$

where $\mathrm{n_{cap}}$ is the refractive index of the cap layer, λ_0 is the free-space wavelength, θ_{inc} is the incidence angle, $\theta_{\mathrm{diff},m}$ is the diffracted angle, m is the diffraction order. At normal incidence ($\theta_{\mathrm{inc}} = 0$), the diffraction equation is simplified as

$$\mathrm{n_{cap}}\sin(\theta_{\mathrm{diff},m}) = m\frac{\lambda_0}{\Lambda}, \qquad m = 0, \pm1, \pm2, \cdots, \pm|m_{max}| \tag{5.3}$$

with

$$m_{max} = \mathrm{n_{cap}}\frac{\Lambda}{\lambda_0}.$$

The maximum order of m_{max} for the normal incidence is determined by the

refractive index of the cap, the period of the bottom grating, and the incident wavelength. Therefore, by adjusting the three parameters, it is possible to excite higher orders only up to ±1-st orders in the region I′ and no transmitted diffraction orders in region II.

5.2.4.2 Re-guiding off-normal order to surface-normal one

As shown in Fig. 5.7, the diverse reflection and diffraction processes related to the broadband reflectance of a HG reflector are mainly divided into two groups depending on the involved diffraction orders inside the cap layer. The involved diffraction processes at the cap-grating boundary are represented as 'r' with subscripts of A, B, C, and D and with the magnitude of reflection coefficients in parenthesis at 1531 nm which is one of the GMR in Fig. 5.2(b). A series of processes related to the surface-normal direction via the surface reflection (r_s) and the 0-th diffraction order (r_A) are shown in Fig. 5.7(a) and are related to FP resonance. During each round trip, the surface-normal propagating light traveled toward the cap-air boundary and is transmitted as indicated $r_0(1)$, $r_0(2)$,$\cdots$. The subscript '0' indicates the 0-th order diffraction involved and the number inside the parenthesis is the number of round trips inside the cap layer.

Not just surface-normal multiple processes occur in the cap along the in-plane direction shown in Fig. 5.7(b), a series of processes initiated by the ±1-st diffraction orders (r_B) via the off-normal diffraction order (r_D) and TIR at the cap-air boundary (r_{TIR}) are related to GMRs. Only right-propagating processes are shown here and the same processes are repeated along the left direction. Through the +1-st diffraction orders (r_C) excited by the obliquely incident light from r_{TIR}, the propagating light traveling along the in-plane direction gradually leaked out along the surface-normal direction indicated as $r_1(2)$, $r_1(3)$,$\cdots$. The notation is the same used for the surface-normal processes.

First, the incident plane wave is partly reflected back as r_s and is partly transmitted. The transmitted light propagates in the cap layer and hit the bottom grating. Then, the 0, ±1 orders are excited and the 0-th order is indicated as r_A

and the +1-st order is indicated as r_B. The 0-th order propagates back and hit the cap-air boundary again. Via the repeated process initiated from the 0-th order diffraction of the normal incident light as shown in Fig. 5.7(a), Fabry-Perot (FP) resonance can be met if the phase condition of the multiple processes is in-phase at the air-cap boundary. Second, the ±1-st diffracted orders propagates along the transverse direction (x-direction) through the diffraction and total internal reflection (TIR) process, and then the propagating light leaks out via the 1-st order as shown in Fig. 5.7(b). This process is similar to that of optical waveguides supporting waveguide modes by using TIR process. In case of the HG reflector, the propagating orders are supported by TIR (r_{TIR}) and 0-th order diffraction (r_D) from the oblique incident light. If a propagating mode is sustained inside the cap layer of the HG reflector and gradually leaks out in-phase condition, then a GMR is excited.

5.2.4.3 In-phase condition for highly broadband reflector

Even though the high-index cap layer deteriorates the surface-normal reflection amplitude of r_A, it is still as high as 0.96. However, it is not enough for VCL applications to achieve a reflectance of $> 99.5\%$. The distributed energy through the ±1-st orders are propagated along the cap layer and leaked out through the 'r_1'. The surface-normal propagating light which is diffracted toward $r_1(2)$ through r_C diffraction possesses the amplitude of $2 \times |r_B r_C| = 0.03$, where the right- and left-propagating diffraction orders or ±1-st orders are counted. If the $\sum_i r_0(i)$ and $\sum_i r_1(i)$ are added in phase, then the total reflectivity could reach ∼1 at the cap-air boundary. Now that r_A is the dominant path in terms of reflectivity, few paths are needed to reach ∼1 if the two paths are in phase. The thickness of the cap layer should be considered when determining the in-phase condition of the two paths as well. Figure 5.8(a) shows the phase spectra of r_A, r_B,r_C and r_{TIR}. The phase spectra of r_B and r_C show strong distortion around the wavelength region where the HG reflector shows broadband reflectance. The sum of four phase spectra is shown in Fig. 5.8(b) and the distortion become clearer from 1400 to 1800 nm. The in-phase condition of the phase of $r_0(1)$ and $r_1(2)$ are then determined by the phase change

from the four processes and the propagation inside the cap. If the phase difference of $r_0(1)$ and $r_1(2)$ become a integer multiple of 2π, then the $r_0(1)$ and $r_1(2)$ are in phase. The integer multiple of 2π condition is linearly adjustable by tailoring the thickness of the cap layer. Figure 5.8(c) shows the (1-R) contour plot relative to increasing the thickness of the cap layer and the dark region indicates that there are strong resonances. On top of the contour plot, the calculated in-phase condition is overlaid with black dashed lines. The in-phase condition is well matched around the two GMRs of the HCG shown in Fig. 5.2(a) which implies that the very broad reflectance region is obtained from the interaction between the bottom grating and the cap layer via the dominant processes involved with the 0-th order plus the first $\pm$1-st orders. Importantly, at the cap layer thickness of 279 nm, the highly broadband reflectance HG is obtained as shown in Fig. 5.2(b) with 4 GMRs.

As the thickness of the cap layer increases, the in-phase condition is met at specific thickness (t_c) which excites another high reflective region as shown in Fig. 5.8. Since the increment of the cap layer adds the phase, which results from the propagation inside the cap, the in-phase condition will periodically occur. To confirm the periodic excitation of GMRs, the contour plot is sliced along the thickness axis at the four GMR wavelengths and it is shown in Fig. 5.9. At the 279 nm-thick cap

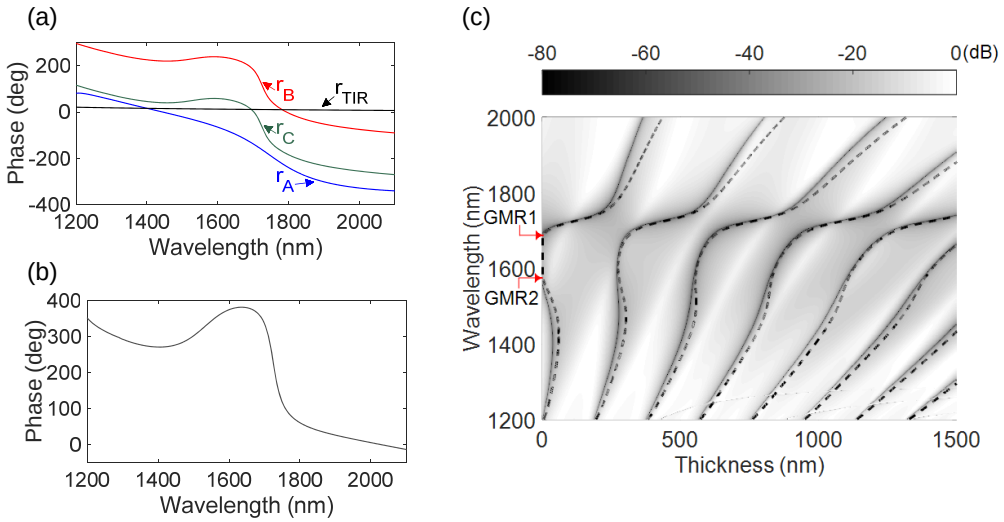

Figure 5.8: (a) Phase spectra of r_A, r_B, r_C, and r_{TIR}. (b) Total phase spectra of the four phase spectra. (c) (1-R) contour plot and the phase condition overlaid on top of the contour with the black dashed lines.

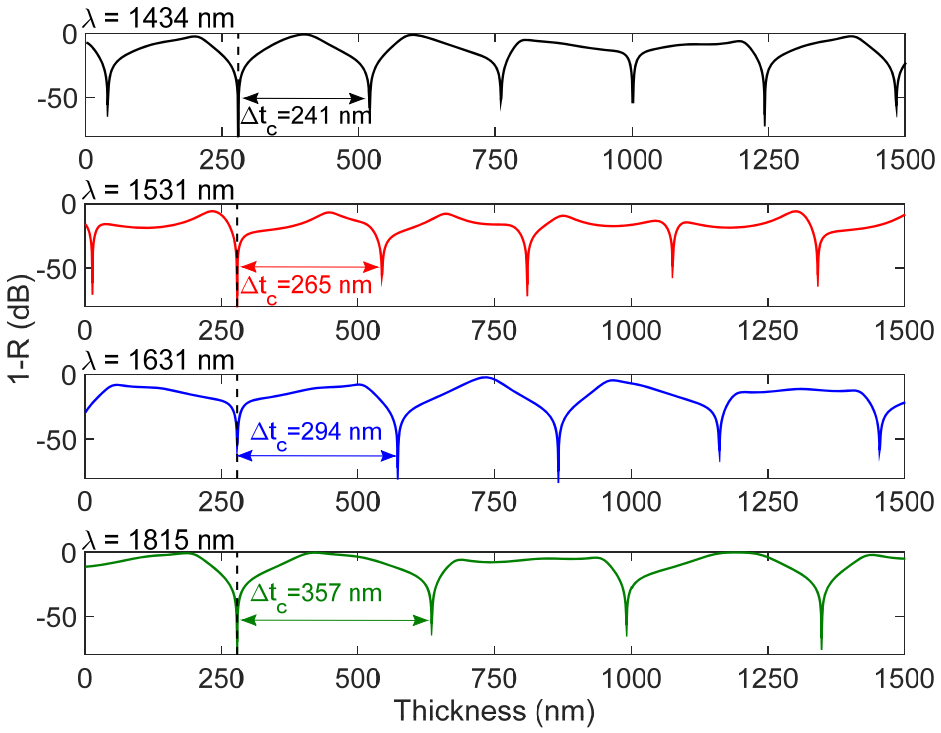

Figure 5.9: Periodically excited GMRs at the four GMR wavelengths of 1434, 1531, 1631, and 1815 nm, respectively, as increasing the thickness of cap layer.

layer which is indicated with black dashed lines, the four GMRs are well aligned and this contributes to the broad stopband. Above the 279 nm thickness, GMRs periodically occur with equal thicknesses (Δt_c). The Δt_c for the GMR wavelengths of 1434, 1531, 1631, and 1815 nm are 241, 265, 294, and 357 nm, respectively. The periodic excitation of GMRs proves that the role of the cap layer.

5.3 Experimental and Characterization Results

In order to experimentally demonstrate a HG reflector, a III-V cap layer which includes an active material was directly bonded on top of a Si layer of a silicon-on-insulator (SOI) wafer [76,79,90]. First, a grating region with a period of 720 nm and a grating bar width of 360 nm is formed onto the 492 nm-thick Si layer ($t_g = 492$ nm) of the SOI wafer using electron-beam lithography and a dry etching process. Then, a III-V layer consisting of an InGaAlAs layer (7 InGaAlAs/InGaAlAs quantum wells (QWs)) with a thickness of 105.5 nm and InP layer with a thickness of 191.7 nm is directly wafer-bonded onto the SOI wafer. The rigorous cleaning process and

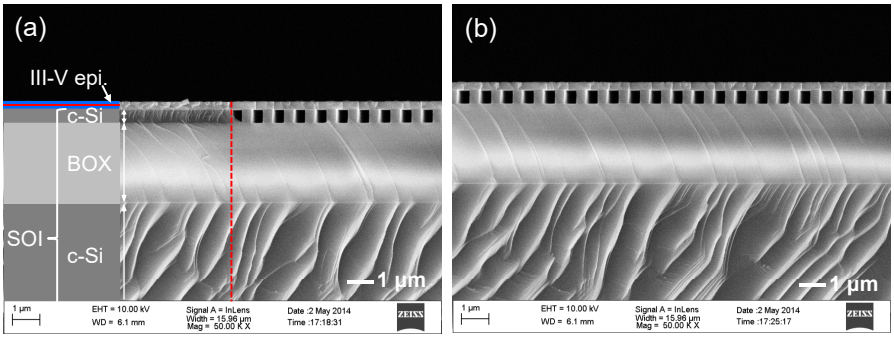

Figure 5.10: Cross-sectional SEM images of the fabricated HGR (a) at the border between the grating region and the unpatterned, indicated as red dotted line, and (b) at the center of the grating region.

the direct wafer bonding (DWB) process are explained in Chapter 3 in more detail. Then, the InP substrate is removed using a wet etching process. The area of the bottom grating is as large as 1 mm × 1 mm. Aligning the incident beam with the HG reflector on a free-space characterization setup is difficult because the size of the beam focused on the sample is ∼300 μm. It should be emphasized that all the processes used here are CMOS-compatible processes. To check the cross-section of the HG reflector, a HG sample was cleaved across the grating region. The bonded interface between the III-V layer and the bottom grating is shown in Fig. 5.10. The bonded interface tightly hold each other like the interface of the SOI wafer which is manufactured using a fusion bonding process. In addition, the sidewall profile of the gratings is almost vertical as required.

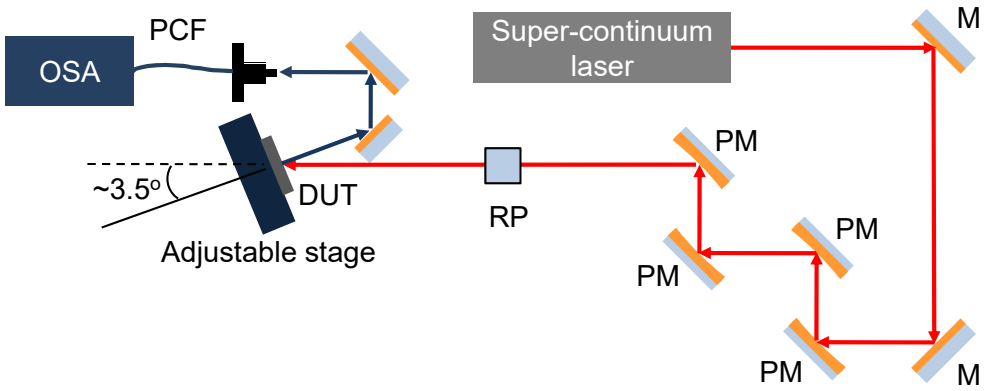

Figure 5.11: Measurement setup for the polarization-dependent HG reflector. (OSA: optical spectrum analyzer, PCF: photonic crystal fiber, DUT: device under test, RP: rotating polarizer, PM: parabolic mirror, M: mirror)

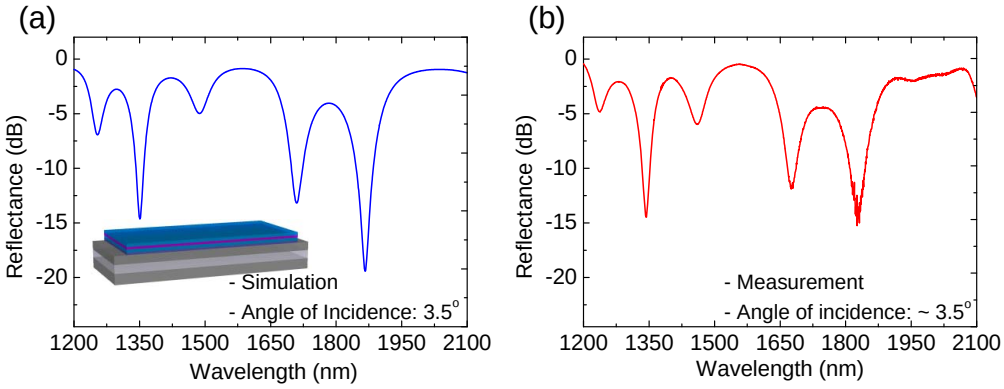

Figure 5.12: Reflectance spectra of the bonded III-V cap layer and unpatterned SOI sample. (a) Calculated and (b) measured reflectance spectra at an incidence angle of 3.5°, respectively.

To characterize the fabricated HG reflector in terms of reflectance, a free-space setup is used and is shown in Fig. 5.11. A super-continuum laser (SuperK Extreme, NKT Photonics) is used as a broadband light source. The light is guided using mirrors and parabolic mirrors to focus the light at the surface of the HG reflector. A rotating polarizer is used to control the polarization of the incident light. The HG sample is loaded on the adjustable stage and it is slightly tilted ∼3.5° relative to the incident light path to collect the reflected light from the HG. The reflected light is guided by two mirrors, collected by photonic crystal fiber (PCF)(NKT Photonics, LMA-10), and then measured using OSA (AQ6375, Yokogawa).

To align the incident light on the HG reflector by adjusting the stage, the optical spectrum is used to estimate the beam position. First, a rough alignment is done by seeing a bright spot on the HG sample. By arranging the position of the stage, the spot is put within the III-V layer. Still, the position is not within the grating region. To confirm the position the spectrum is used as shown in Fig. 5.12, where the III-V cap layer is on top of a flat Si layer. The simulation and the experimental result are quite similar, except for the overall blue shift of the calculated one. This can be attributed to the constant refractive indices, neglecting the dispersion of refractive indices. While observing this spectrum as shown in Fig. 5.12, the beam position is still outside of the grating region but within the area of the III-V cap layer. After entering into the grating region, the spectrum is suddenly changed,

and then the beam position is confirmed by comparing the deep position between the calculated and measured spectra. After measuring the spectrum of the HG reflector, the spectrum of a gold mirror is measured using the same setup, which is used to calibrate the measured spectrum of the HG reflector. Figure 5.13(a) shows the cross-section of the TM HG reflector; the calculated and measured spectra are shown in Figs. 5.13(b, c), respectively. The measured result is blue shifted compared to the calculated result. Except for the blue shift, the calculated and measured spectra with a TM-polarized incident light show good agreement. In Fig. 5.13(c), there is a region where the measured reflectance is slightly higher than 1. This can be explained if the HG reflector shows as higher reflectance than that of the gold mirror. To check the polarization sensitivity, the TM HCG is tested with a TE-polarized incident light and by rotating the rotating polarizer. As shown in

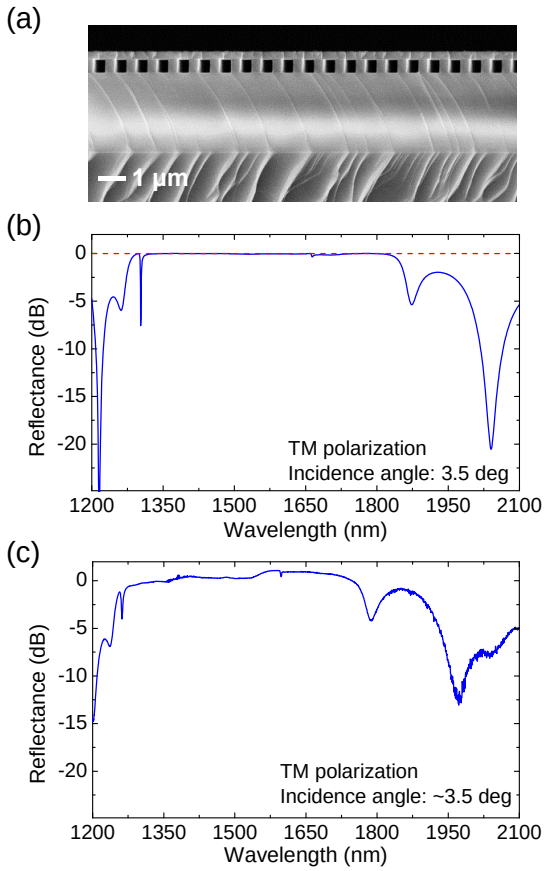

Figure 5.13: (a) Cross-sectional SEM image of the fabricated TM HG reflector. (b) Calculated and (c) measured reflectance spectra at the incidence angle of 3.5°, respectively, with TM-polarized incident light.

Fig. 5.14, the calculated and measured spectra are very similar, and sharp Fano resonance is observed as well. In addition, the reflectance near 1550 nm is as low as -3.5 dB, whereas ∼0 dB was observed for the TM-polarized light.

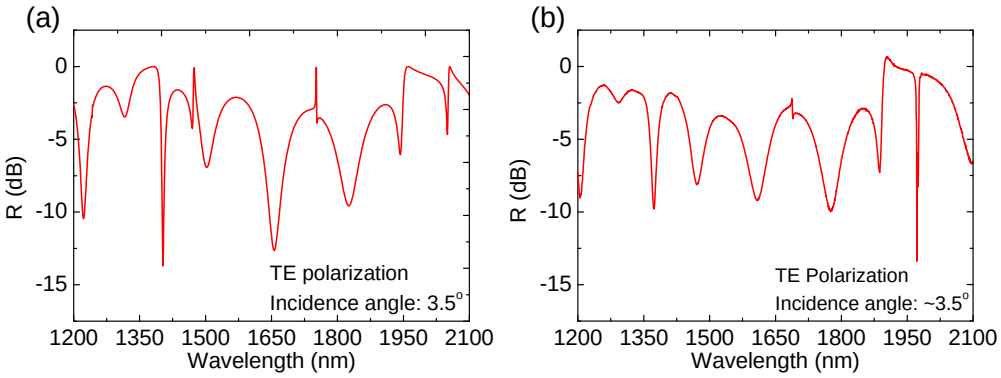

Figure 5.14: (a) Calculated and (b) measured reflectance spectra of the TM HCG at the incidence angle of 3.5°, respectively, with TE-polarized incident light.

5.4 Summary

To sum up, the HG reflector was rigorously investigated focusing on the role of a high-index cap layer, and it was experimentally demonstrated using the CMOS-compatible fabrication processes. The interaction between the cap layer and the bottom grating resulted in strong Fabry-Perot (FP) resonance as well as weak guided mode (GM) resonance. Most of the reflected power came from the FP resonance while the weak GM resonance assisted to achieve 100% reflectance as well as broad the stopband as wide as 300 nm.

The fabrication and characterization of the HG reflector heterogeneously integrated on the SOI platform showed the feasibility of an alternative to HCG-based hybrid VCLs, which need an air gap having a low thermal conductivity. Therefore, this type of hybrid VCLs have potential to solve the heat dissipation challenge more efficiently because the III-V layer including the active region directly contact the bottom Si layer, which functions as a heat spreader.

Somewhere, something incredible is waiting to be known.

— Carl Sagan

6 Conclusion and Outlook

6.1 Conclusion

In this thesis work, the initial proof-of-concept experiment of the Si-integrated long-wavelength hybrid vertical cavity lasers (VCLs) has been conducted. The primary goal of the research was 1) to prove the possibility of the in-plane emission using the vertical cavity structure and 2) to demonstrated the potential for the high-speed operations with the long-wavelength vertical cavity structure. The Si-integrated hybrid VCLs were integrated on the SOI platform for optical interconnect applications. Also, for the long-wavelength application, the novel grating mirror as a bottom reflector and the top dielectric DBR as an alternative for the bulky epitaxial DBR. Firstly, for the in-plane emission, the Si HCG as the bottom mirror was transferred on the SOI platform, which could route the vertically-amplified light laterally into the Si waveguide. The top dielectric DBR was employed to replace the bulky epitaxial DBR. Secondly, at the long wavelength of 1540 nm, the potential for the high-speed operation of the Si-integrated VCLs was demonstrated as well. Furthermore, during the thesis work, the HG reflector was experimentally proven with the rigorous explanation of the role of the high-index cap layer.

For the 1550 nm long-wavelength VCSELs with an InP material system, one of the challenges to be solved is the thick epitaxial DBR mirrors, which limit the high-

speed operations. Also, for the on-chip optical interconnect applications, the vertical emission is rather a hindrance to be applied as light sources. Even though VCSELs have proven them as fast and energy-efficient light sources in short-distance optical communication and data center applications, the vertically-emitted light should be coupled to an on-chip Si waveguide. The unique function of the HCG reflector was used to address the two issues. Therefore, the HCG is utilized not only for the high reflective mirror but also the in-plane router to the in-plane Si waveguide. The thickness of the bottom HCG, which is designed for the long-wavelength mirror, was less than 500 nm with a broader reflectance bandwidth. The stopband is wider than the very thick wafer-fused epitaxial DBR. Not only the physical thickness, but it also has a short energy penetration depth as well, which allows for the high-speeds operation of a laser. For the top mirror, a dielectric DBR with high index contrast was used because of the high index contrast, which requires a fewer pair of the DBR. The total thickness of the DBR is much thinner than the epitaxial DBR, and the bandwidth of the dielectric DBR become wider as well.

To implement the hybrid structure using the III-V gain material and the two different mirrors, the device fabrication procedure was conceived and then developed. First of all, the oxygen plasma-assisted direct wafer bonding (DWB) was developed with a rigorous cleaning process and an additional DIW surface treatment. The DWB bonding process was done at a temperature as low as 300°C. The bonding strength was confirmed indirectly by removing the thick InP substrate in a HCl solution for 60 minutes. During the InP substrate removal process, the substrate was properly removed. Then, $\sim$1 μm-thick membrane was remained, and it was tightly bonded on the SOI wafer during the entire fabrication process. For the DBR formation, the lift-off process and the etch-back process were developed. First, the lift-off process was developed for the SiO_2/TiO_2 DBR because the TiO_2 is a hard material, which cannot be readily etched using dry etch. Second, the etch-back process was developed for the SiO_2/a-Si DBR because the index contrast is higher than the SiO_2/TiO_2 DBR. Therefore, it enhances the vertical confinement factor and improves the 3 dB frequency. Last but not least, the sacrificial layer etching

process was developed to introduce the air gap between the III-V layer and the bottom HCG. For the sacrificial etch, the two via holes and the air part of the bottom HCG are used as channels for the wet etchant. The position of two via holes relative to the direction of the HCG grating was assigned to parallel to the grating. In this way, the sacrificial etch was done uniformly and fast.

The fabricated hybrid VCL was characterized by optical pumping scheme. For the hybrid VCL with an in-plane emission, the pump laser was focused on the center of the top DBR. The 980 nm pump laser was chosen because the top DBR stopband started from below 1300 nm and above 980 nm. Due to the thermal issue, which caused by the absorbed power from the pump laser on the Si and the accumulated heat energy in the active region, the pulsed operation was used. The in-plane emission was measured from the end of the Si waveguide, and it showed the evident lasing phenomenon. In addition, the measured far field of the in-plane emission from the Si waveguide showed the well-confined profile. To confirm the high-speed possibility, the high-speed VCL was fabricated by employing the short effective cavity length, which consisted of the top dielectric DBR and the bottom TM-HCG. Then, the small-signal frequency response was measured, and the maximum 3 dB frequency was 27.2 GHz at the 1540 nm in wavelength. This measured result was limited due to the condition of the measurement setup, especially the input power which pump the hybrid VCL. We expect that if the input power increases more, then the 3 dB frequency enhances accordingly. The measured MCEF and D-factor were 42.1 GHz/mA$^{1/2}$ and 11.2 GHz/mA$^{1/2}$, respectively. From the linear lines of MCEF and D-factor graphs within the input power range, it seems that there is room to enhance the 3 dB frequency further if the injected input power is further increased. The static characteristic of 49 dB was also noteworthy. From the observed multiple sub-peaks of the hybrid VCL, the unique dispersion characteristic was analyzed, and it resulted from the unpatterned bottom mirror.

The new type of grating mirror, HG reflector using a III-V active layer was fabricated. It showed high reflective of $\sim$0 dB over the uninterrupted wavelength range of $>$ 300 nm which is even wider than that of HCGs. Within the high-index

III-V layer, the ±1-st orders are excited from the surface-normal incident light, and the two modes are captured inside the cap layer with the aid of both the TIR from the cap-air boundary and the oblique 0-th diffraction from the bottom grating. At the bottom grating, a small fraction of the surface-normal diffracted orders excited (±1-st) as well. While propagating along the cap layer, the traveling light leaked out along the surface-normal direction via the surface-normal diffracted orders. These small amounts of the leaked-out light contributed to the more than 99.5% reflectance of the HG reflector over the broad wavelength range.

To conclude and summarize, the conducted researches and experiments have proven the concept of the Si-integrated long-wavelength VCL, which emitted light laterally into the Si waveguide. Also, the possibility of the high-speed long-wavelength VCL has been also demonstrated. Besides, the HG reflector showed the potential to be employed for the vertical cavity structure, which would solve the heat dissipation problem with ease. The optically-pumped hybrid vertical cavity structure can be transferred to an electrically-pumped version using the current long-wavelength VCSEL technology. The Si-integrated long-wavelength VCLs with an in-plane emission, which inherit the high-speeds and energy-efficient properties of the vertical cavity laser structures, can be used as light sources for optical interconnects.

6.2 Outlook

The main works conducted in this thesis are *the proof-of-concept demonstration* of 'the Si-integrated long-wavelength hybrid VCLs', which are the optically-pumped lasers. The demonstration proves that the vertical cavity laser, which employs the bottom Si HCG mirror, emits light into the in-plane Si waveguide with the potential for the high-speed operations. Based on this laser structure, an electrically-pumped hybrid VCLs can be implemented by using the today's long-wavelength VCSEL technology.

First, for an electrically-pumped hybrid vertical cavity laser based on the InP material system, the current confinement with a small series resistance can be achieved with a buried tunnel junction [30, 39]. The other way to confine the

injected current is to introduce an ion-implanted aperture above QWs layer [107]. Besides, by manipulating the bottom HCG design, a transverse optical mode can be controlled as well [111]. To confine the optical mode, a HCG with a heterostructure along x- and y-direction can be used [111]. The center part of the HCG works as a part of the laser cavity. The outside of the center part works as barriers, which confine the transverse mode into the center [111, 121, 122]. Both the current confinement structure and the hetero-HCG design can be controlled to alleviate the laser threshold condition.

To inherit the high intrinsic speed of long-wavelength hybrid VCL, it is equally important to consider device parasitics from the metal pads and mesa area of an electrically-pumped laser. The mesa size and the metal pad area need to be minimized to reduce the charged area; and hence, the device capacitance can be reduced [39]. To further reduce the parasitic capacitance from the metal pad, a low permittivity material such as a benzocyclobuthene can be used [39]. Besides, the pad resistance needs to be optimized. Then, the distributed RC time constant resulted from the device can be minimized [39], and it will preserve the high-speed performance.

For heat dissipation, a metal heat spreader can be connected to the top metal pad [25], which will transfer the heat energy from the active region. In this way, a thermal resistace lower than 1 K/mW is achievable [25]. The other way is to use the HG reflector as a bottom mirror. The HG reflector can include a III-V active layer inside the cap layer, and the III-V layer is directly contacted to the large area bottom silicon. This will be beneficial regarding the heat dissipation because the generated heat inside the III-V layer can flow to the underlying Si layer. Therefore, HG reflector may improve the heat dissipation efficiency of HCG-based hybrid VCL structure.

The investigated hybrid VCLs have the potential for the high-speeds and energy-efficient on-chip optical interconnects at the near future. In the long-term perspective, with the development of technology, a nano-scale light sources, such as a nano-cavity plasmonic light sources [123], or the other kinds of light sources

will replace the current promising light sources, which will be more energy efficient and will support higher data transmission.

Appendices

A

RCWA for a Multi-block Structure

For a general multi-block structure, the same algorithm employed for the two-block case used in Chapter 2, can be extended, and the **S** matrix and **c** matrix for the multi-block can be obtained. The part of the multi-block is shown in Fig. A.1 and the superscript, for instance, (n,m+n+l) indicates the first and last layer of the part [69, 70]. The **S** matrix of the part can be obtained from the first sub-part (n,n+m) and the second sub-part (n+m+1,n+m+l) using the Redheffer product as

$$\overleftarrow{\mathbf{R}}^{(\mathrm{n,n+m+l})} = \overleftarrow{\mathbf{R}}^{(\mathrm{n,n+m})} + \overleftarrow{\mathbf{T}}^{(\mathrm{n,n+m})} \left[\mathbf{I} - \overleftarrow{\mathbf{R}}^{(\mathrm{n+m+1,n+m+l})} \overrightarrow{\mathbf{R}}^{(\mathrm{n,n+m})}\right]^{-1} \overleftarrow{\mathbf{R}}^{(\mathrm{n+m+1,n+m+l})} \overrightarrow{\mathbf{T}}^{(\mathrm{n,n+m})} \tag{A.1a}$$

$$\overrightarrow{\mathbf{T}}^{(\mathrm{n,n+m+l})} = \overrightarrow{\mathbf{T}}^{(\mathrm{n+m+1,n+m+l})} \left[\mathbf{I} - \overrightarrow{\mathbf{R}}^{(\mathrm{n,n+m})} \overleftarrow{\mathbf{R}}^{(\mathrm{n+m+1,n+m+l})}\right]^{-1} \overrightarrow{\mathbf{T}}^{(\mathrm{n,n+m})} \tag{A.1b}$$

$$\overrightarrow{\mathbf{R}}^{(\mathrm{n,n+m+l})} = \overrightarrow{\mathbf{R}}^{(\mathrm{n+m+1,n+m+l})} + \overrightarrow{\mathbf{T}}^{(\mathrm{n+m+1,n+m+l})} \left[\mathbf{I} - \overrightarrow{\mathbf{R}}^{(\mathrm{n,n+m})} \overleftarrow{\mathbf{R}}^{(\mathrm{n+m+1,n+m+l})}\right]^{-1} \overrightarrow{\mathbf{R}}^{(\mathrm{n,n+m})} \overleftarrow{\mathbf{T}}^{(\mathrm{n+m+1,n+m+l})} \tag{A.1c}$$

$$\overleftarrow{\mathbf{T}}^{(\mathrm{n,n+m+l})} = \overleftarrow{\mathbf{T}}^{(\mathrm{n,n+m})} \left[\mathbf{I} - \overleftarrow{\mathbf{R}}^{(\mathrm{n+m+1,n+m+l})} \overrightarrow{\mathbf{R}}^{(\mathrm{n,n+m})}\right]^{-1} \overleftarrow{\mathbf{T}}^{(\mathrm{n+m+1,n+m+l})}. \tag{A.1d}$$

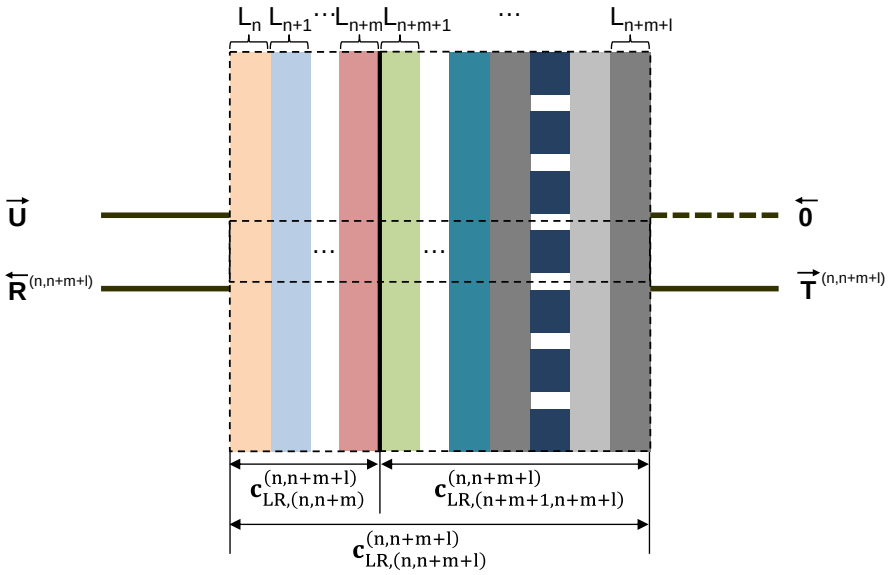

Figure A.1: Illustration of multi-block S-matrix component and coupling coefficients (left-to-right direction illustrated only). The dashed square box in the middle indicates the unit cell of the multi-block structure.

Then, the S-matrix of the part is rewritten as Redheffer star product of the multi-block structure

$$\mathbf{S}^{(\mathrm{n,n+m+l})} = \mathbf{S}^{(\mathrm{n,n+m})} * \mathbf{S}^{(\mathrm{n+m+1,n+m+l})}, \tag{A.2}$$

and each sub-part can be finally decomposed with each single-block using the Redheffer star product. The coupling coefficient set of the sub-part of multi-block structure can be written as

$$\mathbf{c}^{(\mathrm{n,n+m+l})}_{\mathrm{LR,(n,n+m+l)}} = \left\{\mathbf{c}^{(\mathrm{n,n+m+l})}_{\mathrm{LR,(n,n+m)}}, \mathbf{c}^{(\mathrm{n,n+m+l})}_{\mathrm{LR,(n+m+1,n+m+l)}}\right\} \tag{A.3a}$$

$$\mathbf{c}^{(\mathrm{n,n+m+l})}_{\mathrm{RL,(n,n+m+l)}} = \left\{\mathbf{c}^{(\mathrm{n,n+m+l})}_{\mathrm{RL,(n,n+m)}}, \mathbf{c}^{(\mathrm{n,n+m+l})}_{\mathrm{RL,(n+m+1,n+m+l)}}\right\}, \tag{A.3b}$$

and can be expressed with the interconnected coupling coefficient of the single layer, $\mathrm{n} \sim \mathrm{n+m+l}$ [69, 70].

$$\mathbf{c}^{(\mathrm{n,n+m+l})}_{\mathrm{LR,(n,n+m)}} = \left\{\mathbf{c}^{(\mathrm{n,n+m+l})}_{\mathrm{LR,(n)}}, \mathbf{c}^{(\mathrm{n,n+m+l})}_{\mathrm{LR,(n+1)}}, \cdots, \mathbf{c}^{(\mathrm{n,n+m+l})}_{\mathrm{LR,(n+m)}}\right\} \tag{A.4a}$$

$$\mathbf{c}^{(\mathrm{n,n+m+l})}_{\mathrm{RL,(n,n+m)}} = \left\{\mathbf{c}^{(\mathrm{n,n+m+l})}_{\mathrm{RL,(n)}}, \mathbf{c}^{(\mathrm{n,n+m+l})}_{\mathrm{RL,(n+1)}}, \cdots, \mathbf{c}^{(\mathrm{n,n+m+l})}_{\mathrm{RL,(n+m)}}\right\} \tag{A.4b}$$

$$\mathbf{c}^{(\mathrm{n,n+m+l})}_{\mathrm{LR,(n+m+1,n+m+l)}} = \left\{\mathbf{c}^{(\mathrm{n,n+m+l})}_{\mathrm{LR,(n+m+1)}}, \mathbf{c}^{(\mathrm{n,n+m+l})}_{\mathrm{LR,(n+m+2)}}, \cdots, \mathbf{c}^{(\mathrm{n,n+m+l})}_{\mathrm{LR,(n+m+l)}}\right\} \tag{A.4c}$$

$$\mathbf{c}^{(\mathrm{n,n+m+l})}_{\mathrm{RL,(n+m+1,n+m+l)}} = \left\{\mathbf{c}^{(\mathrm{n,n+m+l})}_{\mathrm{RL,(n+m+1)}}, \mathbf{c}^{(\mathrm{n,n+m+l})}_{\mathrm{RL,(n+m+2)}}, \cdots, \mathbf{c}^{(\mathrm{n,n+m+l})}_{\mathrm{RL,(n+m+l)}}\right\}. \tag{A.4d}$$

The coupling coefficient of the part is now expressed using the star product as

$$\begin{aligned}&\left(\mathbf{c}^{(\mathrm{n,n+m+l})}_{\mathrm{LR,(n,n+m+l)}}, \mathbf{c}^{(\mathrm{n,n+m+l})}_{\mathrm{RL,(n,n+m+l)}}\right) = \\ &\left(\mathbf{c}^{(\mathrm{n,n+m})}_{\mathrm{LR,(n,n+m)}}, \mathbf{c}^{(\mathrm{n,n+m})}_{\mathrm{RL,(n,n+m)}}\right) * \left(\mathbf{c}^{(\mathrm{n+m+1,n+m+l})}_{\mathrm{LR,(n+m+1,n+m+l)}}, \mathbf{c}^{(\mathrm{n+m+1,n+m+l})}_{\mathrm{RL,(n+m+1,n+m+l)}}\right).\end{aligned} \tag{A.5}$$

Then, the total $\mathbf{S}$ matrix and the $\mathbf{c}$ matrix of the multi-block with N layers can be now expressed as

$$\mathbf{S}^{(\mathrm{1,N})} = \mathbf{S}^{(\mathrm{1,1})} * \mathbf{S}^{(\mathrm{2,2})} * \mathbf{S}^{(\mathrm{3,3})} * \cdots * \mathbf{S}^{(\mathrm{N-1,N-1})} * \mathbf{S}^{(\mathrm{N,N})} \tag{A.6a}$$

$$\begin{aligned}\left(\mathbf{c}^{(\mathrm{1,N})}_{\mathrm{LR,(1,N)}}, \mathbf{c}^{(\mathrm{1,N})}_{\mathrm{RL,(1,N)}}\right) = &\left(\mathbf{c}^{(\mathrm{1,1})}_{\mathrm{LR,(1)}}, \mathbf{c}^{(\mathrm{1,1})}_{\mathrm{RL,(1)}}\right) * \left(\mathbf{c}^{(\mathrm{2,2})}_{\mathrm{LR,(2)}}, \mathbf{c}^{(\mathrm{2,2})}_{\mathrm{RL,(2)}}\right) * \\ &\cdots * \left(\mathbf{c}^{(\mathrm{N-1,N-1})}_{\mathrm{LR,(N-1)}}, \mathbf{c}^{(\mathrm{N-1,N-1})}_{\mathrm{RL,(N-1)}}\right) * \left(\mathbf{c}^{(\mathrm{N,N})}_{\mathrm{LR,(N)}}, \mathbf{c}^{(\mathrm{N,N})}_{\mathrm{RL,(N)}}\right).\end{aligned} \tag{A.6b}$$

B

PL Data of III-V Epitaxy

Figure B.1 shows the representative PL spectrum and PL mapping data of the III-V epitaxy used in this thesis work. The III-V epitaxy structure is shown in Table 3.1. The peak material gain is 1541 nm over almost all 2-inch area.

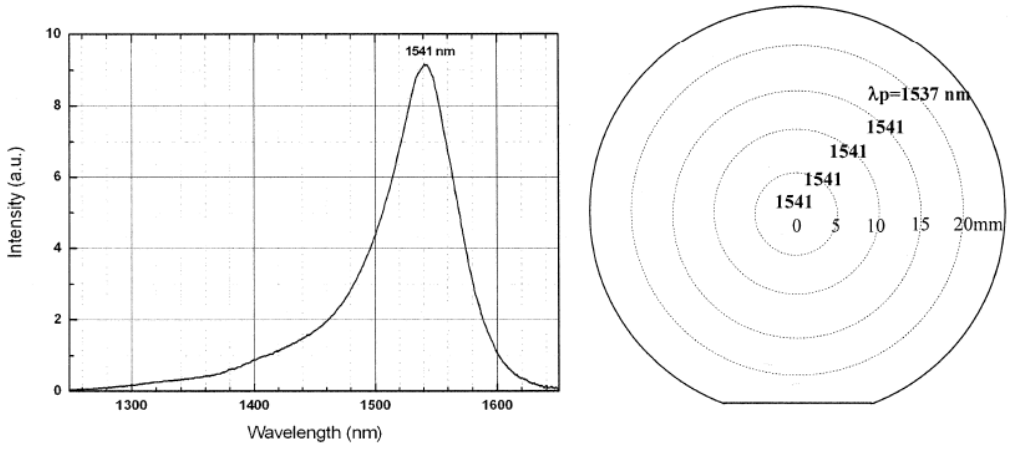

Figure B.1: (a) A representative PL spectrum and (b) a PL mapping data of the III-V epitaxy measured at RT.

C

Optical Properties of DBR Materials.

C.1 SiO_2 and TiO_2 deposited by IBD

In here, the optical properties of the DBR materials, which were used for the two types of DBRs, are presented. First, the measured refractive indice of SiO_2 and TiO_2 materials are shown in Figure C.1. These two materials are deposited for the DBR, which is formed using the lift-off process. Before depositing an entire 7 pair DBR, each layer of SiO_2 and TiO_2 material was deposited and then the index was confirmed by using Ellipsometer VASE. Based on the index information, a quarter-lambda thickness is estimated, respectively, and then the DBR is deposited.

In addition, the extinction coefficient was measured as well because if the

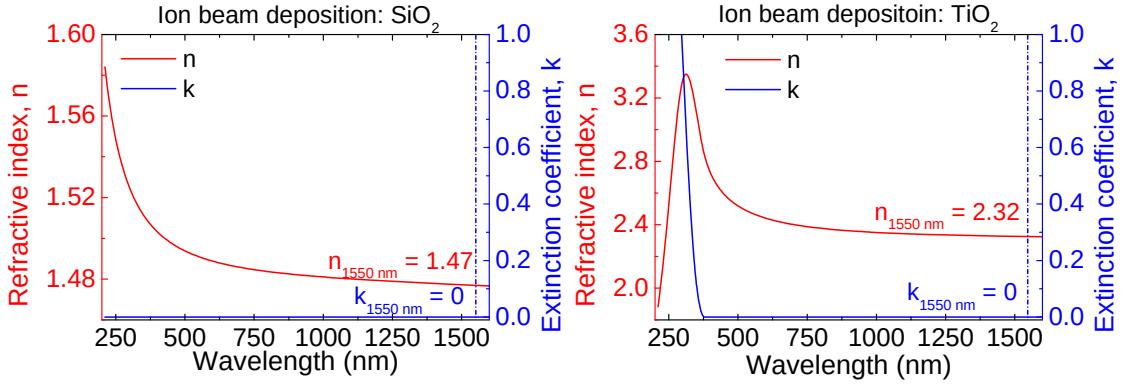

Figure C.1: Refractive index and extinction coefficient of (left) the SiO_2 and (right) the TiO_2 layer deposited by using IBD.

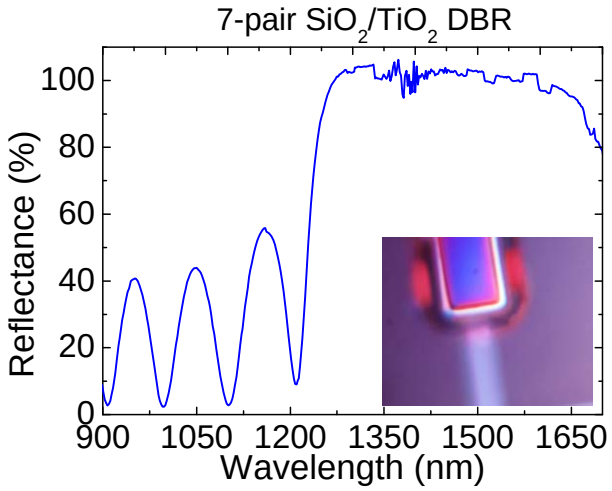

Figure C.2: Measured reflectance spectrum of the 7 pair SiO_2/TiO_2 DBR formed by the lift-off process.

absorption loss in the DBR is too high, then it cannot be used as a DBR for a laser having a specific gain which cannot overcome the overall loss including the DBR. The measured extinction coefficient was 0 at the 1550 nm. Even thought it is possible to deposit a-Si having a high refractive index of 3.970 at 1550 nm using the IBD, it has a high extinction coefficient of 0.062 at the same wavelength as well. Therefore, the a-Si cannot be chosen. The measured refractive indice are $n_{TiO_2} = 2.32$ and $n_{SiO_2} = 1.47$ at 1550 nm and the refractive index contrast is 0.85. The measured reflectance spectrum of a 7 pair SiO_2/TiO_2 DBR is shown in Fig. C.2. The high reflectance region covers the target wavelength, 1550 nm. In addition, the DBR exhibits less than 20% reflectance around 980 nm in wavelength. Therefore, for the optical pump with a 980 nm, the pump power can be efficiently transmitted through the top DBR. However, a 1300 nm pump laser cannot be used because the wavelength is within the stopband. The inset in Fig. C.2 shows the top-view microscope image of the DBR.

C.2 a-Si and SiO_2 deposited by III-V dielectric evaporator

The refractive index and the extinction coefficient of the a-Si deposited by using a III-V dielectric evaporator are shown in Fig. C.3. The optical properties are

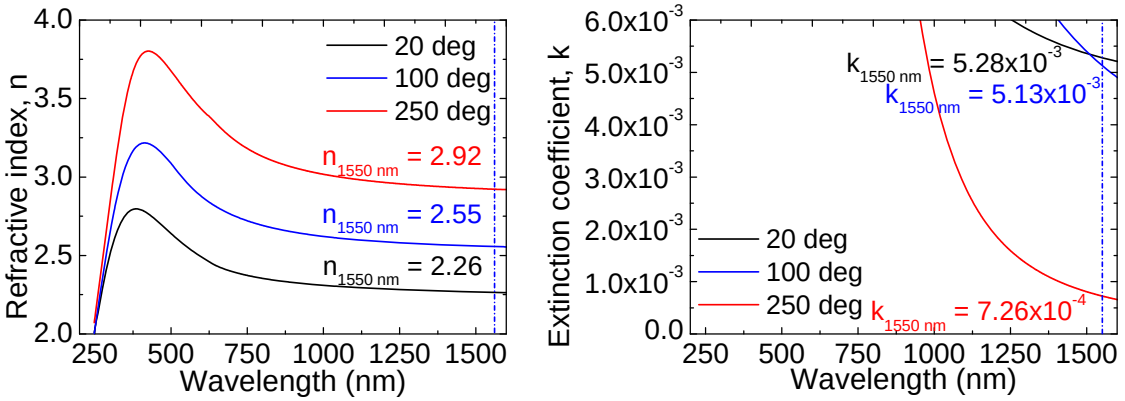

Figure C.3: Measured refractive index and extinction coefficient of a-Si deposited by using the III-V dielectric evaporator in vacuum environment at 20, 100, and 250 °C.

depend on the deposition temperature, and especially to get low loss a-Si, it is imperative to deposit the a-Si at 250 °C. Therefore, the lift-off process is in principle impossible. The refractive index and the extinction coefficient are 2.92 and 7.26×10^{-4}, respectively, at 250 °C. The SiO_2 source has no temperature-dependency. The measure refractive index and extinction coefficient are shown in Fig. C.4, and the refractive index is 1.45 with no loss. The refractive index contrast of the a-Si and the SiO_2 is 1.47. The 6-pair a-Si/SiO_2 is shown in Fig. C.5 with the cross-sectional SEM image of the DBR. The high reflectance region covers the target lasing wavelength of 1550 nm. Near the 980 nm, where the pump laser operates, the reflectance is ∼35%.

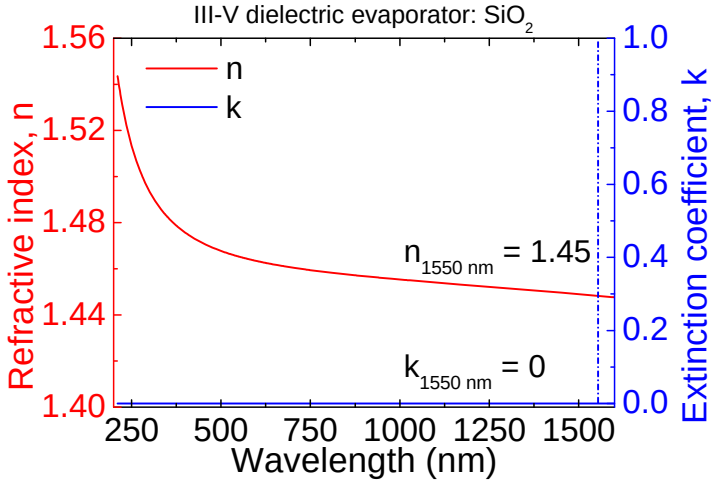

Figure C.4: Measured refractive index and extinction coefficient of SiO_2 deposited by using the III-V dielectric evaporator in vacuum environment at 250 °C.

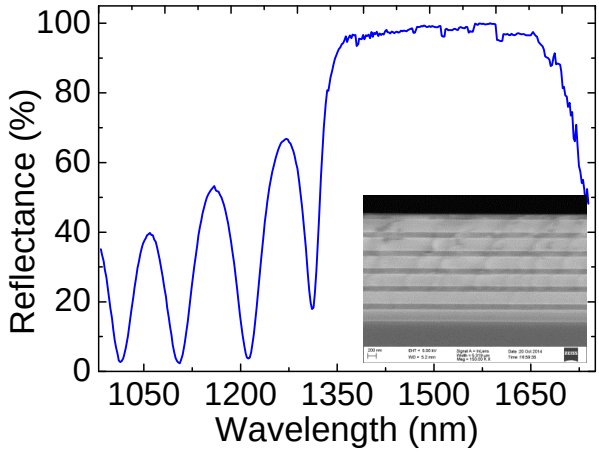

Figure C.5: Measured reflectance spectrum of the 6-pair a-Si/SiO_2 DBR deposited by using the III-V dielectric evaporator.

D

Beam Waist Measurement.

In here, the way to measure the beam waist is explained. The measured beam waists of the hybrid VCL and 980 nm pump laser are used in Chapter 4 to estimate the absorbed input power.

D.1 Beam Waist of Pump Laser

First, to measure the beam waist of the 980 nm pump laser, the pump laser is focused on the surface of the flat Si layer which is outside of the III-V active layer. By increasing the pump power, the reflected image of each input power on the Si surface is captured by using a NIR InGaAs camera as shown in Fig. D.1(a-c). Then, the captured images are analyzed by using an image processing software (ImageJ). On the bright spot of the pump beam images, a straight line is drawn, which crosses the center of the beam, and then the intensity profile is obtained. The fitted results are shown in Fig. D.1(d-f). The entire measured results for the different input power are shown in Table D.1. By averaging the results from the input power of 1.5 to 18.0 μW, the estimated pump beam waist of 5.84 μm is obtained. The first two results in Table D.1 are not used because the input power are too weak to measure the waist correctly.

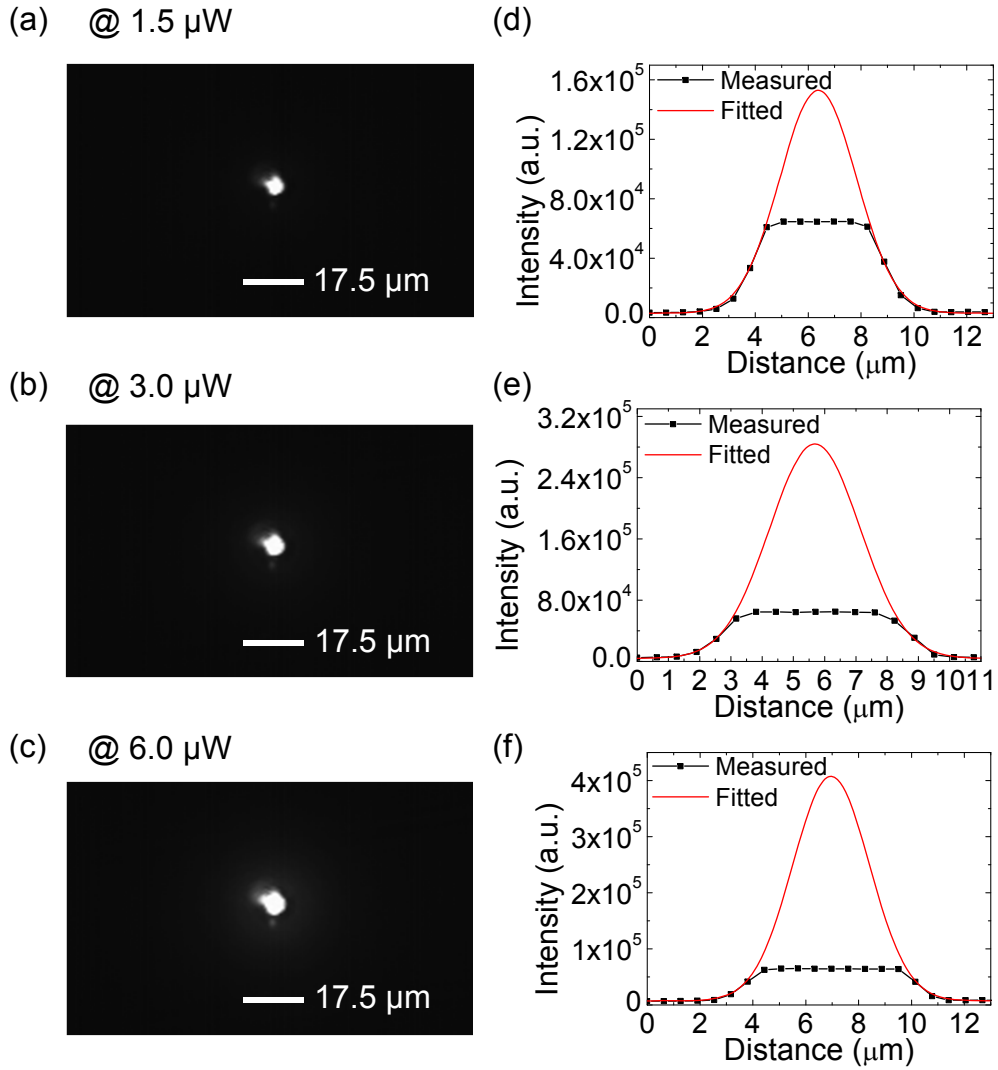

Figure D.1: (a-c) Captured images of the mode profile of the pump beam and (d-f) corresponding intensity profile of the reflected pump beam at each input pump power of 1.5, 3.0, and 6.0 μW, respectively. (The pump power indicated in the images are read from the optical power meter.)

D.2 Beam Waist of In-plane Hybrid VCL

In the same way, the mode profile of the hybrid VCL is measured. First, the pump laser is focused on the center of the hybrid VCL. To capture the lasing mode only, a long pass filter is used to filter out the 980 nm pump laser; and hence, only the lasing mode is capture as shown in Fig. D.2(a). The captured image is then image-processed and it is shown in Fig. D.2(b).

Table D.1: Measured pump beam waist.

Input power (μW)*	FWHM (μm)	1/e^2 width (μm)
0.5	3.19	5.29
1.0	3.39	5.68
1.5	3.45	5.80
2.0	3.47	5.81
2.5	3.27	5.77
3.0	3.45	5.77
6.0	3.45	5.80
9.0	3.47	6.01
12.0	3.44	5.79
15.0	3.45	5.98
18.0	3.46	5.81
Average**	3.44	5.84

*This input power indicates the 1% pump power read from the power meter connected to the 1% branch of the fiber couplers.

**Each average is obtained by averaging the corresponding measured results from the input power of 1.5 to 18.0 μW.

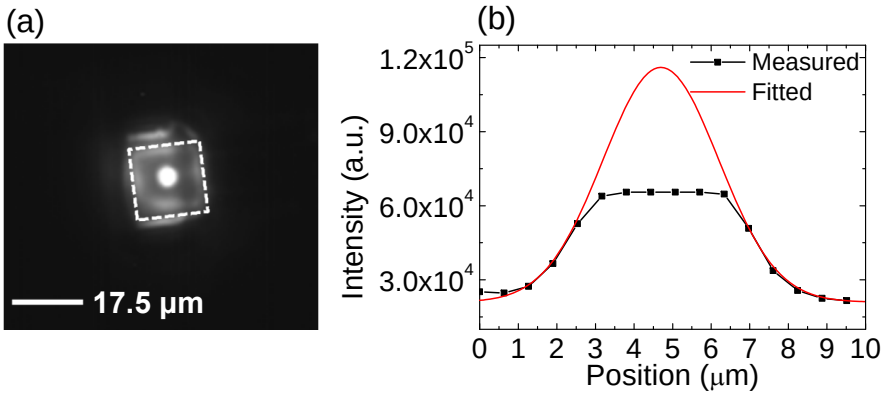

Figure D.2: (a) Captured image of the mode profile of the hybrid VCL and (b) corresponding intensity profile of the lasing mode.

E

Simulation Parameters.

In this appendix, the simulation parameters for the hybrid VCLs and the VCSEL with the double wafer-fused DBR, which are discussed in Chapter 4 to compare their vertical confinement factor, are provided. Table E.1 shows the hybrid VCL with the bottom TM HCG. The numerical simulation of the hybrid VCL with the TE HCG is conducted with the top dielectric DBR and III-V layer, which is used for the TM HCG structure. The parameters are listed in Table E.2.

Table E.1: Parameters of the hybrid VCL with TM HCG.

Layer	Thickness (nm)	Refractive index	Comment
Incident	Half infinite	1.0	-
Top dielectric DBR	132.6/261.8	2.923/1.48 a-Si/SiO_2	6 pairs
III-V layer	489.6	3.1661	InP
Air gap	303.8	1.0	-
Bottom TM HCG	492	3.48/1.0 a-Si/air	Period (703.4 nm) Si bar width (323 nm)
Exit	Half infinite	1.48	-

Table E.2: Parameters of the hybrid VCL with TE HCG.

Layer	Thickness (nm)	Refractive index	Comment
Incident	Half infinite	1.0	-
Top dielectric DBR	132.6/261.8	2.923/1.48 a-Si/SiO_2	6 pairs
III-V layer	489.6	3.1661	InP
Air gap	918.9	1.0	-
Bottom TE HCG	238	3.48/1.0 a-Si/air	Period (1,000 nm) Si bar width (322 nm)
Exit	Half infinite	1.48	-

For the double wafer-fused VCSEL, the 40 pair p-GaAs/p-AlGaAs and 30 pair n-AlAs/n-GaAs are used. Since the p-type DBR possesses a index contrast of 0.33, it needs a larger number of pair of DBR when compared to the n-type DBR, which has a index contrast of 0.49. In addition, the incident and exit medium are assumed to be the same as the hybrid VCLs. All the parameters are in Table E.3.

Table E.3: Parameters of the VCSEL with double wafer-fused DBRs.

Layer	Thickness (nm)	Refractive index	Comment
Incident	Half infinite	1.0	-
Top epitaxial DBR	114.6/127.0	3.38/3.05 p-GaAs/p-AlGaAs	40 pairs
III-V layer	489.6	3.1661	-
Bottom epitaxial DBR	114.6/134.1	3.38/2.89 n-AlAs/n-GaAs	30 pairs
Exit	Half infinite	1.48	-

Bibliography

[1] J. W. Goodman, F. I. Leonberger, S.-Y. Kung and R. A. Athale. Optical interconnections for VLSI systems. *Proc. IEEE* **72**, 850 (1984).

[2] D. A. B. Miller. Optical interconnects to electronic chips. *Appl. Opt.* **49**, F59 (2010).

[3] IBM, Silicon Photonics (2015), http://www.extremetech.com/extreme/205713-ibm-announces-silicon-photonics-breakthrough-set-to-break-100gbs-barrier

[4] N. Izhaky, M. T. Morse, S. Koehl, O. Cohen, D. Rubin, A. Barkai, G. Sarid, R. Cohen and M. J. Paniccia. Development of CMOS-compatible integrated silicon photonics devices. *IEEE J. Sel. Topics Quantum Electron.* **12**, 1688 (2006).

[5] M. A. Popović, M. T. Wade, J. S. Orcutt, J. M. Shainline, C. Sun, M. Georgas, B. Moss, R. Kumar, L. Alloatti, F. Pavanello, Y.-H. Chen, K. Nammari, J. Notaros, A. Atabaki, J. Leu, V. Stojanović and R. J. Ram. *Proc. of SPIE* **9367**, 93670M (2015).

[6] M. Haurylau, G. Chen, H. Chen, J. Zhang, N. A. Nelson, D. H. Albonesi, E. G. Friedman and P. M Fauchet. On-chip optical interconnect roadmap: challenges and critical directions. *IEEE J. Sel. Topics Quantum Electron.* **12**, 1699 (2006).

[7] D. Liang and J. E. Bowers. Recent progress in lasers on silicon. *Nature Photon.* **4**, 511 (2010).

[8] G. T. Reed. The optical age of silicon. *Nature* **427**, 595 (2004).

[9] G. Roelkens, J. V. Campenhout, J. Brouckaert, D. V. Thourhout, R. Baets, P. R. Romeo, P. Regreny, A. Kazmierczak, C. Seassal. X. Letartre, G. Hollinger, J. M. Fedeli, L. D. Cioccio and C. Lagahe-Blanchard. III-V/Si photonics by die-to-wafer bonding. *Mater. Today* **10**, 36 (2007).

[10] H. Rong, R. Jones, A. Liu, O. Cohen, D. Hak, A. Fang and M. Paniccia. A continuous-wave Raman silicon laser. *Nature* **433**, 725 (2005).

[11] S. G. Cloutier, P. A. Kossyrev and J. Xu. Optical gain and stimulated emission in periodic nanopatterned crystalline silicon. *Nat. Mater.* **4**, 887 (2005).

[12] R. E. Camacho-Aguilera, Y. Cai, N. Patel. J. T. Bessette, M. Romagnoli, L. C. Kimerling and J. Michel. An electrically pumped germanium laser. *Opt. Express* **20**, 11316 (2012).

[13] S. Wirths, R. Geiger, N. v. d. Driesch, G. Mussler, T. Stoica, S. Mantl, Z. Ikonic, M. Luysberg, J. M. Hartmann, H. Sig, J. Faist, D. Buca and D. Grützmacher. Lasing in direct-bandgap GeSn alloy grown on Si. *Nature Photon.* **9**, 88 (2015).

[14] M. Ortsiefer, B. Kögel, J. Rosskopf, M. Görblich, Y. Xu, C. Gréus and C. Neumeyr. Long wavelength high speed VCSELs for long haul and data center. In *Optical Fiber Communication Conference*, paper W4C.2. (2014).

[15] A. W. Fang, H. Park, O. Cohen, R. Jones, M. J. Paniccia and J. E. Bowers. Electrically pumped hybrid AlGaInAs-silicon evanescent laser. *Opt. Express* **14**, 9203 (2006).

[16] A. W. Fang, H. Park, Y.-h. Kuo, R. Jones, O. Cohen, D. Liang, O. Raday, M. N. Sysak, M. J. Paniccia and J. E. Bowers. Hybrid silicon evanescent devices. *Mater. Today* **10**, 28 (2007).

[17] D. Liang *et. al.* High-quality 150 mm InP-to-Silicon epitaxial transfer for silicon photonic integrated circuits. *Electrochem. Solid State Lett.* **12**, H101 (2009).

[18] C. Zhang, S. Srinivasan, Y. Tang, M. J. R. Heck, M. L. Davenport and J. E. Bowers. Low threshold and high speed short cavity distributed feedback hybrid silicon lasers. *Opt. Express* **22**, 10202 (2014).

[19] K. Takeda, T. Sato, T. Fujii, E. Kuramochi, M. Notomi, K. Hasebe, T. Kakitsuka and S. Matsuo. Heterogeneously integrated photonic-crystal lasers on silicon for on/off chip optical interconnects.

[20] K. Iga. Vertical-cavity surface-emitting laser: its conception and evolution. *Jpn. J. Appl. Phys.* **47**, 1 (2008).

[21] K. Iga, F. Koyama and S. Kinoshita. Surface emitting semiconductor lasers. *IEEE J. Quantum Electron.* **24**, 1845 (1988).

[22] E. Higurashi, T. Imamura, T. Suga and R. Sawada. Low-temperature bonding of laser diode chips on silicon substrates using plasma activation of Au films. *IEEE Photon. Technol. Lett.* **19**, 1994 (2007).

[23] J. Witzens, A. Scherer, G. Pickrell, D. Louderback and P. Guilfoyle. Monolithic integration of vertical-cavity surface-emitting lasers with in-plane waveguides. *Appl. Phys. Lett.* **86**, 101105 (2005).

[24] H. T. Hattori, X. Letartre, C. Seassal, P. Rojo-Romeo, J. L. Leclercq and P. Viktorovitch. Analysis of hybrid photonic crystal vertical cavity surface emitting lasers. *Opt. Express* **11**, 1799 (2003).

[25] I.-S. Chung and J. Mørk. Silicon-photonics light source realized by III-V/Si-grating-mirror laser. *Appl. Phys. Lett.* **97**, 151113 (2010).

[26] J. A. Tatum. Evolution of VCSELs. *Proc. SPIE* **9001**, 90010C-1 (2014).

[27] M. C. Y. Huang, Y. Zhou and C. J. Chang-Hasnain. A surface-emitting laser incorporating a hihg-index-contrast subwavelength grating. *Nature Photon.* **1**, 119 (2007).

[28] C. Sciancalepore, B. B. Bakir, X. Letartre, J. Harduin, N. Olivier, C. Seassal, J.-M. Fedeli and P. Viktorovitch. CMOS-compatible ultra-compact 1.55-μm emitting VCSELs using double photonic crystal mirrors. *IEEE Photon. Technol. Lett.* **24**, 455 (2012)

[29] A. Larsson. Advances in VCSELs for communication and sensin. *IEEE J. Sel. Topics Quantum Electron.* **17**, 1552 (2011).

[30] E. Kapon and A. Sirbu. Long-wavelength VCSELs: power-efficient answer. *Nature Photon.* **3**, 27 (2009).

[31] M. A. Fisher *et. al.* Pulsed electrical operation of 1.5-μm vertical-cavity surface-emitting lasers. *IEEE Photon. Technol. Lett.* **7**, 608 (1995).

[32] A. Karim, S. Björlin, J. Piprek and J. E. Bowers. Long-wavelength vertical-cavity lasers and amplifiers. *IEEE J. Sel. Topics Quantum Electron.* **6**, 1244 (2000).

[33] P. Westbergh, J. S. Gustavsson, B. Kö, Å. Haglund, A. Larsson, A. Mutig, A. Nadtochiy, D. Bimberg and A. Joel. 40 Gbit/s error-free operation of oxide-confined 850 nm VCSEL. *Electron. Lett.* **46**, 1014 (2010).

[34] S. A. Blokhin, J. A. Lott, A. Mutig, G. Fiol, N. N. Ledenstov, M. V. Maximov, A. M. Nadtochiy, V. A. Shchukin and D. Bimberg. Oxide confined 850 nm VCSEL operating at bit rates up to 40 Gbit/s. *Electron. Lett.* **45**, 501 (2009).

[35] Y. C. Chang and L. A. Coldren. Efficient, high data rate, tapered oxide aperture vertica cavity surface emitting laser. *IEEE J. Sel. Topics Quantum Electron.* **15**, 704 (2009).

[36] A. Mutig, J. A. Lott, S. A. Blokhin, P. Moser, P. Wolf, W. Hofmann, A. M. Nadtochiy, A. Payusov and D. Bimberg. High speed 980 nm VCSELs for very short reach optical interconnects. in *Proc. 22nd IEEE Int. Semicond. Laser Conf.*, 180 (2010).

[37] N. Suzuki, T. Anan, H. Hatakeyama, K. Fukatsu, K. Yashiki, K. Tokutome, T. Akagawa and M. Tsuji. High speed 1.1-μm-range InGaAs-based VCSELs. *IEICE Trans. Electron.* **E92-C**, 942 (2009).

[38] L. A. Coldren, S. W. Corzine and M. L. Mašanović. *Diode Lasers and Photonic Integrated Circuits*. (Wiley, 2012).

[39] M. Müller *et. al.* 1550-nm high-speed short-cavity VCSELs *IEEE J. Sel. Topics Quantum Electron.* **17**, 1158 (2011).

[40] G. C. Park, W. Xue, A. Taghizadeh, E. Semenova, K. Yvind, J. Mørk and I.-S Chung. *Laser Photon. Rev.* **9**, L11 (2015).

[41] A. Gatto, A. Boletti, P. Boffi, C. Neumeyr, M. Ortsiefer, E. Rönneberg and M. Martinelli. 1.3 μm VCSEL transmission performance up to 12.5 Gb/s for metro access networks. *IEEE Photon. Technol. Lett* **21**, 778 (2009).

[42] D. I. Babić *et. al.* Room-temperature continuouse-wave operation of 1.54-μm vertical-cavity lasers. *IEEE Photon. Technol. Lett.* **7**, 1225 (1995).

[43] J. Piprek, D. I. Babic and J. E. Bowers. Numerical analysis of 1.54 μm double-fused vertical-cavity lasers operating continuous-wave up to 33 °C. *Appl. Phys. Lett.* **68**, 2630 (1996).

[44] S. Rapp, J. Piprek, K. Streubel, J. André and J. Wallin. Temperature sensitivity of 1.54-μm vertical-cavity lasers with an InP-based Bragg reflector. *IEEE. J. Quantum Electron.* **33**, 1839 (1997).

[45] L. Goldstein *et. al.* GaAlAs/GaAs metamorphic Bragg mirror for long wavelength VCSELs. *Electron. Lett.* **34**, 268 (1998).

[46] F. Genty, G. Almuneau, L. Chusseau, G. Boissier, J.-P Malzac. P. Salet and J. Jacquet. High reflectivity Te-doped GaAsSb/AlAsSb Bragg mirror for 1.5μm surface emitting lasers. *Electron. Lett.* **33**, 140 (1997).

[47] K. Streubel, S. Rapp, J. André and J. Wallin. Room-temperature pulsed operation of 1.5-μm vertical cavity lasers with an InP-based Bragg reflector. *IEEE. Photon. Technol. Lett.* **8**, 1121 (1996).

[48] I. F. L. Dias, B. Nabet, A. Kohl, J. L. Benchimol and J. C. Harmand. Electrical and optical characteristics of n-type-doped distributed Bragg mirrors on InP. *IEEE Photon. Technol. Lett.* **10**, 763 (1998).

[49] D. Sun *et. al.* Sub-mA threshold 1.5-μm VCSELs with epitaxial and dielectric DBR mirrors. *IEEE. Photon. Technol. Lett.* **15**, 1677 (2003).

[50] C. F. R. Mateus, M. C. Y. Huang, Y. Deng, A. R. Neureuther and C. J. Chang-Hasnain. Ultrabroadband mirror using low-index cladded subwavelength grating. *IEEE Photon. Technol. Lett.* **16**, 518 (2004).

[51] J. L. Jewell, K. F. Huang, K. Tai, Y. H. Lee, R. J. Fischer, S. L. McCall and A. Y. Cho. Vertical cavity single quantum well laser. *Appl. Phys. Lett.* **(**55), 424 (1989).

[52] D. I. Babić and W. Corzine. Analytic expressions for the reflection delay, penetration depth, and absorptance of quater-wave dielectric mirrors. *IEEE J. Quantum Electron* **28**, 514 (1992).

[53] C. J. Chang-Hasnain and W. Yang. High-contrast gratings for integrated optoelectronics. *Adv. Opt. Photonics* **4**, 379 (2012).

[54] K. D. Choquette, R. P. Schneider, Jr., K. L. Lear and R. E. Leibength. Gain-dependent polarization properties of vertical-cavity lasers. *IEEE J. Sel. Topics Quantum Electron.* **1**, 661 (1995).

[55] A. Taghizadeh, G. C. Park, J. Mørk and I.-S. Chung. Hybrid grating reflector with high reflectivity and broad bandwidth. *Opt. Express* **22**, 21175 (2014).

[56] T. Makino. Transfer matrix method with applications to distributed feedback optical devices. *Prog. Electromagn. Res.* **10**, 271 (1995).

[57] M. G. Moharam and T. K. Gaylord. Diffraction analysis of dielectric surface-relief grating. *I. Opt. Soc. Am.* **72**, 1385 (1982).

[58] M. G. Moharam and T. K. Gaylord. Rigorous coupled-wave analysis of metallic surface-relief gratings. *J. Opt. Soc. Am. A* **3**, 1780 (1986).

[59] M. G. Moharam, D. A. Pommet and E. B. Grann. Stable implementation of the rigorous coupled-wave analysis for surface-relief gratings: enhanced transmittance matrix approach. *J. Opt. Soc. Am. A* **12**, 1077 (1995).

[60] M. G. Moharam, E. B. Gram, D. A. Pommet and T. K. Gaylord. Formulation for stable and efficient implementation the rigorous coupled-wave analysis of binary gratings. *J. Opt. Soc. Am. A* **12**, 1068 (1995).

[61] N. Chateau and J.-P Hugonin. Algorithm for the rigorous coupled-wave analysis of grating diffraction. *J. Opt. Soc. Am. A* **11**, 1321 (1994).

[62] J. H. Kim, L. Chrostowski, E. Bisaillon and D. V. Plant. DBR, sub-wavelength grating, and photonic crystal slab Fabry-Perot cavity design using phase analysis by FDTD. *Opt. Express* **15**, 10330 (2007).

[63] C. Sauvan, J. P. Hugonin and P. Lalanne. Difference between penetration and damping lengths in photonic crystal mirror. *Appl. Phys. Lett.* **95**, 211101 (2009).

[64] A. Liu, W. H. E. Hofmann and D. H. Bimberg. Integrated high-contrast-grating optical sensor using guided mode. *IEEE J. Quantum Electron.* **51**, 6600108 (2015).

[65] B. W. Shore, M. D. Perry, J. A. Britten, R. D. Boyd, M. D. Feit, H. T. Nguyen, R. Chow and G. E. Loomis. Design of high-efficiency dielectric reflection gratings. *J. Opt. Soc. Am. A* **14**, 1124 (1997).

[66] T. Clausnitzer, T. Kä, E.-B. Kley and A. Tünnermann. An intelligible explanation of highly-efficient diffraction in deep dielectric rectangular transmission gratings. *Opt. Express* **13**, 10448 (2005).

[67] M. Shokooh-Saremi and R. Magnusson. Wideband leaky-mode resonance reflectors: influence of grating profile and sublayers. *Opt. Express* (16), 18249 (2008).

[68] P. Viktorovitch, C. Sciancalepore, B. B. Bakir, X. Letartre and C. Seassal. Double photonic crystal vertical-cavity surface-emitting lasers. *Proc. of SPIE* **8633** 863302-1 (2013).

[69] H. Kim, I.-M. Lee and B. Lee. Extended scattering-matrix method for efficient full parallel implementation of rigorous coupled-wave analysis. *J. Opt. Soc. Am. A* **24**, 2313 (2007).

[70] H. Kim, J. Park and B. Lee. *Fourier Modal Method and Its Applications in Computational Nanophotonics*. (CRC Press, 2012).

[71] I.-S. Chung. J. Mørk, A. Sirbu, V. Iakovlev, A. Mereuta, A. Caliman and E. Kapon. 80-nm-tunable high-index-contrast subwavelength grating long-wavelength VCSEL: proposal and numerical simulations. *Proc. of SPIE* **7615**, 76150K (2010).

[72] D. Zhao, Z. Ma and W. Zhou. Field penetrations in photonic crystal Fano reflectors. *Opt. Extress* **18** 14152 (2010).

[73] I.-S. Chung. Study on differences between high contrast grating reflectors for TM and TE polarizations and their impact on VCSEL designs. *Opt. Express* **23**, 16730 (2015).

[74] H. Soda, K. Iga, C. Kitahara and Y. Suematsu. GaInAsP/InP surface emitting injection lasers. *Jpn. J. Appl. Phys.* **18**, 2329 (1979).

[75] F. Koyama, S. Kinoshita and K. Iga. Room temperature CW operation of GaAs vertical cavity surface emitting laser. *IEICE Trans.* **E71**, 1089 (1988).

[76] D. Liang and J. E. Bowers. Highly efficient vertical outgassing channels for low-temperature InP-to-silicon direct wafer bonding on the silicon-on-insulator substrate. *J. Vac. Sci. Techno. B* **26(4)**, 1560 (2008).

[77] B. Nagler, M. Peeters, J. Albert, G. Verschaffelt, K. Panajotov, H. Thienpont, I. Veretennicoff, J. Danckaert, S. Barbay, G. Giacomelli and F. Marin. Polarization-mode hopping in single-mode vertical-cavity surface-emitting lasers: theory and experiment. *Phys. Rev. A.* **68**, 013813 (2003).

[78] J. P. Hugonin and P. Lalanne. Perfectly matched layers as nonlinear coordinate transforms: a generalized formalization. *J. Opt. Soc. Am. A* **22**, 1844 (2005).

[79] D. Pasquariello and K. Hjort. Plasma-assisted InP-toSi low temperature wafer bonding. *IEEE J. Sel. Topics Quantum Electron.* **8**, 118 (2002).

[80] X. C. Tong. *Advanced Materials for Integrated Optical Waveguides.* (Springer, 2014).

[81] H. E. Li and K. Iga. *Vertical-Cavity Surface Emitting Laser Devices.* (Springer, 2002).

[82] P. Simonen, A. Heinonen, M. Kuulusa and J. Nurmi. Comparison of bulk and SOI CMOS technology in a DSP processor circuit implementation. *The 13th international conference on microelectronics*, 107 (2001).

[83] J. B. Kuo and S.-C. Lin. *Low-Voltage SOI CMOS VLSI Devices and Circuits.* (Wiley, 2001).

[84] C. Gunn. Fully integrated VLSI CMOS and photonics "CMOS Photonics". *Symposium on VLSI technology digest of technical paper*, 978-4-9000784-03-1 (2007).

[85] Silicon Integrated Nanophotonics, http://researcher.watson.ibm.com/researcher /view_group_subpage.php?id=2763

[86] A. Singh, D. A. Horsley, M. B. Cohn, A. P. Pisano and R. T. Howe. Batch transfer of microstructures using flip-chip solder bonding. *J. Microelectromech. Syst* **8**, 27 (1999).

[87] E. Peiner, A. Guttzeit and H.-H. Wehmann. The effect of threading dislocations on optical absorption and electron scattering in strongly mismatched heteroepitaxial III-V compound semiconductors on silicon. *J. Phys.: Condens. Matter* **14**, 13195 (2002).

[88] X. X. Zhang and J.-P Raskin. Low-temperature wafer bonding: a study of void formation and influence on bonding strength. *J. Microelectromech. Syst.* 14, 368 (2005).

[89] M. Wiegand, M. Reiche, and U. Gösele. Time-dependent surface properties and wafer bonding of O_2-plasma-treated silicon (100) surfaces. *J. Electrochem. Soc.* **147**, 2734 (2000).

[90] G. Roelkens *et. al.* III-V/silicon photonics for on-chip and intra-chip optical interconnects. *Laser Photon. Rev.* **4**, 751 (2010).

[91] H. Park, A. W. Fang, S. Kodama and J. E. Bowers. Hybrid silicon evanescent laser fabricated with a silicon waveguide and III-V offset quantum wells. *Opt. Express* **13**, 9460 (2005).

[92] Y. D. Koninck, G. Roelkens and R. Baets. Electrically pumped 1550 nm single mode III-V-on-silicon laser with resonant grating cavity mirrors. *Laser Photon. Rev.* **9** L6 (2015).

[93] S. Matsuo, A. Shinya, T. Kakitsuka, K. nozaki, T. Segawa, T. Sato, Y. Kawaguchi and M. Notomi. High-speed ultracompact buried heterostructure photonic-crystal laser with 13 fJ of energy consumed per bit transmitted. *Nature Photon.* **4**, 648 (2010).

[94] K. Takega, T. Sato, A. Shinya, K. Nozake, W. Kobayashi, H. Taniyama, M. Notomi, K. Hasebe, T. Kakitsuka and S. Matsuo. Few-fJ/bit data transmissions using directly modulated lambda-scale embedded active region photonic-crystal lasers. *Nature Photon.* **7**, 569 (2013).

[95] P. Moser, W. Hofmann, P. Wolf, J. A. Lott, G. Larisch, A. Payusov, N. N. Ledentsov and D. Bimberg. 81 fJ/bit energy-to-data ratio of 850 nm vertical-cavity surface-emitting lasers for optical interconnects. *Appl. Phys. Lett.* **98**, 231106 (2011).

[96] R. Rodes, M. Müller, B. Li, J. Estaran, J. B. Jensen, T. Gruendl, M. Ortsiefer, C. Neumeyr, J. Rosskopf, K. J. Larsen, M.-C. Amann and I. Tafur Monroy. High-speed 1550 nm VCSEL data transmission link employing 25 GBd 4-PAM modulation and hard decision forward error correction. *J. Lightw. Technol.* **31**, 689 (2013).

[97] D. M. Kuchta, F. E. Doany, L. Schares, C. Neumeyr, A. Daly, B. Kögel, Jürgen Rosskopf and M. Ortsiefer. Error-free 56 Gb/s NRZ modulation of a 1530 nm VCSEL link. in Proc. *ECOC 2015*, Post-deadline paper PDP.1.3, (2015).

[98] J. Heinrich, E. Zeeb and K. J. Ebeling. Butt-coupling efficiency of VCSEL's into multimode fibers. *IEEE Photon. Technol. Lett.* **9**, 1555 (1997).

[99] D. Wiedenmann, R. King, C. Jung, R. Jä, R. Michalzik, P. Schnitzer, M. Kicherer and K. J. Ebeling. *IEEE J. Sel. Topics Quantum Electron.* **5**, 503 (1999).

[100] T. Ouchi, A. Imada, T. Sato and H. Sakata. Direct coupling of VCSELs to plastic optical fibers using guide holes patterned in a thick photoresist. *IEEE Photon. Technol. Lett.* **14**, 263 (2002).

[101] S. H. Hwang, J. Y. An, M.-H. Kim, W. C. Choi, S. R. Cho, S. H. Lee, H. S. Cho and H.-H. Park. VCSEL array module using (111) facet mirrors of a V-grooved silicon optical bench and angled fibers. *IEEE Photon. Technol. Lett.* **17**, 477 (2005).

[102] P. Westbergh, R. Safaisini, E. Haglund, J. S. Gustavsson, A. Larsson, M. Geen, R. Lawrence and A. Joel. High-speed oxide confined 850-nm VCSELs

operating error-free at 40 Gb/s up to 85 °C. *IEEE Photon. Technol. Lett.* **25**, 768 (2013).

[103] A. Mutig and D. Bimberg. Progress on high-speed 980 nm VCSELs for short-reach optical interconnects. *Advances in Optical Technologies* **2011**, Article ID 290508, 15 (2011).

[104] J.-H. Shin, B.-S. Yoo, O.-K. Kwno, Y.-G. Ju and J.-H Lee. CW operation and threshold characteristics of all-monolithic InAlGaAs 1.55-μm VCSELs grown by MOCVD. *IEEE Photon. Technol. Lett.* **14**, 1031 (2002).

[105] M. C. Y. Huang, Y. Zhou and C. J. Chang-Hasnain. A nanoelectromechanical tunable laser. *Nature Photon.* **2**, 180 (2008).

[106] C. Sciancalepore, B. B. Bakir, S. Menezo, X. Letartre, D. Bordel and P. Viktorovitch. III-V-on-Si photonic crystal vertical-cavity surface-emitting laser arrays for wavelength division multiplexing. *IEEE Photon. Technol. Lett.* **25**, 1111 (2013).

[107] J. Ferrara, W. Yang, L. Zhu, P. Qiao and C. J. Chang-Hasnain. Heterogeneously integrated long-wavelength VCSEL using silicon high contrast grating on an SOI substrate. *Opt. Express* **23**, 2512 (2015).

[108] C. Zhang, D. Liang, G. Kurczveil, J. E. Bowers and R. G. Beausoleil. Thermal management of hybrid silicon ring lasers for high temperature operation. *IEEE J. Sel. Topics Quantum Electron.* **21**, 1502607 (2015).

[109] P. Viktorovitch, B. B. Bakir, S. Boutami, J.-L. Leclercq, X. Letartre, P. Rojo-Romeo, C. Seassal, M. Zussy, L. D. Cioccio and J.-M. Fedeli. 3D harnessing of light with 2.5D photonic crystals. *Laser Photon. Rev.* **4**, 401 (2010).

[110] M. Charbonneau-Lefort, E. Istrate, M. Allard, J. Poon and E. H. Sargent. Photonic crystal heterostructures: waveguiding phenomena and methods of solution in an envelope function picture. *Phys. Rev. B* **65**, 125318 (2002).

[111] A. Taghizadeh, J. Mørk and I.-S. Chung. Vertical-cavity in-plane heterostructures: physics and applications. *Appl. Phys. Lett.* **107**, 181107 (2015).

[112] C. F. R. Mateus, M. C. Y. Huang, L. Chen and C. J. Chang-Hasnain. Broadband mirror (1.12-1.62 μm) using a subwavelength grating. *IEEE Photon. Technol. Lett* **16**, 1676 (2004).

[113] H. Dalir and F. Koyama. Bandwidth enhancement of single-mode VCSEL with lateral optical feedback of slow light. *IEICE Electron. Express* **8**, 1075 (2011).

[114] H. Dalir and F. Koyama. Hihg-speed operation of bow-tie-shaped oxide aperture VCSELs with photon-photon resonance. *Appl. Phys. Express* **7**, 022102 (2014).

[115] R. Magnusson. Wideband reflectors with zero-contrast gratings. *Opt. Lett.* **39**, 4337 (2014).

[116] H. Tian, X. Cui, Y. Du, P. Tan, G. Shi and Z. Zhou. Broadband high reflectivity in subwavelength-grating slab waveguides. *Opt. Express* **23**, 27174 (2015).

[117] V. Karagodsky and C. J. Chang-Hasnain. Physic of near-wavelength high contrast gratings. *Opt. Express* **20**, 10888 (2012).

[118] D. Rosenblatt, A. Sharon and A. A. Friesem. Resonant grating waveguide structure. *IEEE J. Quantum Electron.* **33**, 2038 (1997).

[119] N. Grandjean and J. Massies. GaN/$Al_xGa_{1-x}N$ quantum wells grown by molecular beam epitaxy with thickness control at the monolayer scale. *Appl. Phys. Lett.* **73**, 1260 (1998).

[120] B. Johs, D. Doerr and S. Pittal. Real-time monitoring and control during MOVPE growth of CdTe using multiwavelength ellipsometry. *Thin Solid Films* **233**, 293 (1993).

[121] C. Sciancalepore, B. B. Bakir, X. Letartre, J.-M. Fedeli, N. Olivier, D. Bordel, C. Seassal, P. Rojo-Romeo, P. Regreny and P. Viktorovitch. Quasi-3D light confinement in double photonic crystal reflectors VCSELs for CMOS-compatible integration. *IEEE. Lightw. Technol.* **29**, 2015 (2011).

[122] M. Gębski, O. Kuzior, M. Dems, M. Wasiak, Y. Y. Xie, Z. J. Xu, Q. J. Wang, D. H. Zhang and T. Czyszanowski. Transverse mode control in high-contrast grating VCSELs. *Opt. Express* **22**, 20954 (2014).

[123] K. Liu, N.Li, D. K. Sadana and V. J. Sorger. Integrated nanocavity plasmon light source for on-chip optical interconnects. *ACS Photonics* DOI: 10.1021/acsphotonics.5b00476 (2016).